The First Year of Distributed Strain Sensing (DSS)
Monitoring in the Groningen Gas Field

Shell and NAM BV

M. Cannon and P. Kole

Datum June 2018

Editors Jan van Elk & Dirk Doornhof

General Introduction

Reservoir compaction is an important factor for subsidence and has therefore been studied since production from the Groningen field commenced. Most compaction monitoring relies on (indirect) measurements of subsidence through optical levelling surveys, GPS and/or InSAR. Compaction is then derived either through direct inversion or through compaction models calibrated to these subsidence measurements and compaction measurements on core samples.

Direct measurements of compaction in the reservoir have been taken by logging the relative movement of gamma-ray markers placed in monitoring wells. In a report (Ref. 1), the existing methods as well as a newly developed method to analyse in-situ measurements of compaction in the monitoring wells were reviewed in detail.

As reservoir compaction appears to be an important input into the seismological model, the studies into seismicity in the Groningen gas field have led to an intensified interest in compaction. Compaction can also be measured with the new technology of glass-fibre. A glass-fibre cable was installed over the reservoir section of the Zeerijp-3 monitoring well. The current report discussed the first year of experience with measuring compaction using this new technology.

Reference

1. In-situ compaction measurements using gamma ray markers, NAM, Pepijn Kole, June 2015

NAM

Title	**The First Year of Distributed Strain Sensing (DSS) Monitoring in the Groningen Gas Field**		**Date**	June 2018
			Initiator	NAM
Autor(s)	Mike Cannon and Pepijn Kole	**Editors**	Jan van Elk Dirk Doornhof	
Organisation	NAM	**Organisation**	NAM	
Place in the Study and Data Acquisition Plan	Study Theme: Reservoir Compaction Comment: Reservoir compaction is an important factor for subsidence and has therefore been studied since production from the Groningen field commenced. Most compaction monitoring relies on (indirect) measurements of subsidence through optical levelling surveys, GPS and/or InSAR. Compaction is then derived either through direct inversion or through compaction models calibrated to these subsidence measurements and compaction measurements on core samples. Direct measurements of compaction in the reservoir have been taken by logging the relative movement of gamma-ray markers placed in monitoring wells. In a report, the existing methods as well as a newly developed method to analyse in-situ measurements of compaction in the monitoring wells were reviewed in detail. As reservoir compaction appears to be an important input into the seismological model, the studies into seismicity in the Groningen gas field have led to an intensified interest in compaction. Compaction can also be measured with the new technology of glass-fibre. A glass-fibre cable was installed over the reservoir section of the Zeerijp-3 monitoring well. The current report discussed the first year of experience with measuring compaction using this new technology.			
Associated research	(1) Development of compaction models based on core measurements. (2) Inversion of subsidence to derive compaction estimates. (3) Seismological modelling.			
Used data	In-situ measurements of compaction by logging relative movement of gamma-ray markers installed in observations wells.			
Associated organisations	Baker Hughes.			
Assurance	Internal.			

Unrestricted **SR.17.00934**

The First Year of Distributed Strain Sensing (DSS) Monitoring in the Groningen Gas Field

by

M. Cannon (SIEP-PTI/RS)

P. Kole (NAM-PTU/E/Q)

Shell International Exploration and Production Inc., Houston

Further electronic copies can be obtained from the Global Information Centre.

Executive summary

This report provides an overview of Distributed Strain Sensing (DSS) technology based on fiber optical Bragg gratings and the installation of Baker Hughes' SureVIEW WIRE™ system in the Zeerijp-3 monitor well in the Groningen gas field, operated by Nederlandse Aardolie Maatschappij B.V. (NAM). Observations from measurements acquired during the first year of continuous strain monitoring (October 2015 – October 2016) are presented with some limited initial interpretation of the results. It should be noted that this work is ongoing. Though in some respects the DSS system is analogous to existing radioactive marker surveys, in many ways it is a wholly new measurement type and the interpretation and application of the data is still being developed and refined. The aim of this report is therefore to present observations from the data and demonstrate the potential insights and applications afforded by the technology. In addition, Distributed Temperature Sensing (DTS) data has also been acquired (it is required for the DSS system) and those results are presented as well.

It is understood that gas production from the Groningen field causes seismic activity in the local region. Seismicity forecasts are shared with the Dutch government and the NAM has deployed the DSS system to make certain the latest technology is being used to ensure the predicted depletion-induced reservoir compaction model is as reliable as possible.

The hazard and risk workflow uses modeled subsurface deformation along with information regarding fractures and fault offsets to provide a subsurface hazard map for seismicity. This hazard map is combined with a shallow subsurface velocity model to forecast the size of the Rayleigh waves at the surface. These predicted amplitudes are then compared to the rated strength of buildings in the region to arrive at a risk map. The DSS system provides a new independent data source obtained from directly measuring the subsurface which will help reduce uncertainty in the compaction model and constrain the inversion results.

The DSS data reveal the strain profile across the monitored interval to be quite inhomogeneous and more complex than is treated by existing models. Additionally, the observed compaction signal is not limited to the reservoir but extends into the overlying Ten Boer and underlying Carboniferous zones. This suggests that the volume of rock being compacted is potentially larger than previously thought.

Vertical compressibility values for the reservoir have been derived from the DSS measurements and simulated pressure depletion from the reservoir model. Previously, compressibility values had been obtained from measurements of core samples and from inversion models using surface subsidence data. The compressibility values from the core samples were notably larger than those obtained from the inversion modeling, and the discrepancy has formerly been attributed to sample damage of the cores. However, the results from the in situ DSS measurements also suggest higher compressibility values than those from the inversion. The observation that both (independent) experimental data sets show higher compressibilities might suggest that certain assumptions within the models should be reassessed.

Table of contents

1. Introduction

1.1. Well and Reservoir Surveillance using Fiber Optical Technology

Responsible and optimal reservoir management requires access to accurate and timely information. The primary goal of Well and Reservoir Surveillance (WRS) programs is to improve operational decisions and overall asset performance by comparing field data to models of the response of the reservoir and surrounding rocks to production or injection activities. Often, however, WRS efforts are hindered by a lack of suitable, high-quality data. Many options for acquiring field data involve a well intervention; consequently, the operator has to either defer production or wait to acquire the data during planned maintenance. In addition, well site operations associated with many traditional WRS activities (such as wireline logging) can be costly and involve safety or operational risks, both of which can prevent data acquisition attempts from succeeding. These drawbacks result in data often being collected infrequently which can lead to suboptimal management of the reservoir, inadequate model calibration, and lower ultimate recovery.

Distributed sensing with Fiber-Optical (FO) technology offers an alternative means for acquiring surveillance data without many of the tradeoffs associated with traditional methods [1]. Permanently installed FO systems provide timely data (often in near real-time) at a low marginal survey cost without well intervention. Furthermore, because the optically-instrumented completion is a passive sensor that is interrogated from the surface, operational risks or any adverse impact on well activities are avoided.

The use of FO measurements for WRS applications has grown significantly over the past two decades. Figure 1.1 shows the growth in the number of FO installations within Shell between 1993 and 2013. Distributed Temperature Sensing (DTS) is becoming a standard evaluation tool for activities such as monitoring the steam front in thermal EOR projects or injection conformance in waterfloods [2],[3]. In recent years, the application of Distributed Acoustic Sensing (DAS) for in-well geophysical and production (or injection) surveillance has rapidly matured [4],[5],[6],[7]. Distributed Pressure Sensing (DPS) has been used to monitor the fluid contact for oil-rim monitoring in observation wells [8]. The Distributed Strain Sensing (DSS) system discussed in this paper is the latest addition to the suite of FO technologies for WRS applications and was first installed in 2014 in the Belridge field for monitoring wellbore integrity across an active shear plane [9].

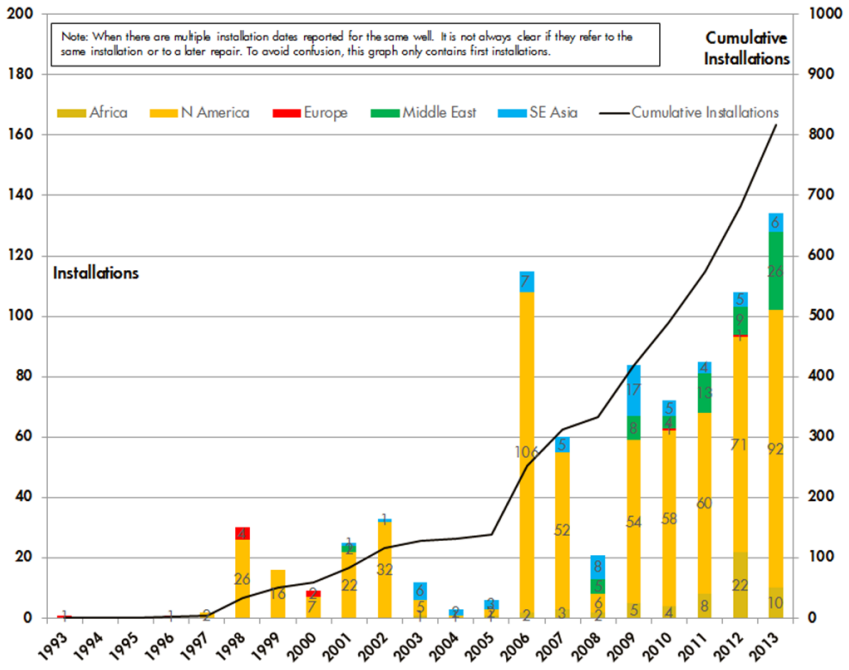

Figure 1.1: Number of Fiber Optic (FO) installations for Shell assets from 1993 to 2013. The solid black line indicates the cumulative sum.

The need for a DSS system stems from the fact that production or injection operations change the pore pressure, the total stress, and the effective stresses in the reservoir. As a result, the rocks deform and this can induce slippage along geological strata, faults, and fractures (or create new faults and fractures). Consequently, the wells undergo deformation in both reservoir and overburden rock intervals. This can be due to compaction or shear forces and can be expressed by buckling, dog-legs, wrinkling, etc. A DSS system can help to locate, describe, and analyze these modes of well deformation in an almost real-time fashion. By assuming that the well deformation reflects the reservoir deformation we can use the well as a "sensor" to learn about the mechanical behavior of the reservoir and the rocks around it. In this sense, the DSS data can be used to relate strains to changes in pore pressure via analysis of the well deformation, which is assumed to correspond to the reservoir deformation. This assumption is valid provided the well and FO cable are properly cemented to the formation (see Appendix 1).

A good example highlighting the need for DSS is the offshore Gulf of Mexico where, over ten years, sizeable reservoir compaction was diagnosed and the effectiveness of water injection (intended to reduce the rate of compaction) was evaluated [10],[11]. Because successive wireline logging surveys were roughly two years apart, it took years to prove that there was a serious compaction issue and even longer to become confident that the injection practices were effectively able to reduce the rate of compaction. However, given that data could only be acquired infrequently, it would have taken a long time to adjust the injection practices if they needed to be modified. Another good example of water flooding a reservoir to reduce subsidence is the Ekofisk field which subsided dramatically over roughly two decades of production before water injection started in 1987 [12]. Here too, regular

measurement of well deformation would have provided valuable insight in reservoir deformation, pore pressure distribution, and thus its injection effectiveness.

Shell and Baker Hughes have jointly developed an in-well FO based DSS system and the product is now commercially available from Baker Hughes, marketed under the name SureVIEW WIRE™ (Well Integrity Real-time Evaluation). As of October 2016, the system has been installed in 9 wells in 3 countries for 4 different operators. As mentioned above, the first installation of the SureVIEW WIRE was in April of 2014 for Aera Energy in the Belridge field, California. An additional 8 installations have occurred since that time, all of which were successful. Four (4) installations have been for Shell (2 in the United States, 2 in the Netherlands) and 5 have been for two separate non-Shell operators in Canada. The Canadian installations have primarily been for the purpose of well/formation integrity monitoring in Cyclical Steam Stimulation (CSS) and Steam-Assisted Gravity Drainage (SAGD) fields where it is important to ensure that injected steam is contained in the productive layers of the reservoir [13]. The SureVIEW WIRE installations to date are summarized in Table 1.1.

Table 1.1: Total global (Shell and non-Shell) SureVIEW WIRE Installations by Baker Hughes

Count	Date	Country	Operator	Application
1	Apr 2014	United States	Aera Energy	Compaction Monitoring/ Well Integrity
2	Oct 2014	Canada	Unknown Operator 'A'	Caprock Integrity
3	Nov 2014	United States	Aera Energy	Compaction Monitoring/ Injection Profiling
4	Jan 2015	Canada	Unknown Operator 'B'	Well Integrity
5	Jan 2015	Canada	Unknown Operator 'B'	Well Integrity
6	Jan 2015	Canada	Unknown Operator 'B'	Well Integrity
7	Oct 2015	The Netherlands	NAM	Compaction Monitoring
8	Feb 2016	Canada	Unknown Operator 'B'	Well Integrity
9	Oct 2016	The Netherlands	NAM	Compaction Monitoring/ Injection Profiling
10	Feb 2017	Canada	Unknown Operator 'B'	Well Integrity

Current and anticipated surveillance applications for DSS include:

- Monitoring reservoir/formation compaction
- Monitoring casing deformation (well integrity)
- Monitoring caprock integrity
- Early assessment of the effectiveness of remediate actions to improve well life and forecasting well life
- Injection conformance, in particular detection of out-of-zone injection
- Identifying zones that produce fluids
- Calibration of reservoir geomechanical, subsidence, and 4D seismic models
- Detection of fault (re)activation

1.2. Distributed Strain Sensing Technology

The DSS system consists of a permanently-installed downhole sensor and a Surface Interrogation Unit (SIU). The sensing element is a ¼" control line that is deployed along the outside of a well casing and cemented in place. Though the control line looks just like any other (unencapsulated) downhole FO cable, the internal construction of the SureVIEW WIRE is unique. The cable contains two fibers that are locked in place with adhesive so that mechanical strain is transmitted to the fibers.

The strain sensitivity is derived from the spectral response of individual Fiber Bragg Gratings (FBGs) which are optically etched into the core of the fiber using a pulse of light from an ultraviolet laser during the fiber manufacturing process [14]. Each FBG consists of a periodic variation in the index of refraction inscribed along the fiber core and only reflects light within a very narrow range of wavelengths determined (in large part) by the pitch of the grating (Figure 1.2). Input signals outside of this characteristic wavelength range pass through the grating with very little attenuation.

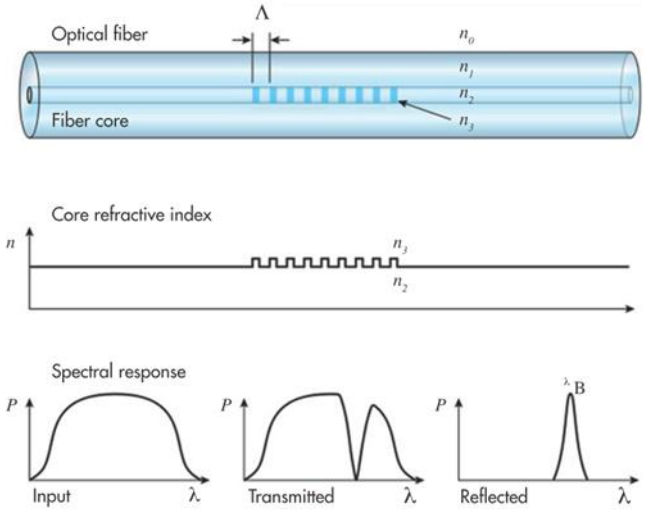

Figure 1.2: Schematic representation of an optical fiber with a grating etched into the core (top). Corresponding representation of the index of refraction along the core (middle). Spectral response of the fiber due to an in input signal with a broad range of wavelengths (bottom).

The gratings are each 5 mm long and spaced every 2 cm along the fiber. Initially, all the gratings are written to reflect light some nominal wavelength (known as the Bragg wavelength, λ_0). In this case, λ_0 = 1548 nm. However, when a FBG is compressed, light is reflected from the grating at a shorter wavelength because the pitch of the grating decreases (Figure 1.3). Conversely, the Bragg wavelength increases when the grating is pulled in tension. As discussed in the literature[14], the Bragg wavelength changes linearly with both strain, ε, and temperature changes, ΔT (over the ranges observed in typical producing reservoir systems). Specifically,

$$\lambda - \lambda_0 = \lambda_0 [c_\varepsilon \varepsilon + c_T \Delta T] \quad (1)$$

The strain coefficient, c_ε, is a property of the fiber due to the strain-optic effect (variation in the index of refraction of the fiber with strain). For the fiber used in this DSS system, $c_\varepsilon = 0.78$. The temperature coefficient, c_T, depends on properties of the glass in the fiber as a result of thermal expansion and the thermo-optic effect (variation of the index of refraction of the fiber with changes in temperature). However, c_T also depends on the thermoelastic properties of the medium in which the fiber is embedded (coatings on the fiber core, the cable components, and the surrounding environment). A description of the determination of c_T can be found in reference [9].

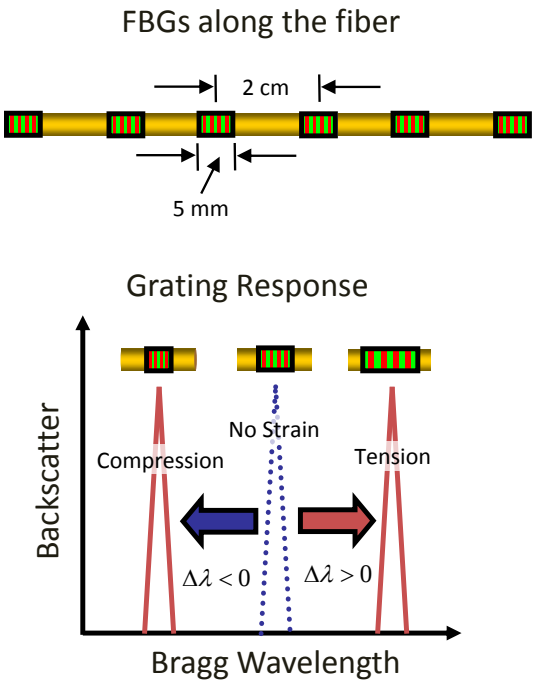

Figure 1.3: A FBG is placed every 2 cm along the fiber. Each FBG is 0.5 cm long (top). When compressed, the backscattered light is shifted to a lower wavelength because the grating becomes shorter (bottom). The opposite happens when a grating is in tension.

Because the fibers are fixed in a helical geometry (via a twisted core substrate), axial and bending modes of deformation can both be detected, enabling the identification of various modes of deformation (e.g., shearing, buckling, etc.). Figure 1.4 shows a schematic representation of a casing section instrumented with a DSS cable along with the corresponding strain profiles modeled under various simple deformations. When the casing (and thus the cable) undergoes uniaxial compression the entire fiber experiences a uniform strain decrease and the strain response is a simple bulk shift at all affected depths. Likewise, when the cable is pulled in tension the entire fiber experiences a uniform strain increase. However, when the cable is bent the strain response oscillates between tension and compression with a frequency that corresponds to the helix period of the fiber.

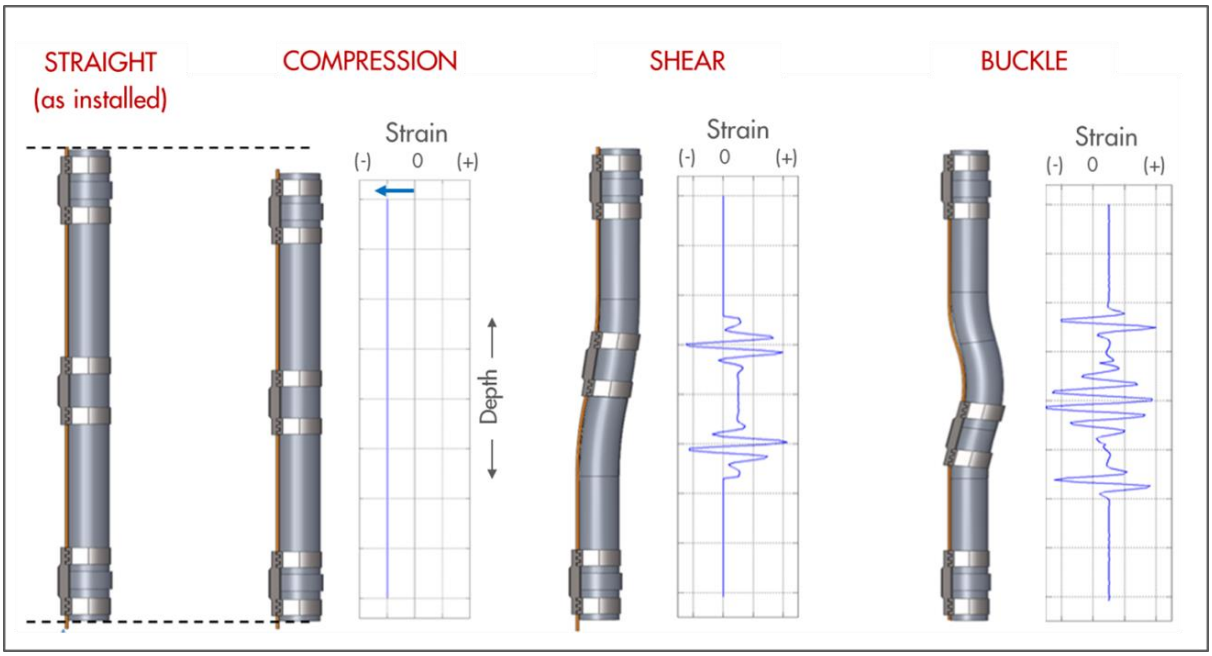

Figure 1.4: Idealized strain responses of the fiber as a function of depth along the casing due to compression, shear, and buckle deformation modes. (Graphics and simulated response provided by Baker Hughes.)

The spatial resolution of the system is comparable to the scale of the grating spacing, which is on the order of a few centimeters. A single measurement from an individual FBG can sense strains as low as 5 microstrain[1]; however, in practice this performance is improved (~1 microstrain) when the data are time averaged during permanent monitoring. The interrogator has a sensing length of 250 meters per channel (each channel is connected to an independent fiber) that can be arbitrarily offset by up to 10 km of lead-in length. With 4 channels available on the current unit, this provides up to 1 km of strain coverage along the well bore.

1.3. The Groningen Gas Field

Discovered in 1959, the Groningen field is the largest gas field in Europe and the 7th largest in the world, supplying gas to 98% of the population in the Netherlands. It is located along the northern coast of the Netherlands (Figure 1.5) and is operated by Nederlandse Aardolie Maatschappij (NAM), which is a 50/50 joint venture between Shell (the operating partner) and ExxonMobil.

[1] Equivalent to a 5 mm change over 1000 m.

Figure 1.5: The Groningen gas field located along the northern coast of the Netherlands.

It is understood that gas production from the Groningen field causes earthquakes in the local region. Because the NAM has a responsibility to determine the extent to which production activities may give rise to subsidence due to compaction of the porous rock layers where natural gas is produced [15], it is critical to continually calibrate subsidence, geomechanical, and forecast models to continuously-acquired field data. The NAM has been working since the start of gas production toward continuous improvement of the subsidence prediction and data acquisition technologies.

The primary existing sources of surveillance data utilized in the Groningen field include: survey leveling, Interferometric Synthetic Aperture Radar (InSAR), Global Positioning Systems (GPS), and in-well compaction measurements. Additionally, the surveillance data are supplemented by compaction measurements performed on rock samples in the laboratory.

Survey leveling utilizes elevation measurements between various benchmarks such as buildings, bridges, and viaducts. The subsidence can be deduced from changes in the relative positions of the benchmarks.

InSAR has been used since 2003 by the NAM to measure the surface deformation above the gas field. Results show good agreement with those from survey leveling and can be considered as an alternative technique for monitoring subsidence [15]. Subsidence monitoring with InSAR, however, has as much greater temporal resolution since data is collected every 24 days.

Between 2013 and 2014 the single GPS station located in Veendam was supplemented with 11 additional permanent stations distributed across the field (Figure 1.6). The areal spatial resolution of

the GPS stations is not as great as that provided by surveying or InSAR; however, the data are collected continuously.

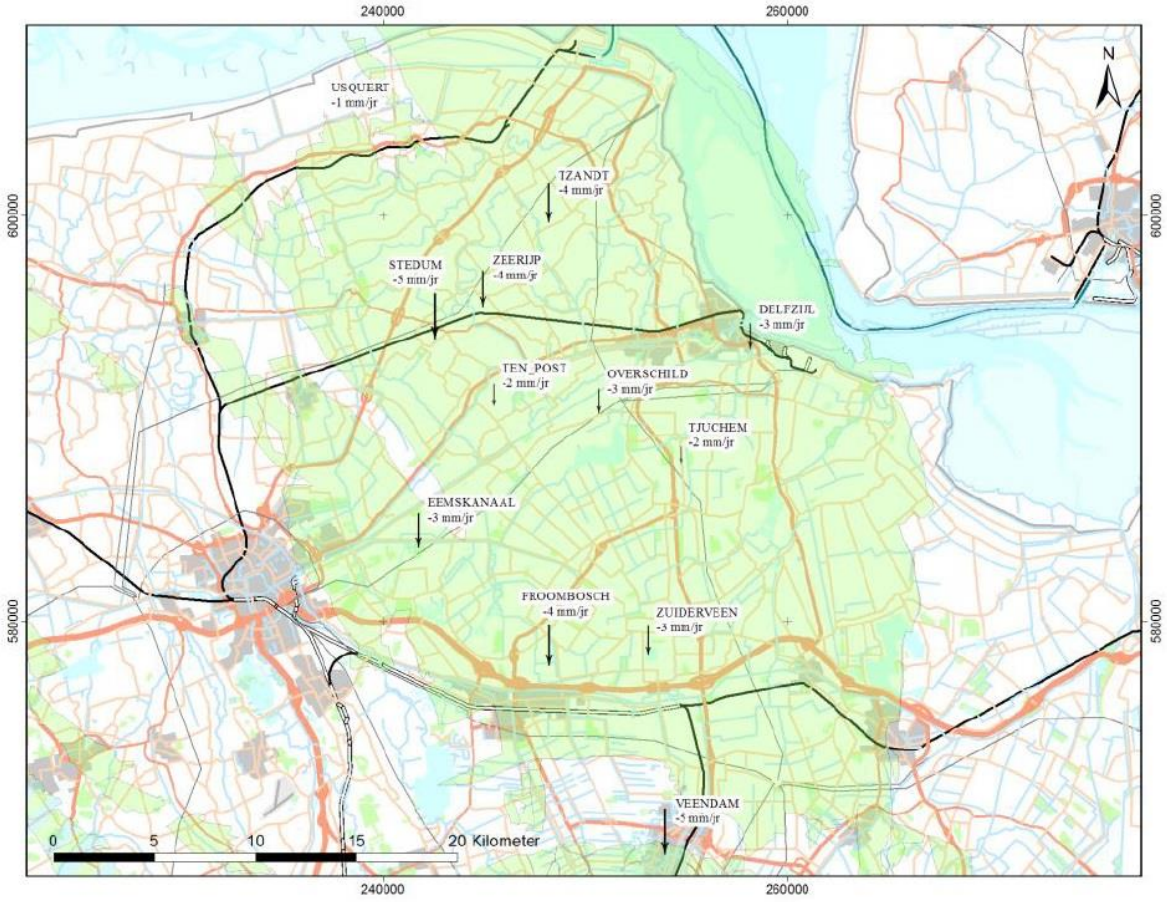

Figure 1.6: Locations of the permanent GPS stations above the Groningen field. The labels also include the decline rates observed over a 12 month period beginning in October 2014 [15].

The measurements used to determine the parameters of the compaction model (which, in turn, provides input to the field-wide subsidence model) are obtained from compaction measurements on rock samples in the laboratory and in-situ compaction measurements acquired in deep observation wells. Despite careful attempts to simulate reservoir conditions in the laboratory experiments, it is often observed that compaction behavior observed in core samples differs slightly from the compaction behavior observed in the field [15].

A number of years after production had begun a program for in-situ measurement of the reservoir compaction was established. Eleven (11) observation wells were drilled and radioactive bullets were embedded in the reservoir along the wellbore at a nominal initial spacing of ~10 m. The change in spacing between the markers is monitored by periodically (every few years) measuring their position with a wireline tool. Of the original 11 wells, 7 are still in operation: Uithuizermeeden, De Hond, Stedum, Ten Boer, Schildmeer, Delfzijl, and Roode Til (Figure 1.7). Two wells were recompleted as

producers (Usquert and Bierum), while one well was lost due to mechanical failure (Sappermeer). From 1974 to 1982 the measurement precision was insufficient to adequately determine the compaction. Since that time, various tools, vendors, and analysis methods have been utilized and a (seemingly) reasonable measure of the reservoir compaction over the past 3 decades has been obtained.

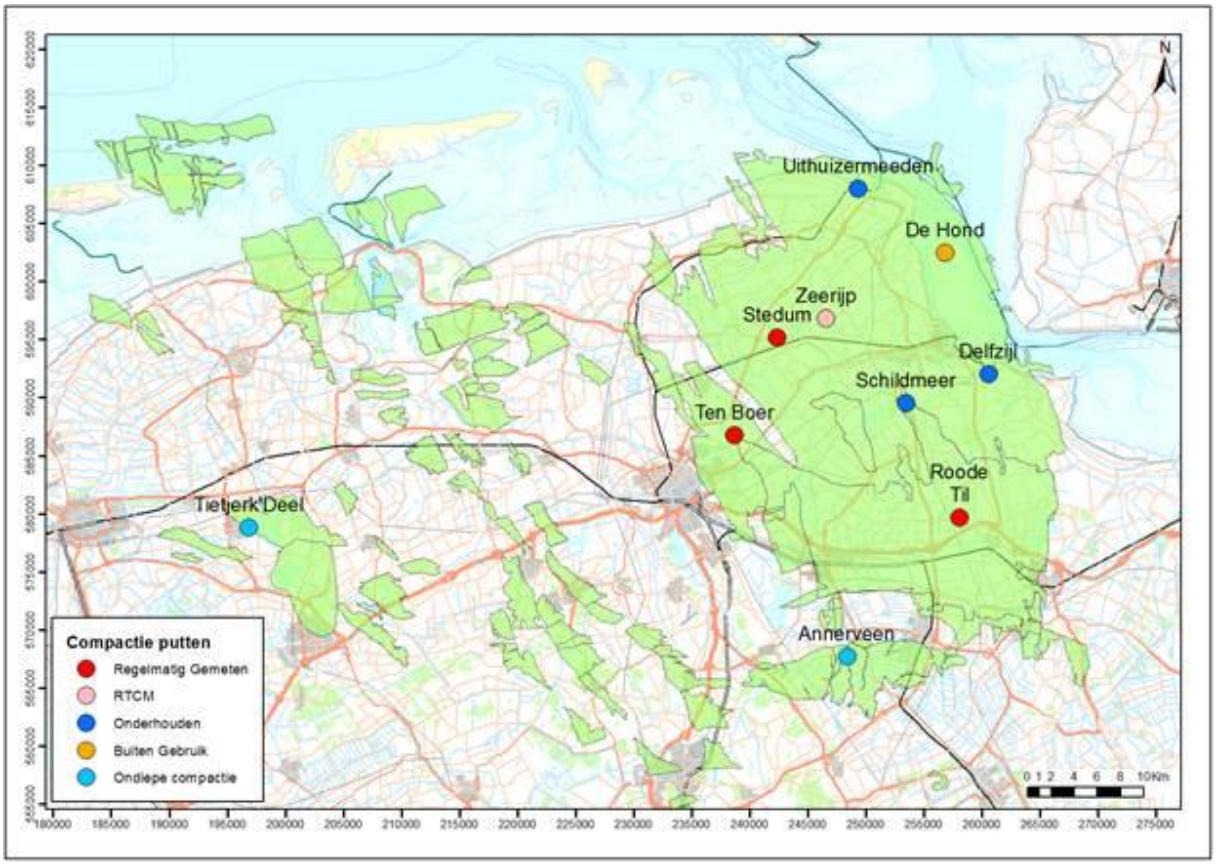

Figure 1.7: Locations of the monitor wells for in-situ compaction measurements [15]. Note that the shallow observation wells Annerveen and Tietjerk' Deel shown in the figure are outside the Groningen gas field.

Because the compaction process is relatively slow (< 50 με/year), the accuracy of the existing in-situ compaction monitoring program imposes a limit in the frequency of data acquisition. It has been observed that it is not meaningful to acquire data more frequently than once every ~5 years. Therefore, as part of the effort to improve the in-situ compaction monitoring program and better understand the causal relationship between gas production and seismicity, the SureVIEW WIRE was installed in a new monitor well (Zeerijp-3) located near the center of the subsidence bowl. The real time compaction measurements (RTCM) provided by the DSS system will be used to (continuously) calibrate the geomechanical model relating production (i.e., pressure depletion) to compaction. The increased sensitivity and measurement frequency provided by DSS enables a better means of

monitoring the effects of changes in the production rate on compaction behavior. This will reduce the uncertainty in the compaction model and help optimize the production scenarios to minimize the seismic hazard and risk.

2. Installation of the Fiber Optic DSS System in Zeerijp-3

The DSS system has been installed in Zeerijp-3, a near-vertical monitor well located near the center of the Groningen subsidence bowl (see Figure 2.1). (The well trajectory is purely vertical across the reservoir interval.) The primary purpose of the Zeerijp-2 and Zeerijp-3 wells is to provide permanent monitoring of subsurface microseismic activity via a geophone array installed across the reservoir interval. In addition to the permanent seismic and strain monitoring, Zeerijp-3 was also cored over 8 separate intervals. Drilling began on May 22, 2015 and was completed on August 21, 2015 at a total depth of 3885 m AHRT (3294 m TVRT). Permanent FO monitoring began 6 weeks later on Oct 12, 2015 after the rig had moved off location and the FO surface connections had been completed.

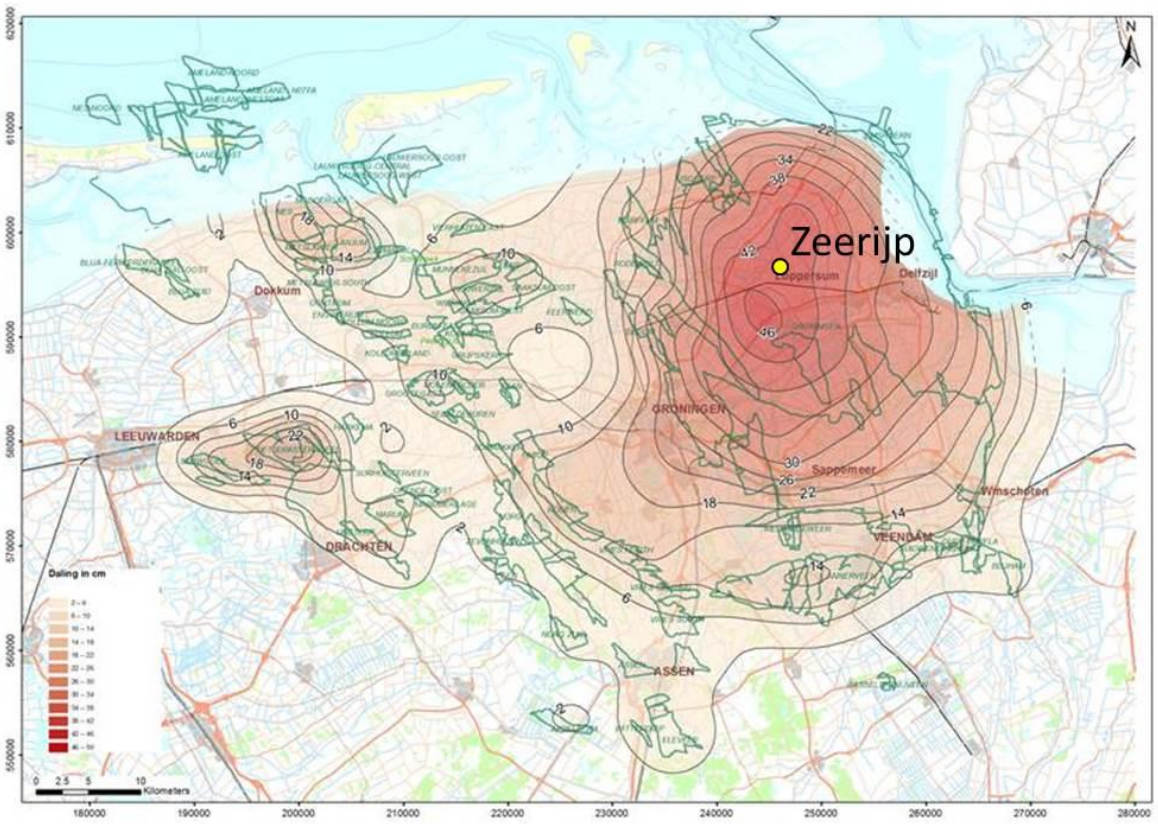

Figure 2.1: Location of the Zeerijp-3 well near the center of the Groningen subsidence bowl. The subsidence contours shown are taken from the 2080 prediction [15].

Two separate DSS cables were installed (end-to-end) in Zeerijp-3, providing approximately 450 meters of coverage along the well (Figure 2.2 – Figure 2.4), from 3390 – 3841 mAHRT. In addition to spanning the 215 m reservoir interval (ROSLU and ROSLL), the DSS coverage also extends 148 m into the overburden (spanning the entire 63 m of the Ten Boer Claystone interval (ROCLT) and 85 m into the Zechstein Salt) as well as 79 m into the underlying Carboniferous zone. It is noted

that the portion of the cable in the salt is between the 7" and 3.5" casing strings. However, it is believed that this does not have a notable impact on the strain measurement.

A secondary FO control line was installed that covers the entire length of the well. This cable contains ancillary fibers which, among other uses, provide the DTS measurement necessary for temperature correction of the DSS data. The geophne array was installed from 3275 – 3835 mAHRT at 40 meter spacing.

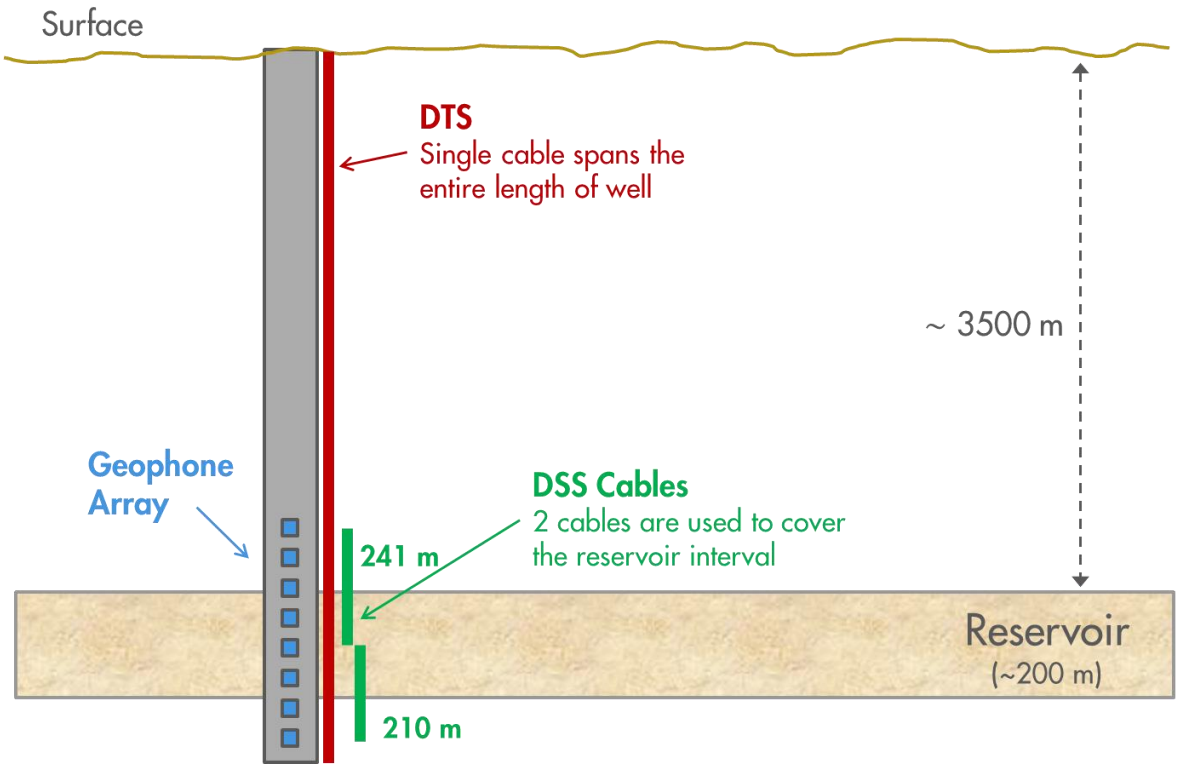

Figure 2.2: Simplified representation of the Fiber Optic and geophone installation in the well across the reservoir.

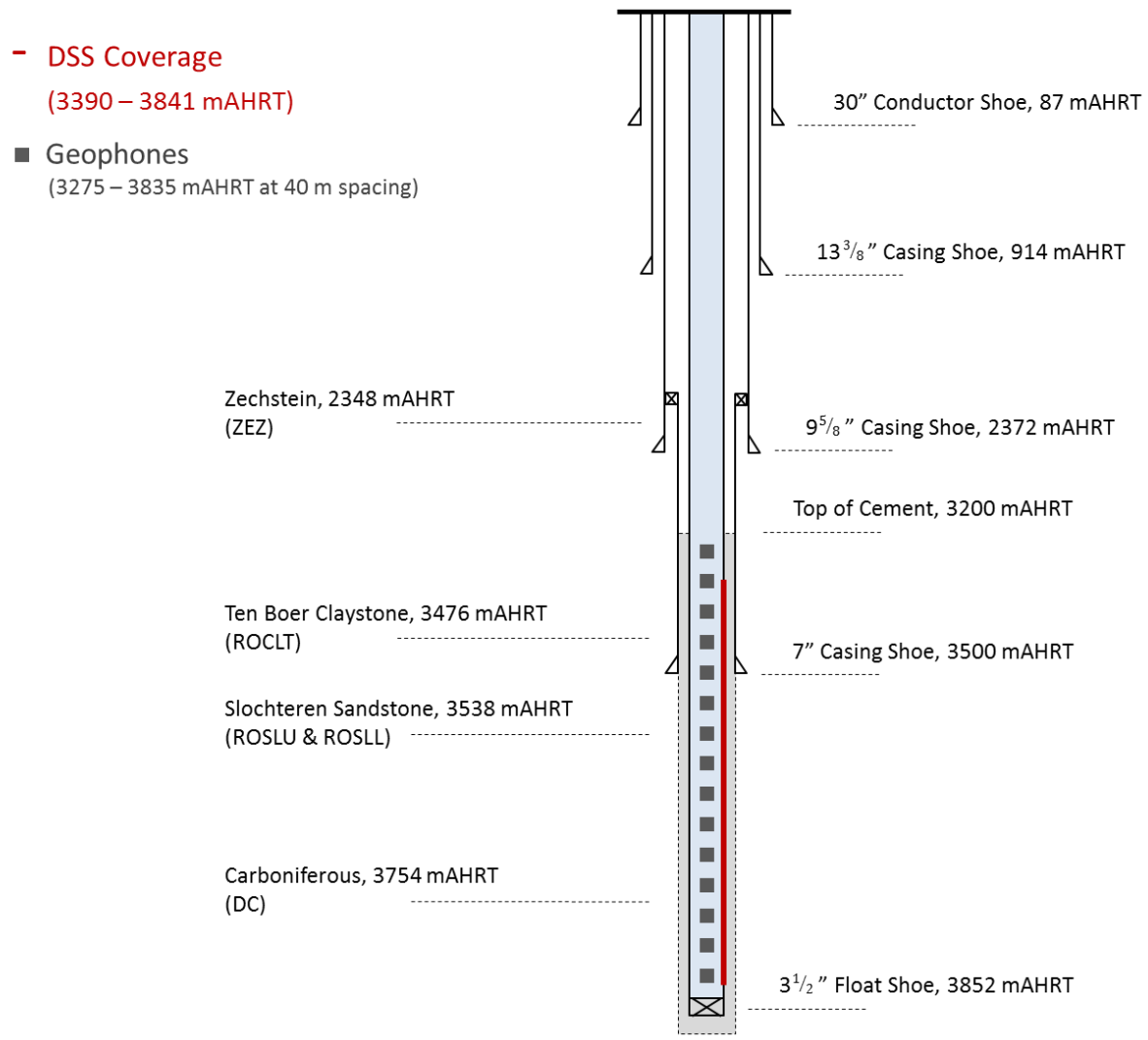

Figure 2.3: Simplified Zeerijp-3 well diagram including relevant formation tops and the DSS/geophone installations.

All of the fibers (including the lead-in fibers for the DSS cable) are contained in a single FO control line to a depth of 3390 m AHRT at which point the cable enters a splice housing (or 'H-Splice'). Below this depth, the fibers are contained in two separate cables, the DSS cable (SureVIEW Wire) and the auxiliary FO cable (sometimes called the FO downhole cable). Figure 2.4 shows a diagram of the installed FO lines. The 'Upper Cable' runs from 3390 to 3631 m AHRT and the 'Lower Cable' runs from 3631 to 3841 m AHRT.

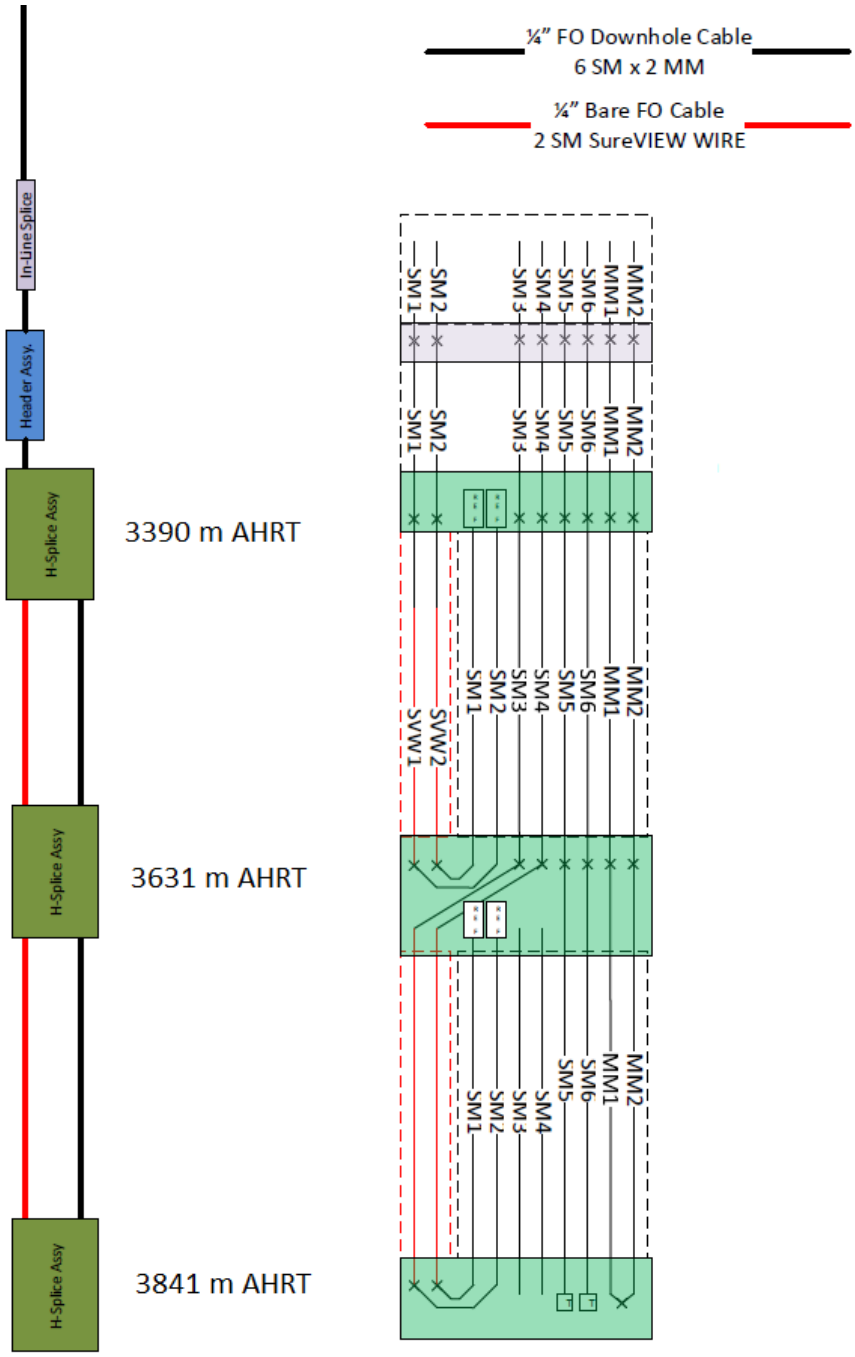

Figure 2.4: **Diagram of the installed FO lines. In the figure on the left, the red and black lines represent the DSS and auxiliary cable, respectively. The figure on the right shows all the fibers contained in the two FO control lines. The 2 left hand fibers indicated in red represent the 2 fibers bonded in the DSS cable (SureVIEW Wire). The remaining black lines represent the other 8 fibers (6 single-mode and 2 multi-mode) contained in the auxiliary cable. The depths of the middle of each H-Splice Assembly are indicated.**

The auxiliary cable contains 8 fibers. Four of these (SM1, SM2, SM3, & SM4) are connected to the strain sensing fibers in the DSS cable to provide the lead-in connection as well as the reference arm of the interferometric strain measurement [16],[17]. The two multi-mode fibers (MM1, MM2) are connected to the DTS interrogator. The remaining two single-mode fibers (SM5, SM6) are not being utilized and remain available for additional measurements (such as DAS).

As shown in Figure 2.5, each H-Splice is protected above and below by splice bumpers that prevent the housing from getting hung up while tripping in or out of the hole. It can also be seen in the picture that the auxiliary FO cable is encapsulated with a protective material (shown in yellow) but the DSS cable is not. The encapsulation on standard FO downhole cables is not bonded adequately to transmit strain from the exterior to the fibers and thus is not part of the SureVIEW Wire design.

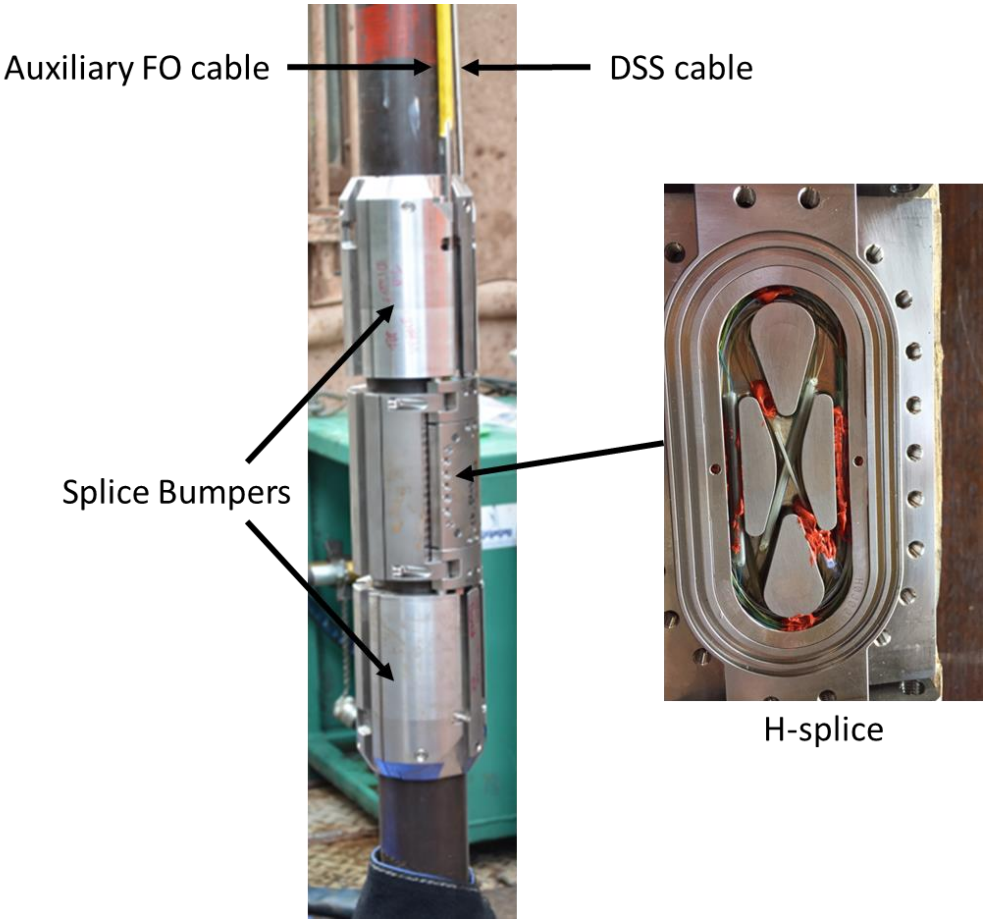

Figure 2.5: Bottom splice housing for the DSS and auxiliary FO control lines. The picture on the right shows the geometry of the fibers coiled inside the 'H-splice'.

The fibers exiting the well head are spliced to a FO surface cable that leads to a data cabin permanently housed at the well site. The data cabin accommodates an equipment rack containing the DSS Interrogator, DTS interrogator, computer, UPS & battery pack, a fiber routing unit, and a SureFIELD DataHub system which is used to remotely connect to the equipment in the rack.

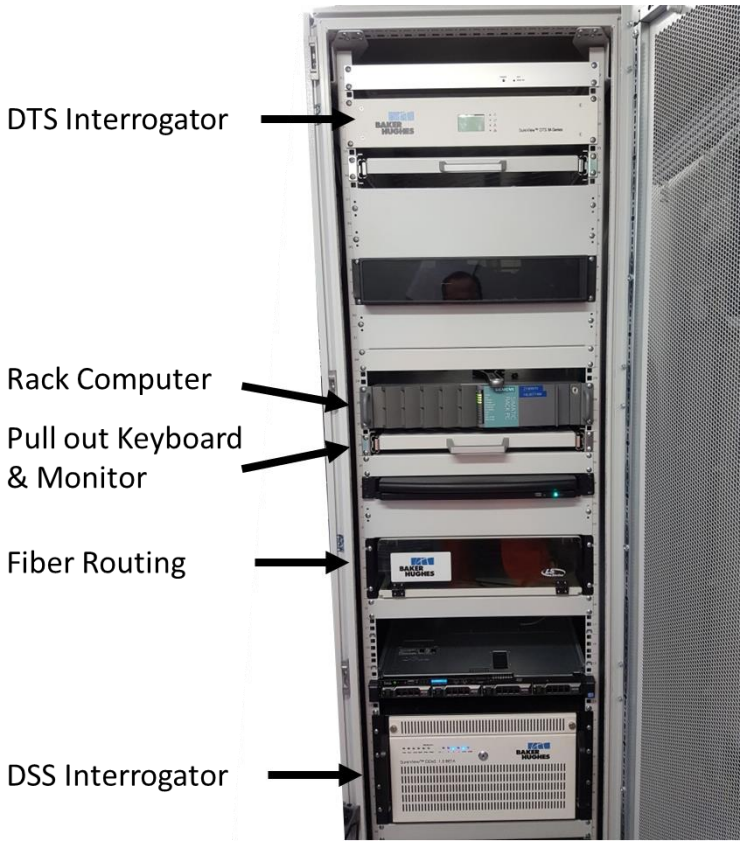

Figure 2.6: Equipment rack housed in the data cabin and the well site.

3. Cement Cure Monitoring

When finishing the installation of a permanent FO cable along a well the line must be cut to pass it through the tubing hanger. However, in this case, after the completion was landed the FO lines were re-connected at the surface through a temporary splice to enable DTS and DSS monitoring of the fibers during the cementing operation (see Figure 3.1). Monitoring the temperatures along the well during a cement cure is certainly not a common activity, and strain monitoring during such an operation is unprecedented in the industry. Therefore, this was a bit of an experiment to see if any important observations or learnings could be identified.

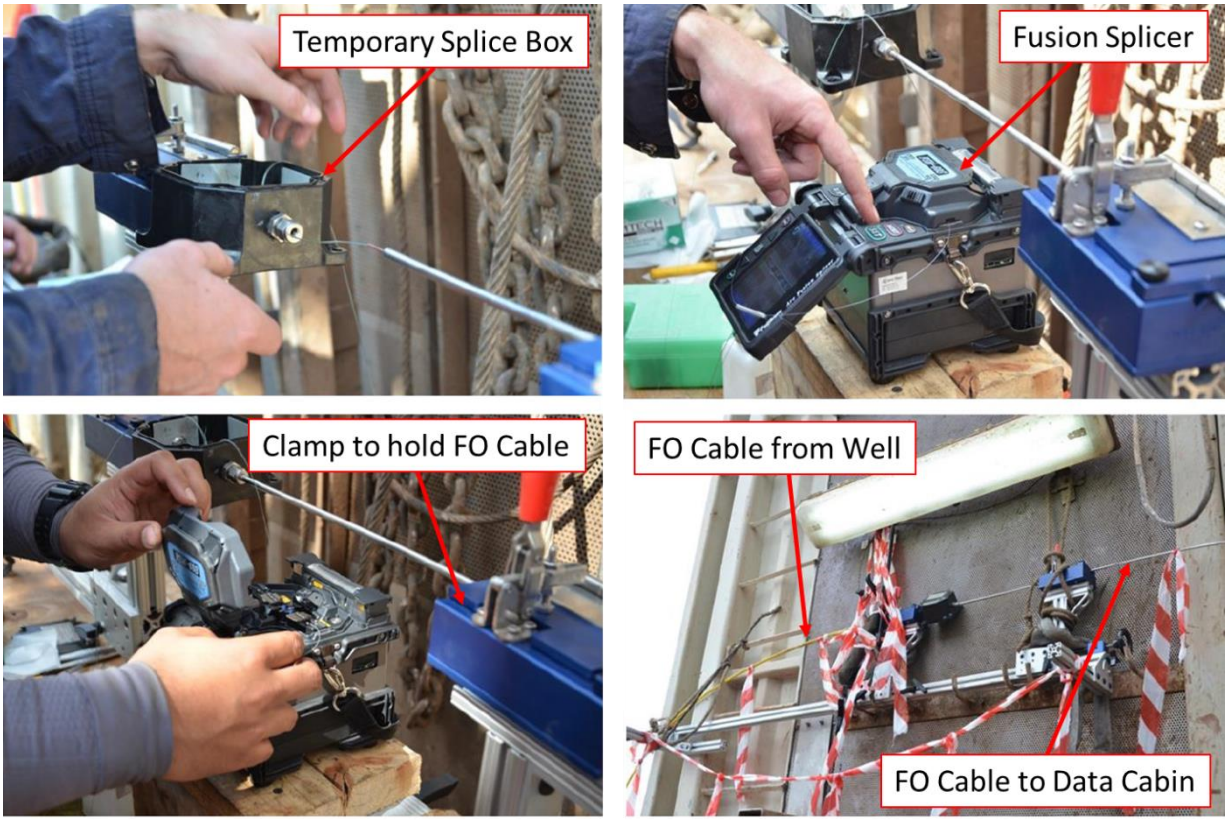

Figure 3.1: **Photographs of the temporary surface splice. The two cable ends were held in clamps (the blue boxes), spliced together, and fixed to the rig. The exposed fiber was coiled inside a temporary splice box.**

The FO lines were reconnected while the well was still circulating, ~5.5 hours prior to the start of cement pumping. The cement was then pumped for 2 hours and allowed to cure for ~29 hours, the wait on cement (WOC) period. This is summarized in Table 3.1, which shows a timeline of key events.

Table 3.1: Timeline of key events during the cementing operation.

Time (UTC)	Event
Aug 28, 2015 10:00	Landed completion
Aug 28, 2015 11:15	Commenced circulating
Aug 28, 2015 15:32	Begin FO monitoring
Aug 28, 2015 20:00	Stopped circulating
Aug 28, 2015 22:00	Started pumping Flexstone cement
Aug 29, 2015 00:15	Start Wait on Cement (WOC) period
Aug 30, 2015 05:30	Cut FO control line and lift BOP

Figure 3.2 shows the temperatures along the wellbore measured during the 38-hour monitoring period while the cement was curing. During the initial 9-10 hours the temperatures are heavily impacted by the circulation and pumping activities. However, during the WOC period the temperatures are primarily stable until approximately 11:00 on Aug 29 at which point the bottom of the well begins to increase in temperature dramatically due to the heat of hydration as the cement cures.

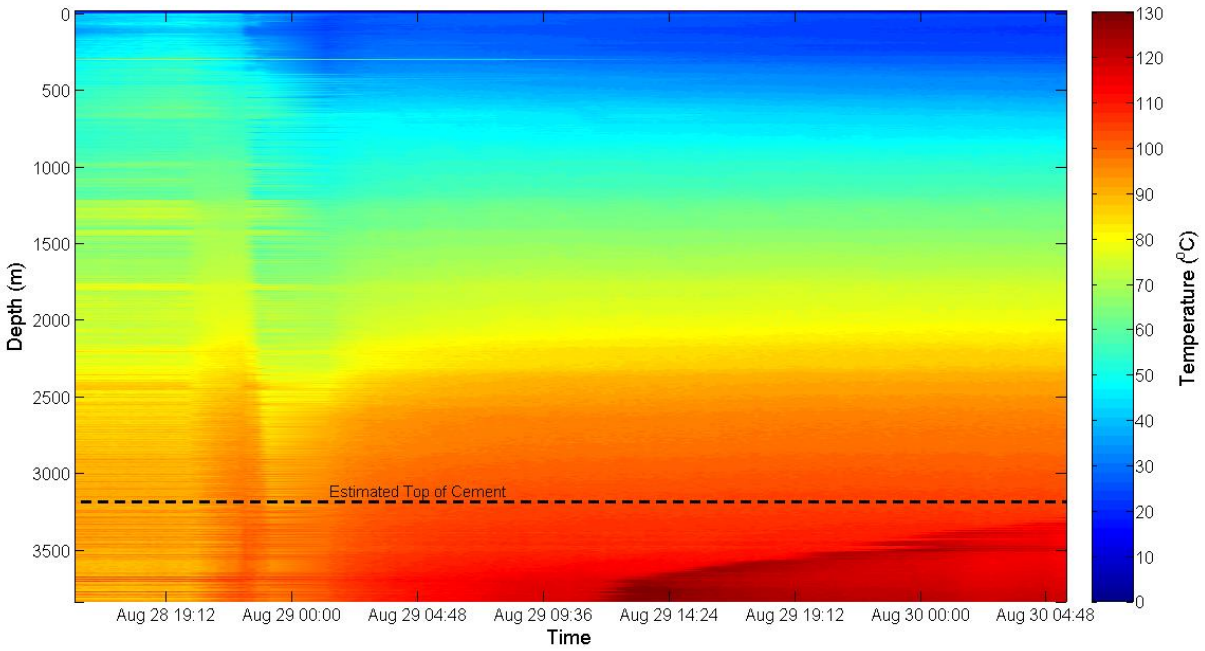

Figure 3.2: Absolute temperature measured along the wellbore during the cementing operation. The dashed horizontal line indicates the Estimated Top of Cement (ETOC) at 3200 m.

The heating is demonstrated more clearly in Figure 3.3 which shows the increase in temperature along the bottom portion of the well exceeds 20°C. The cement cure begins at the bottom of the well because the elevated temperatures deeper in the well accelerate the curing process. The curing process then proceeds up the cement column fairly linearly in time. A linear extrapolation of the heating process suggests that if the fibers had remained connected for an additional 3-4 hours the top of the cement might have been confirmed by the DTS data.

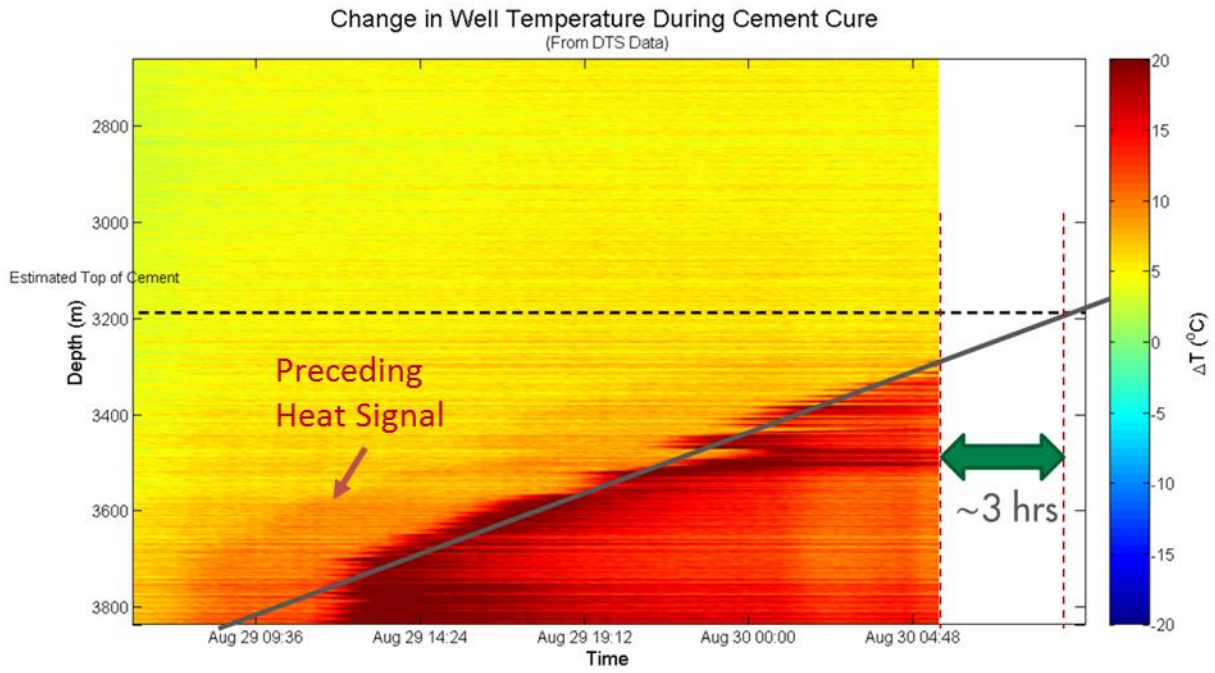

Figure 3.3: Change in measured temperature along the bottom of the well during the peak heating. The dashed horizontal line indicates the Estimated Top of Cement (ETOC) at 3200 m. The solid line represents a linear extrapolation through the peak heat of hydration. The faint heat signature preceding the primary heat of hydration is denoted by the red arrow..

The heat of hydration signal is more pronounced when observing the time derivative of the heating process. Figure 3.4 shows a plot of the change in temperature between successive scans (i.e., $\Delta T/\Delta t$ which is essentially a quantized time derivative). The onset of the heat of hydration 20 hours after the start of the monitoring period is clearly manifested and occurs at a rate of approximately 2°C per minute. It is noted that a deviation in the linearity of the heat of hydration curve occurs near the 7" casing shoe at 3500 mAHRT and is likely due to a change in the thermal properties of the well. It is also interesting to note the appearance of a faint heating signal that precedes the primary heat of hydration signal by ~4 – 5 hours. This is not unexpected as there are two hydration stages in the cement cure process.

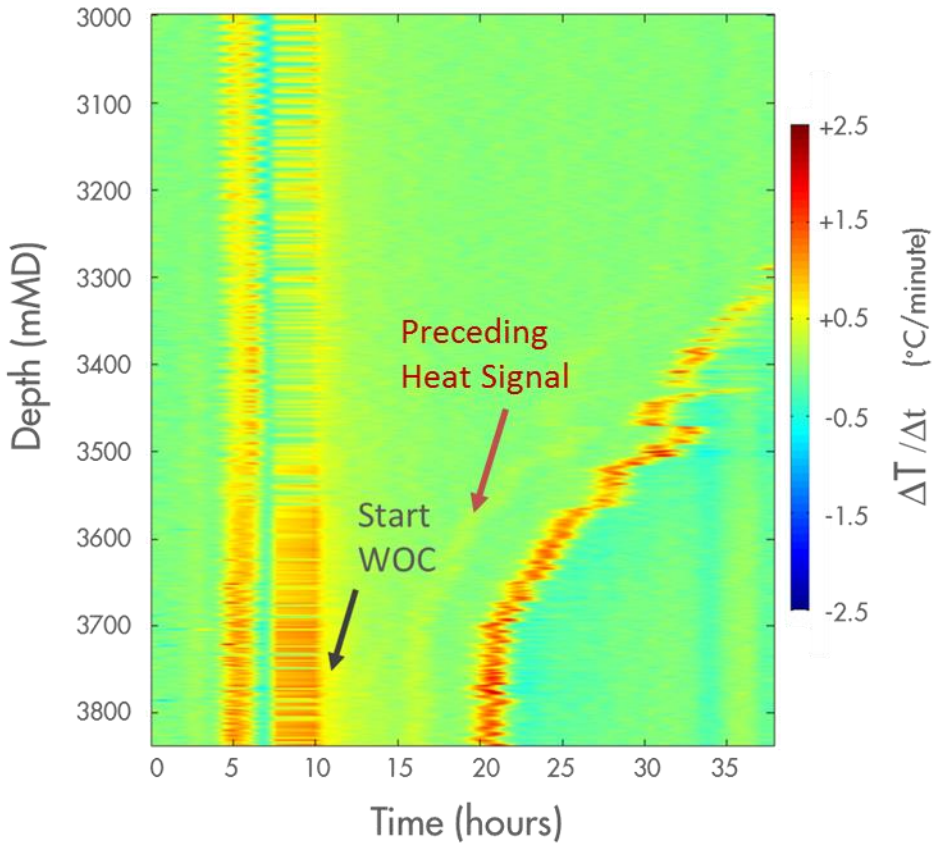

Figure 3.4: **Rate of change in the measured temperature as a function of monitoring time over the lower region of the well during the cement cure. The WOC began ~10 hours into the monitoring period. The faint heat signature preceding the primary heat of hydration is denoted by the red arrow. (The stripes in the data between t = 5 – 10 hrs are due to the circulation and pumping activities.)**

The DSS cable was also monitoring during the cement cure and Figure 3.5 shows a plot of the rate of change in the measured strain ($\varepsilon/\Delta t$) as a function of time. The quality of the DSS signal was much degraded compared to data obtained during a permanent monitoring configuration. Unlike the DTS data, the DSS signal is obtained through an interferometric measurement and is much more susceptible to vibrational noise. Nevertheless, the heat of hydration signal is clearly evident in the DSS data. Note that the data in the figure has not been temperature corrected and the heat of hydration signal is primarily associated with a temperature change. (The DSS measurement is sensitive to changes in temperature.) However, a legitimate compression signal is observed to form just below the 7" casing shoe at approximately the same time the heat of hydration signal reaches that location. It is not clear what is causing the strain, but it's possible the cable is thermally expanding at the lower depths and being compressed near the casing shoe where it is sufficiently fixed in place even before the cement has set.

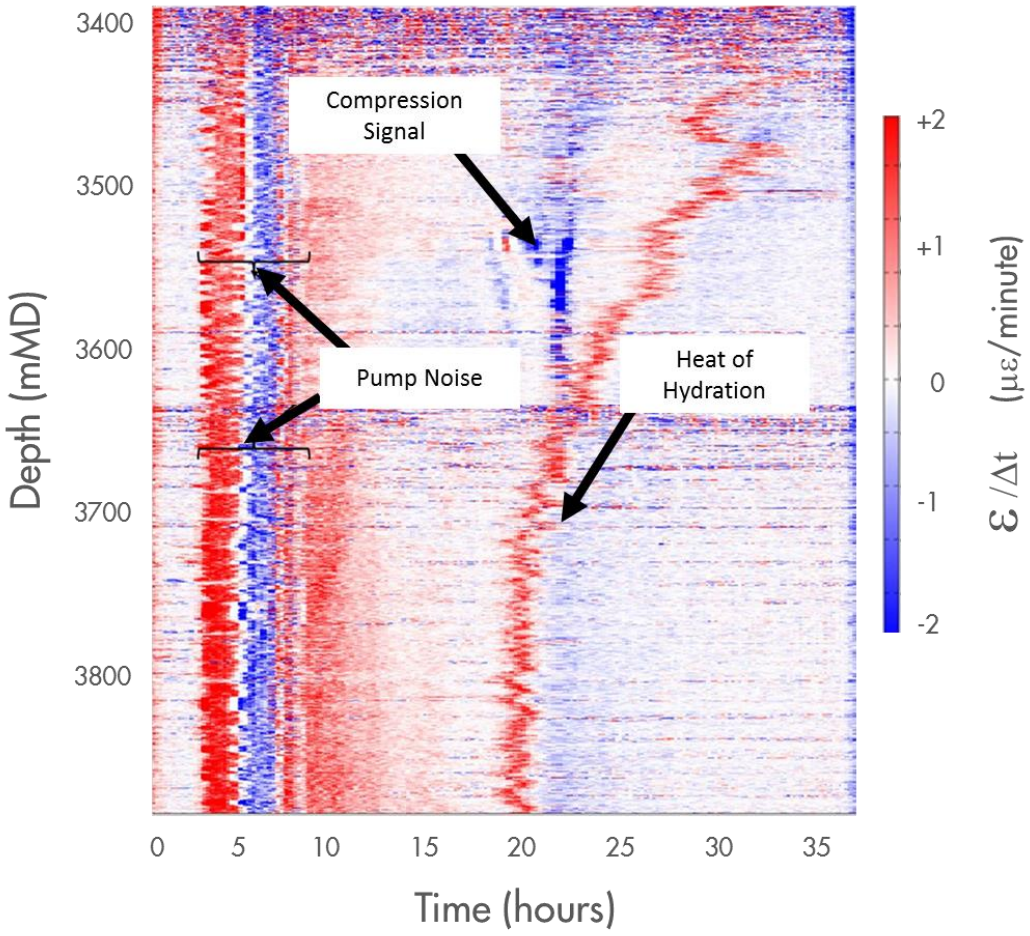

Figure 3.5: Rate of change in the measured strain along the DSS cable as a function of monitoring time. The WOC began ~9 hours into the monitoring period. Note that the strain data in the figure has not been temperature corrected.

The DTS data during cement curing also provides valuable feedback to the Well Fluids teams about the cement characteristics. A first comparison between the simulated and measured hydration times show good agreement. Currently, a more detailed examination is being performed that could ultimately lead to better calibration of such simulations and subsequently more accurate future predictions of cement curing (and wait-on-cement) times. Additionally, the DTS signals seem to reveal more character to the hydration depth profile which might hint at the effect of a changing heat exchange capacity with different formations. Signs of such effects can possibly be seen in Figure 3.5 around the gas-water interface in the well (~3567 mMD) where the hydration of the cement is slightly delayed in the gas-filled compared to the water-filled formations. The difference is rather small in the case of Zeerijp, however it might be significant under different circumstances. Such DTS data of processes like the curing of cement could identify the need for more detailed simulations and cement programs.

4. Observations from Temperature and Strain Monitoring

DSS monitoring in ZRP-3 began on Oct 12, 2015. Because the strain measurement is sensitive to changes in temperature, DTS data have also been acquired to provide the necessary thermal correction. The following sections present the primary observations from the DTS and DSS data.

4.1. DTS Results

Figure 4.1 shows the change in temperature along the well during the first five months of monitoring (Oct 12, 2015 – May 1, 2016). The shallow depths (< 1500 m) exhibit cooling during this initial time period, whereas the deeper depths (> 2000 m) undergo heating. It is likely that this behavior is the result of the near the wellbore environment returning to its original geothermal gradient after being disturbed by the drilling process. (Note that the well was completed 6 weeks prior to the start of monitoring.) During drilling, the deeper zones are cooled and the shallow depths are heated as the drilling mud is circulated in the wellbore. This would produce the representative geothermal gradient depicted in Figure 4.2.

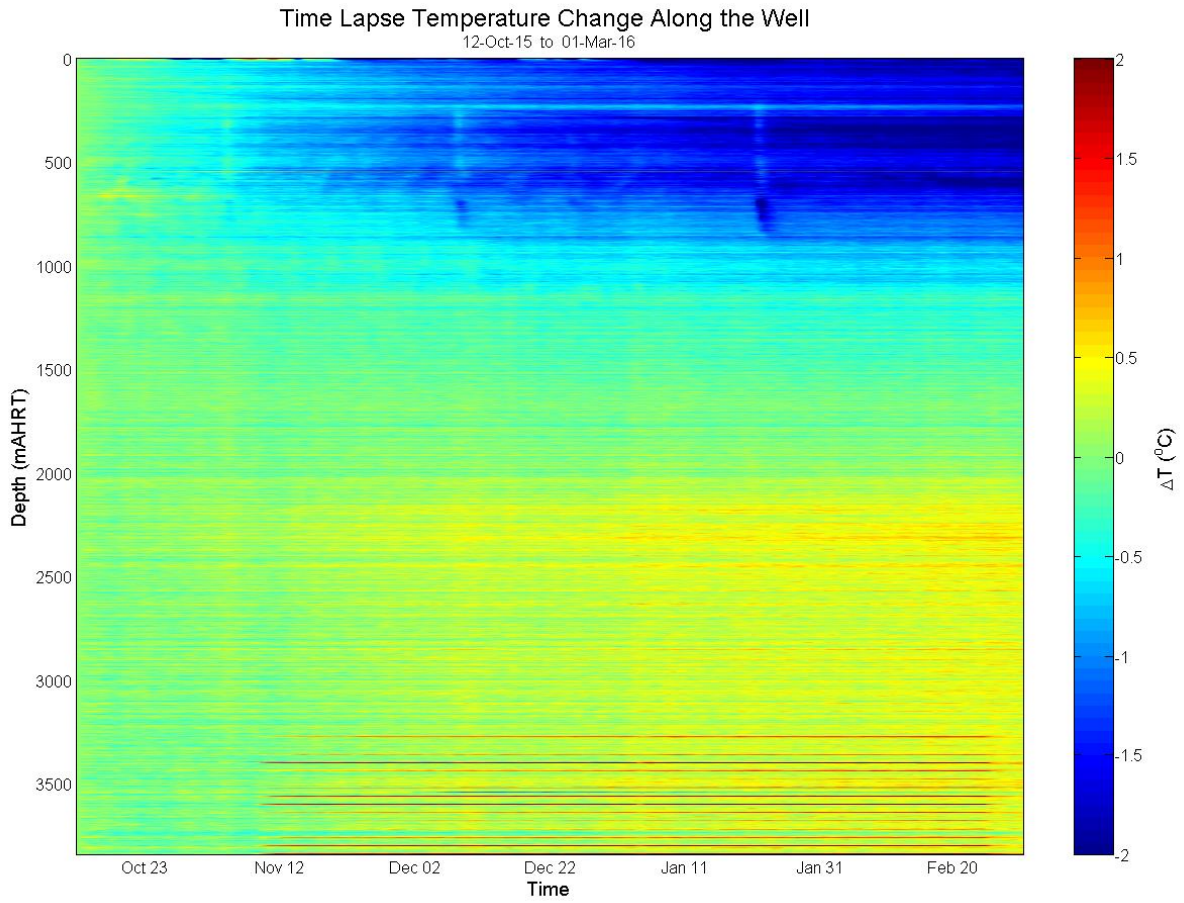

Figure 4.1: Change in temperature along the well during the first five months of monitoring (Oct 12, 2015 to May 1, 2016).

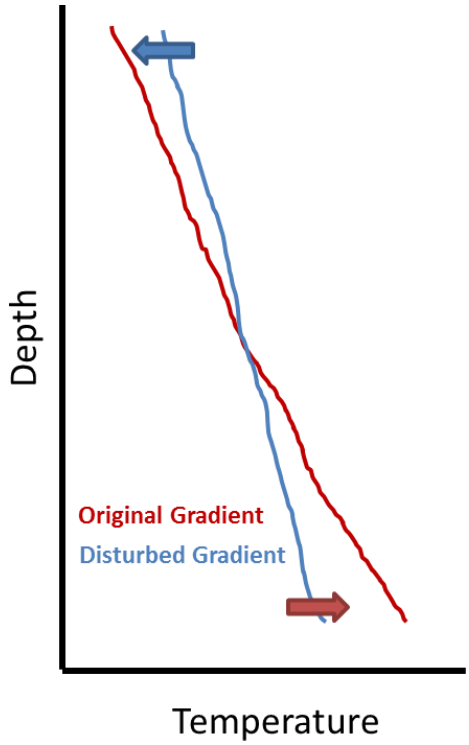

Figure 4.2: **Conceptual representation of the change in the geothermal gradient in the near-wellbore environment after being disturbed by the drilling process. The arrows indicate the direction of the change in temperature during the rethermalization process.**

If the behavior in Figure 4.1 is indeed explained by a return to the natural geothermal gradient, then it may seem surprising that the process would continue for so long. However, during conductive heat transfer, the rate of temperature change is proportional to the temperature differential. Therefore, the tail end of the thermal stabilization process where the remaining temperature difference is < 1°C can take quite a long time. Indeed, such long relaxation times have been observed in geothermal fields [18] and have been predicted in simulations[19] and analytical solutions [20],[21]. In addition, as a monitor well, the lack of flowing fluids in the wellbore might also make the rethermalization process more noticeable.

It has been identified in the past that the slow temperature equilibration leads to a general underprediction of the true formation temperatures when using temperature logs from drill stem tests or formation pressure tests. Many different ways to correct for these temperatures have been created, some of which are listed in [22], and corrections of 10% are not uncommon.

An estimate of the actual formation temperature can be obtained by plotting the temperature against time on a Horner type plot. The Horner time ratio on the x-axis is defined as (t+dt)/dt, where we chose t as the time that has elapsed between the completion of the well and the start of the DSS data (t = fixed), and dt is the time that has elapsed since the start of recording the DSS data. An example of the DTS data measured at 3800 mAHRT in the Zeerijp-3 well is shown in Figure 4.3, similar to

those done for geothermal fields in [18]. The full time span in the figure from (t+dt)/dt = 1000 to (t+dt)/dt = 100 is 185 days (note that increasing time runs from right to left along the horizontal axis). The temperature is slowly increasing over time, where the slope of the data in such a logarithmic plot depends on the heat flow rate, thermal conductivity, and geometry. When extrapolated to dt = infinity, one can assume the system to be in thermal equilibrium such that the wellbore temperature is equal again to the original formation temperature. In the data here, the eventual reading of the DTS is expected to be 125°C, which is approximately five degrees (or about 4-5%) higher than that seen on wireline logs.

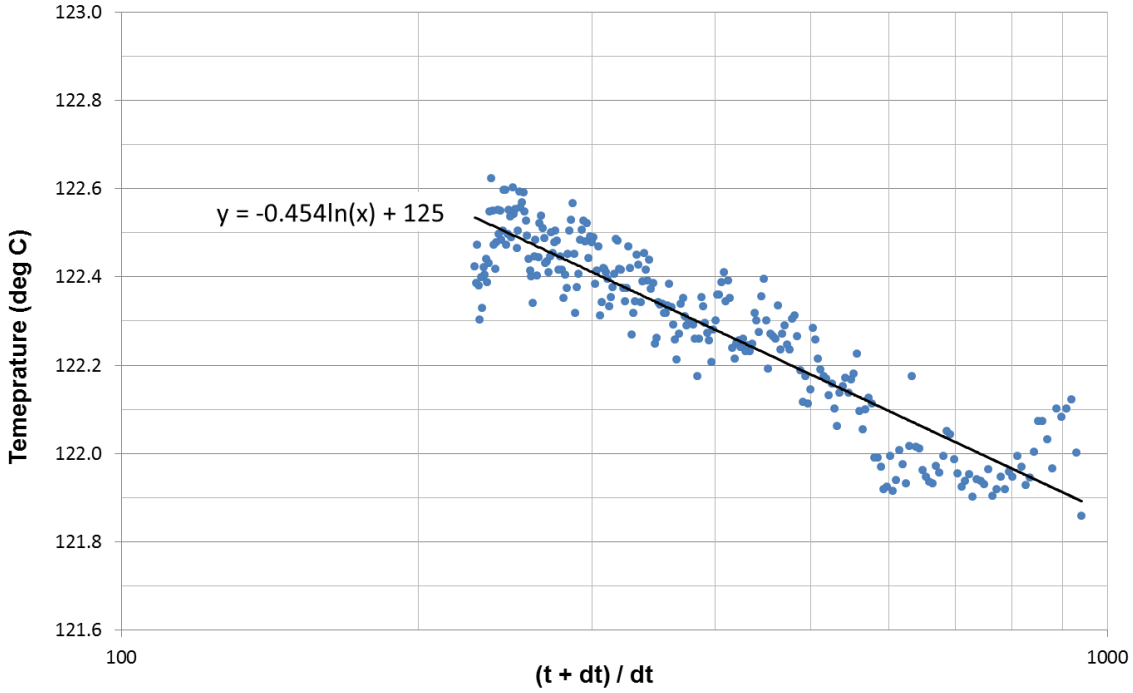

Figure 4.3: Horner type plot of the DTS temperature at a depth of 3800 mAHRT (averaged over 10 m intervals). Time dt is the elapsed time since the end of circulation prior to pumping cement. The black line represents a logarithmic fit to the data.

A series of horizontal stripes are observed near the bottom of the well in Figure 4.1 beginning in early November, 2015 and lasting until February, 2016. This signal is seen more clearly in Figure 4.4 which displays the temperature change during the first year of monitoring along the portion of the well where the strain cable was installed. The stripes occur at the depths of the geophones in the well which cause localized heating when powered on. As indicated by the regularity of the observed heat signature, the geophones are spaced at 40 meter intervals and are located within 1 meter of the depths declared by the vendor. The power supply for the geophone array is located at the bottom of the tool string and can be identified by a very dark zone of heating. Though saturated on the scale of the plot, the temperature increase at the depth of the power supply is >30°C. The

geophones suffered a failure in February, 2016 after which the associated heat signature is no longer observed (except at the depth of the power supply where the temperatures were much higher and take longer to return to ambient.)

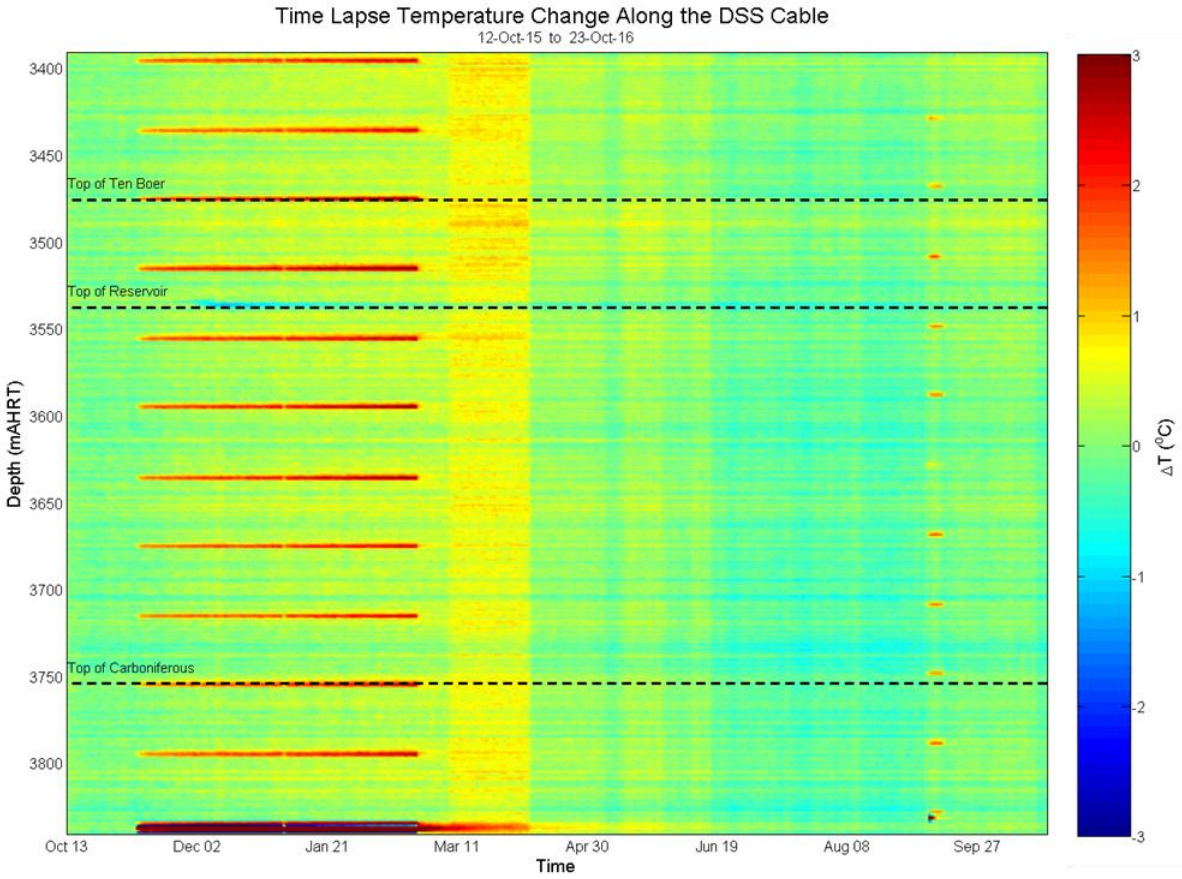

Figure 4.4: Change in temperature along the portion of the well monitored by the DSS cable during the first year of monitoring (Oct 12, 2015 to Oct 23, 2016).

The temperatures at the depths of three different geophones are displayed in Figure 4.5. After the initial onset of the increase in temperature (which lasts several days), the temperature is observed to slowly but steadily continue to rise during following 4 months before the failure. The temperature (behind the casing at the location of the DTS cable) increased by approximately 2 – 3°C during this timeframe.

After being repaired by the vendor, the geophones were reinstalled and powered on briefly in September, 2016 before failing again. The renewed heating can be seen in Figure 4.4. Though difficult to see on the scale of the plot, the geophones were installed 7 meters shallower than before and, consequently, there is a constant 7 m shift in the heat signature relative to the initial installation. The reason for the change in depths is that the bottom of the well had filled with debris and the geophone array could not be lowered to the original depth.

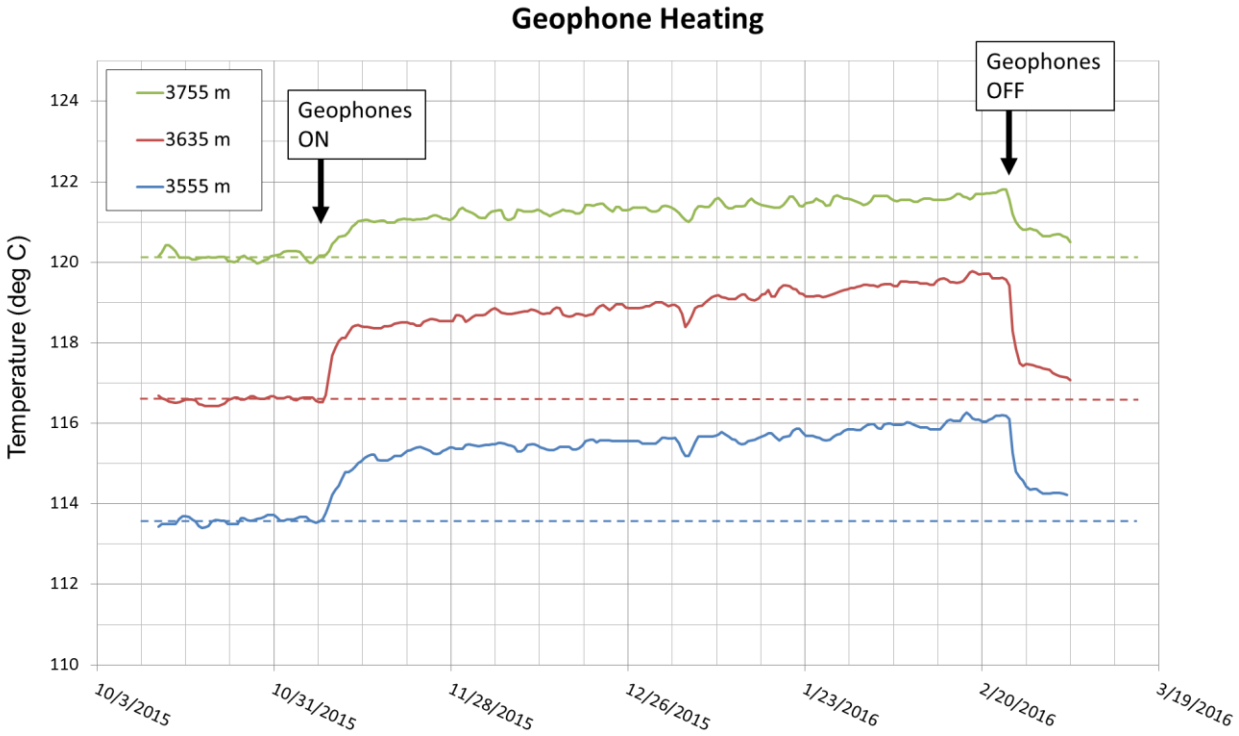

Figure 4.5: Temperature measurements at the depths of three separate geophones. The times at which the geophones were turned on and off are indicated by the arrows.

Also evident in Figure 4.4 are abrupt changes in temperature across all depths beginning in early March, 2016 that manifest as 'vertical striping' on the plot. This behavior is demonstrated more clearly in Figure 4.6 which shows the change in the average of the measured temperatures across the reservoir interval during the first year of monitoring. The measured temperature is seen to increase until early March, 2016 at which point the temperature dramatically and abruptly increases. The jump in temperature corresponds with the activity in the data cabin at the well site during which personnel where entering the cabin to deal with the failed geophones. The change in cabin temperature affected the temperature of the DTS unit itself which, in turn, affects the temperature measurement. The sensitivity of the DTS measuring on the temperature of the DTS interrogator is a known phenomenon common to all DTS units (sometimes referred to as 'temperature feed through'). It is difficult to fully compensate for this effect and the changes in measured temperature beginning in March, 2016 are erroneously caused by the remnant of the inadequate compensation.

The internal reference temperature of the DTS unit is also included in Figure 4.6 and clearly demonstrates a strong correlation to the changes in measured temperature. Nearly all of the abrupt changes in measured temperature can be associated with the activity log of personnel entering the data cabin. The one notable exception occurred on April 5, 2016 when the DTS interrogator's averaging setting was changed. There is a large decrease in measured temperature, but only a small change in the DTS reference temperature.

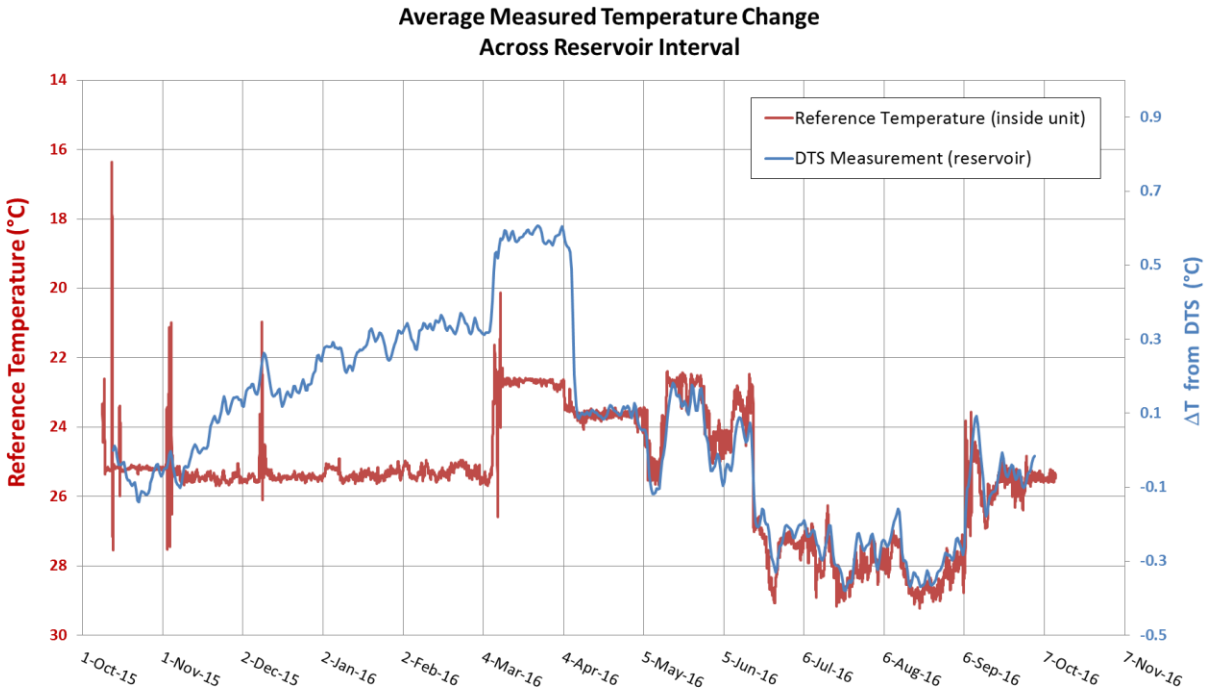

Figure 4.6: Change in the average of the measured temperatures across the reservoir interval (blue) and the internal reference temperature of the DTS unit (red) during the first year of monitoring.

From the data in Figure 4.6, it is concluded that the measured temperature change in the well prior to March 2016 is probably real; however, afterwards the temperature has likely been constant and the change in the measurement is erroneous.

Further evidence of this assumption is provided in Figure 4.7 which shows the measured temperature change at several selected depths along the well. Note that the jump in measured temperature that occurred when the data cabin was first entered in March of 2016 becomes much more pronounced with increasing depth. This is due to the deterioration in signal quality with increasing fiber distance associated with the DTS measurement. The previously mentioned difference in thermal behavior in the shallow and deep zones during the early months of monitoring is also apparent in the figure. However, during the second half of the year (indicated by the dashed box) the temperature change is the same at all the depths. This is demonstrated in the inset to the figure in the data at each depth has been vertically shifted by a constant offset such that they all overlay.

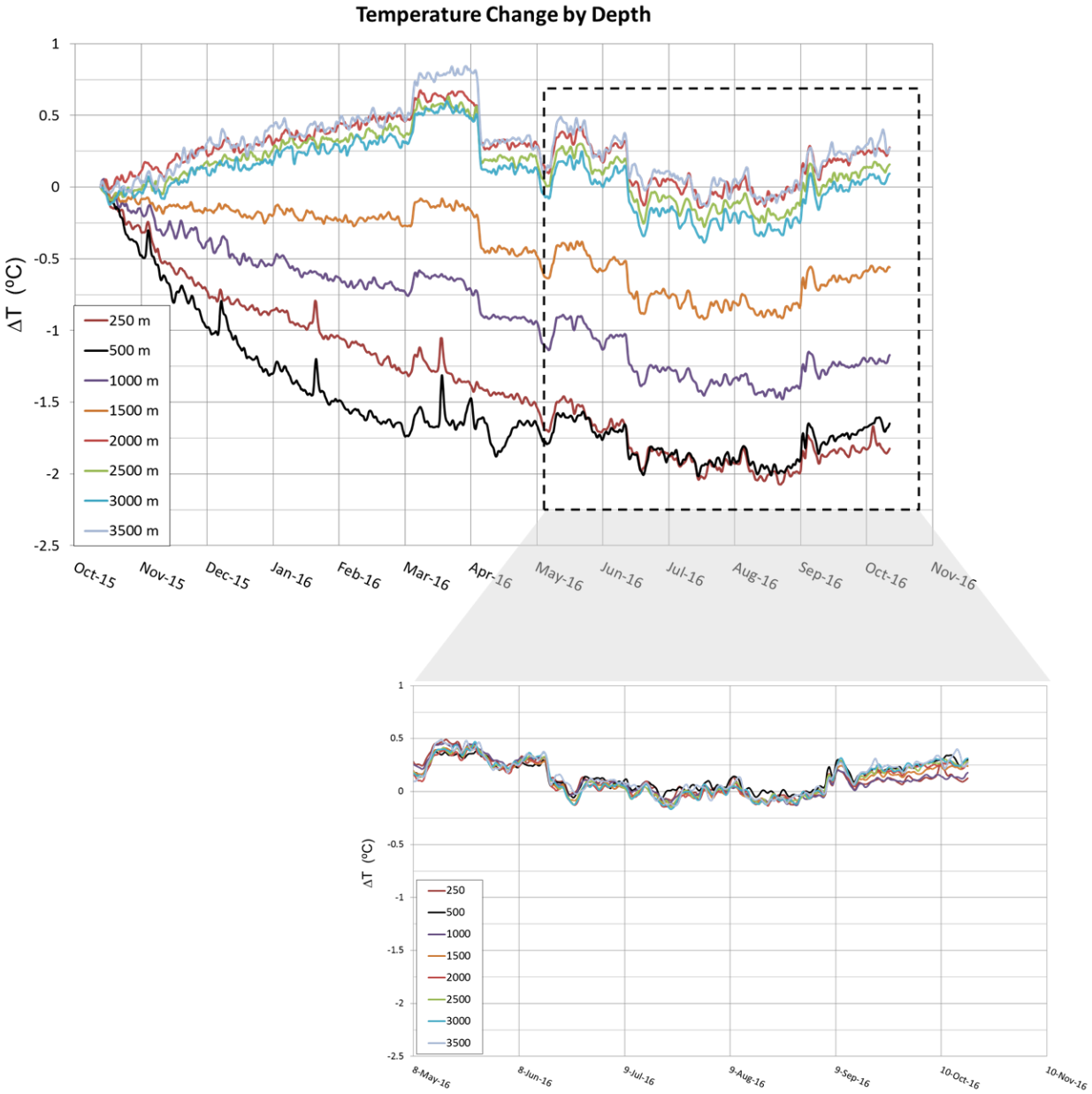

Figure 4.7: **Change in measured temperatures at the depths indicated. The data within the time interval indicated by the dashed box are displayed with a vertical offset in the inset such that the curves overlap.**

Under the assumption that only the temperature data during the first ~5 months is valid, a synthetic temperature curve was created for each of the major lithological zones spanned by the DSS cable. The synthetic data fits the early-time temperature increase and then remains constant through the interval during which the measurements are affected by the temperature feed through, see Figure 4.8. The synthetic temperature curve is used for the temperature correction of the strain data.

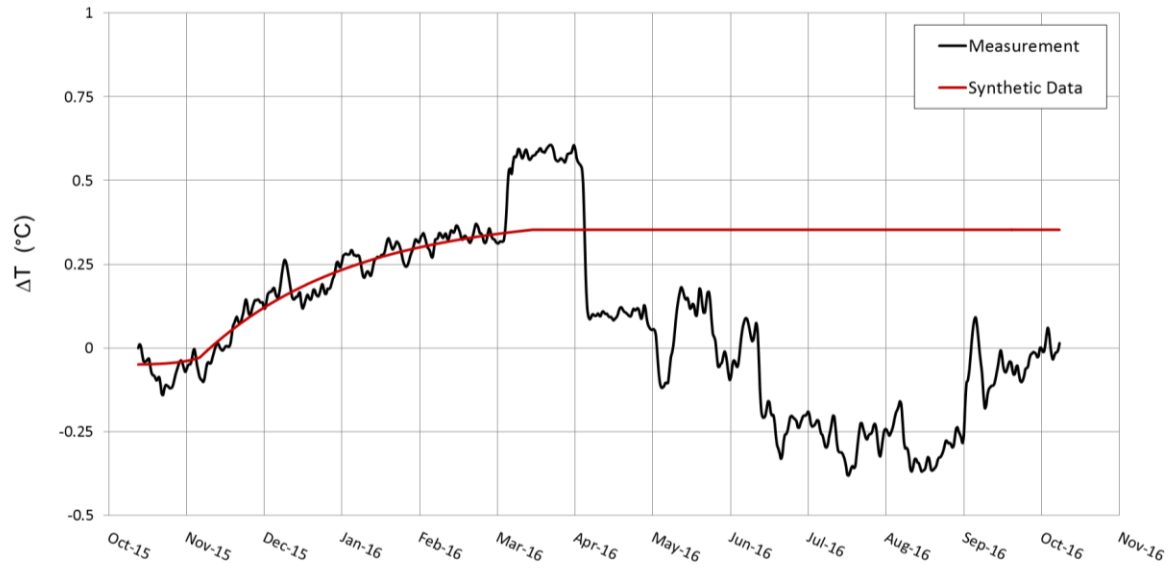

Figure 4.8: Change in the average of the measured temperatures across the reservoir interval (black) and the synthetic temperature data (red) used for the thermal correction of the strain data.

4.2. Strain Profile

4.2.1. Overview

The strain evolution along the portion of the well monitored by the DSS cable is shown in Figure 4.9. The black horizontal dashed lines indicate the depths of the top of the Ten Boer, Reservoir, and Carboniferous zones. The figure also includes a log plot of the total strain accumulated during the first year of monitoring (red curve). Because the strain changes rapidly with depth, a heavily smoothed version of the data (black curve) has been added to aid in the visualization of the average strain behavior along the well. The curvature signal is negligible along the entire length of the cable; therefore, the measured axial strain data can be simply regarded as a purely vertical strain (since it is a vertical well). From the data it is apparent that the strain, though quite inhomogeneous, is predominantly compressive and has been growing over time. However, it can also be seen that the strain profile is positive in many places along the cable, indicating regions of tension. Furthermore, the strain is not limited to the reservoir interval. In fact, most of the cable exhibits a notable degree of strain. The primary exception occurs over the bottom ~75 meters of the 7" casing (the shoe is located at 3500 mAHRT). This region shows very little strain and remains 'green' on the color plot in Figure 4.9. Because the top 109 meters of the DSS cable resides between casing strings it is reasonable to question the possible impact of this configuration on the strain measurement.

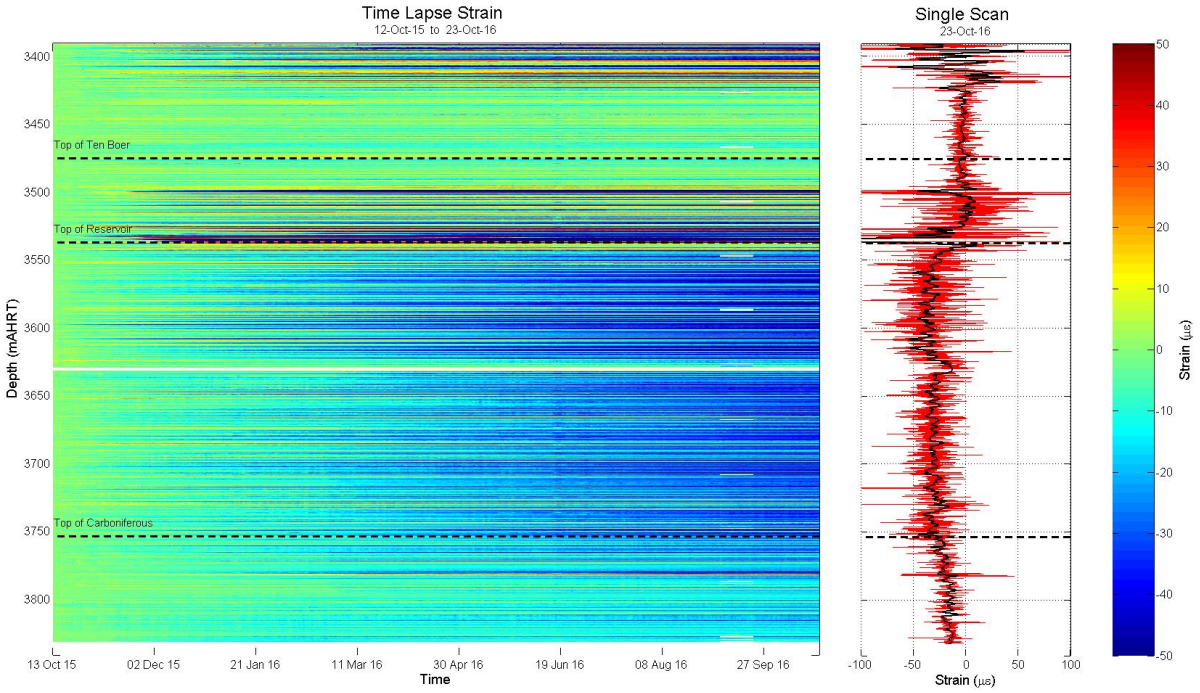

Figure 4.9: **(Left) Strain measured along the DSS cable during the first year of monitoring (Oct 12, 2015 – Oct 23, 2016). (Right) Strain along the cable measured on Oct 23, 2016. The black curve represents a heavily smoothed version of the data to aid in visualization of the average.**

Figure 4.10 shows the strain profile across the upper 125 meters of the DSS cable. A zonation track and a depiction of the well configuration are also included in the figure. The strain measured between the two casing strings is not entirely negligible. Indeed, some of the largest strains are measured in this region, across the upper 33 meters of the cable. This indicates that there is an adequate degree of strain transfer taking place through the outermost casing. Furthermore, it is interesting to note that the transition from large strain to minimal strain occurs exactly at a lithological boundary (~3424 mAHRT). In fact, the four zones in the Zechstein salt below this interface are treated as one single anhydrite block in the seismic velocity model. It is perhaps not surprising then that strains in these zones behave similarly to each other and quite different from the overlying zone.

The bottom of the region exhibiting minimal strain ends at another lithological boundary within the Ten Boer Claystone (~3500 mAHRT). Therefore, though not definitive, the observation that the strain appears to be changing with lithology suggests that the measurement is indicative of real formation strains and not significantly impacted by being located between casing strings. There does, however, appear to be a large strain anomaly right at the 7" casing shoe, as seen in Figure 4.10. It is unclear if the measurement reflects the true strain in the formation (perhaps caused by the upset in casing profile) or if the signal is merely the result of some interaction between the cable and the completion hardware at this location. It is also noted that most of the strain at the casing shoe

developed during the first 6 months of monitoring (which began approximately 4 months after the casing shoe was installed) and has changed very little since then.

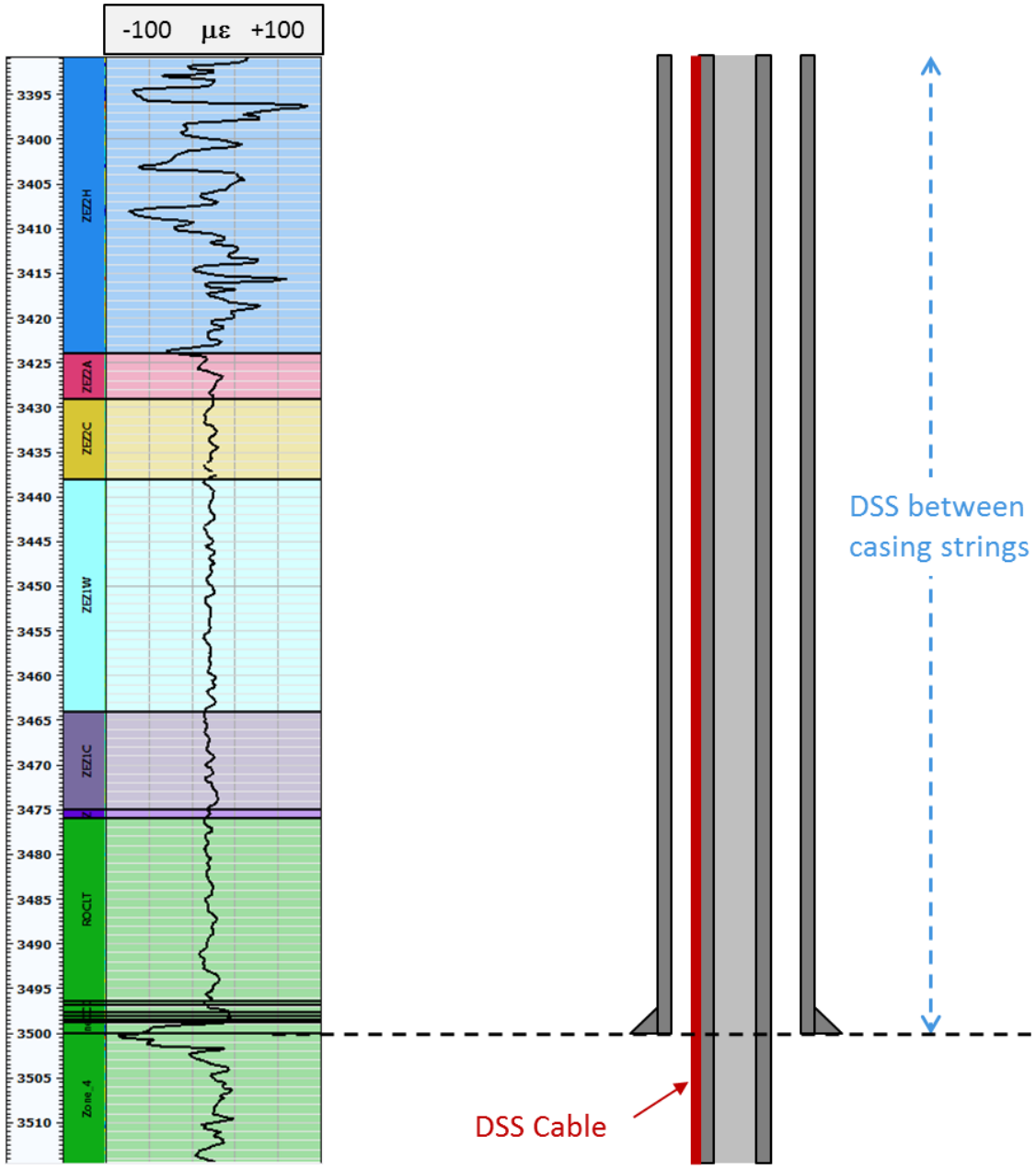

Figure 4.10: **Strain profile and zonation over the upper 125 m of the DSS cable. As indicated by the diagram on the right, the top 109 m of the cable is located above the 7" casing shoe and is therefore between casing strings.**

4.2.2. Dynamic Event in the Ten Boer Claystone

As shown in Figure 4.11, there is another significant strain anomaly located near ~3535 mAHRT, at the bottom of the Ten Boer. Unlike the strain signal at the casing shoe, there is no identified hardware associated with this signal. Additionally, the onset of the signal is quite rapid compared to the timescale of the development of the other strains. The strain profile within the interval ~3530 – 3540 mAHRT initially developed in a similar fashion to the strain along the rest of the cable; however, during a period of approximately 2 weeks near the end of November, 2015 the strain behavior changed dramatically. Some regions exhibited a tremendous increase in their rates of compaction or extension. Other regions, however, experienced a complete reversal of strain behavior; i.e., compaction became tension and vice versa. By combining the signal from the two opposing DSS fibers in the cable, it has been verified that these events are indeed predominantly axial strains and show very little bending. In addition to the strain development, there was simultaneously a notable decrease in temperature near the depth of the largest strain feature. In Figure 4.11, three depths have been selected that demonstrate this behavior and (in the top plot) are identified by the white dashed lines. The bottom plot in the figure displays the measurements at these depths as a function of time.

The strain measurements at 3533.01 and 3535.78 mAHRT indicate that the initial compaction rates at these two depths were similar. However, after ~Nov 21, 2015 the strain rate at 3533.01 mAHRT reversed sign and the formation at that depth began to be drawn into tension. Afterwards, no further significant strain developed at this depth. At the same time, the compaction rate at 3535.78 mAHRT dramatically increased (by a factor of ~50) after which it returned to its original compaction rate. Approximately, one week after the onset of change in compaction behavior there was sharp decrease in temperature in this interval. The data plotted in Figure 4.11 were taken from the depth of maximum temperature change (~1.5°C). Near the end of the transient strain anomaly, the temperature began to slowly increase and after ~4 months had returned to its original temperature. Though the change in temperature was temporary, the strain measurement suggests that the mechanical deformation is permanent.

It is not clearly understood what occurred to cause the strain and temperature to change so dramatically over such a relatively short period of time. It is known that there are isolated gas pockets within the Ten Boer Claystone. One possibility is that there was a shift in the formation (perhaps due to a post-drilling settling process) that enabled the release (and expansion) of a limited volume of gas which resulting in a Joule-Thomson cooling effect. However, because the DSS measurement is new, there is little experience to know for certain how various suspected subsurface phenomena would manifest in the data.

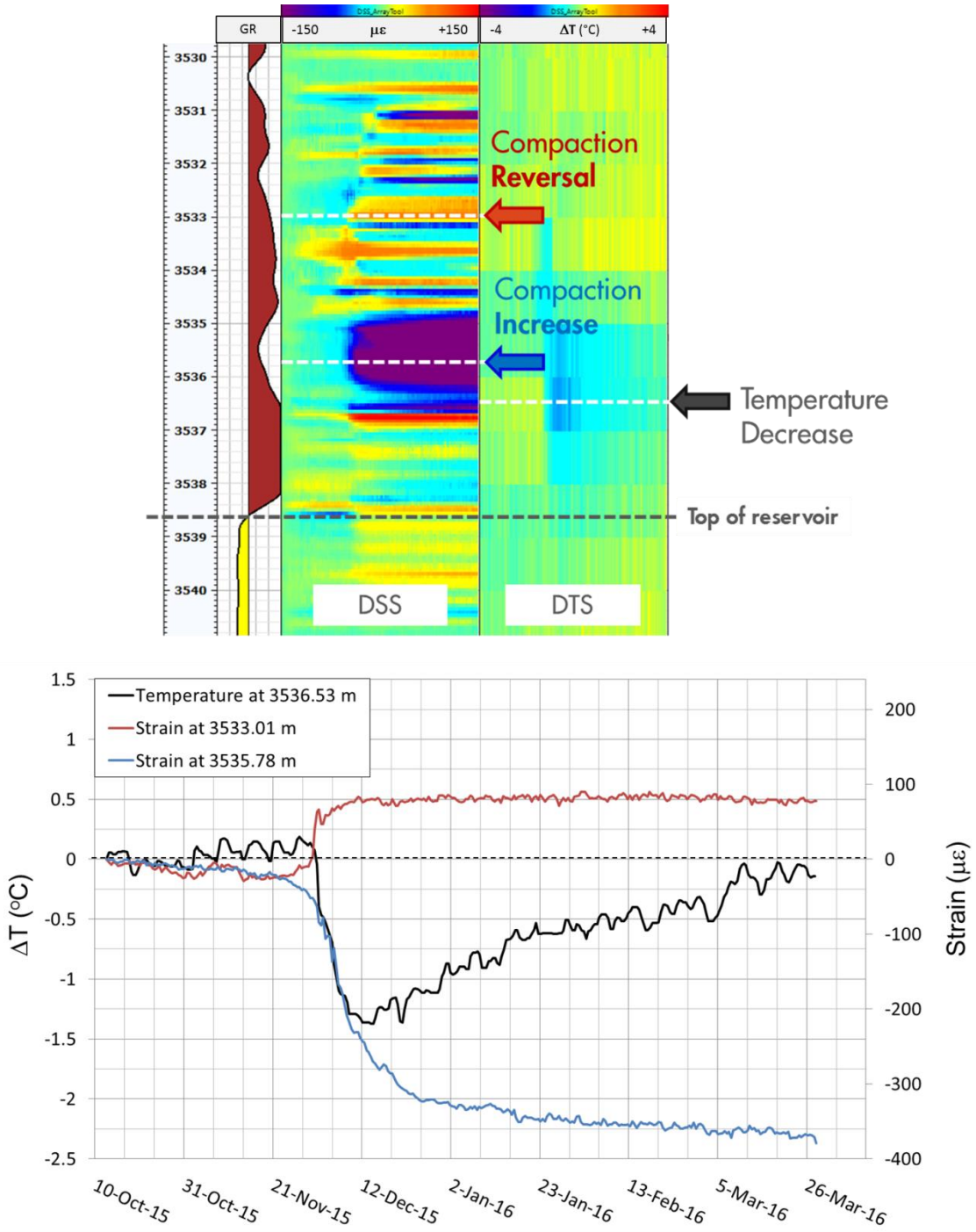

Figure 4.11: **(Top) Log plot of the strain anomaly near the bottom of the Ten Boer Claystone. The tracks on the right show the time evolution of the strain profile and temperature change measured by the DSS and DTS systems during the first 5 months of monitoring (Oct 12, 2015 – Mar 7, 2016). The gamma ray log is displayed in the left-hand track. (Bottom) Strain and temperature at the indicated depths, shown in the legend and marked by the white dashed lines in the top plot, as a function of time. Each minor division is 1 week.**

4.2.3. Tension Bands

The strain profiles shown in the previous figures highlight regions of interest that are not necessarily representative of measurements across most of the monitored interval. In contrast, Figure 4.12 displays the strain along a typical 25 meter interval of the reservoir during the first 6 months of monitoring. The gamma ray log indicates the interval is comprised of fairly clean sands. The data show that the strain profile consists of bands of both compression and tension. As shown in the inset to Figure 4.12, in many places these bands alternate between compaction and extension on a spatial scale of a few tens of centimeters.

Anecdotally, the observation of tensile bands within the reservoir has come as a surprise to some people but is fully expected by others (for the latter, see e.g. [24], where simulated GR marker response in depleting layers interbedded with impermeable layers show expansion signals at the intervals of unproductive confining rocks). In either case, there does not seem to be a consistent consensus regarding their explanation. No tensile bands were observed during laboratory compression tests (see Appendix 2), suggesting that they are not merely an artifact of the cable functionality. Careful observation of the development of the strain log on the left-hand side of Figure 4.12 reveals that many of the tensile bands decrease in magnitude over time (i.e., the bands of yellow fade to green or blue). This behavior is shown more quantitatively in Figure 4.13 which displays the time evolution of the strain at the depths of several selected tensile bands within the reservoir. The tension signals vary significantly in magnitude, growth rate, and decay rate. By the end of the first year of monitoring a few regions were still under a notable degree of tension; however, most had gone into compression.

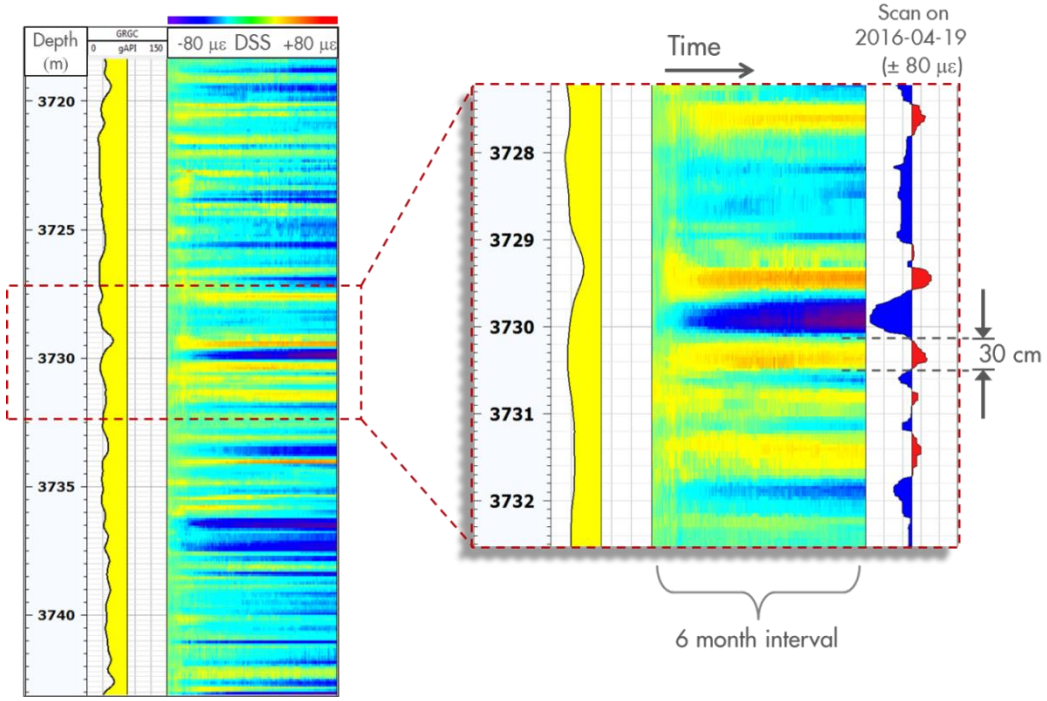

Figure 4.12: Plot of the strain along a 25 meter interval of the reservoir during the first 6 months of monitoring (October 12, 2015 – April 19, 2016). The gamma ray

log is included in the left-hand track. The inset displays an enlarged view of the boxed region on the log.

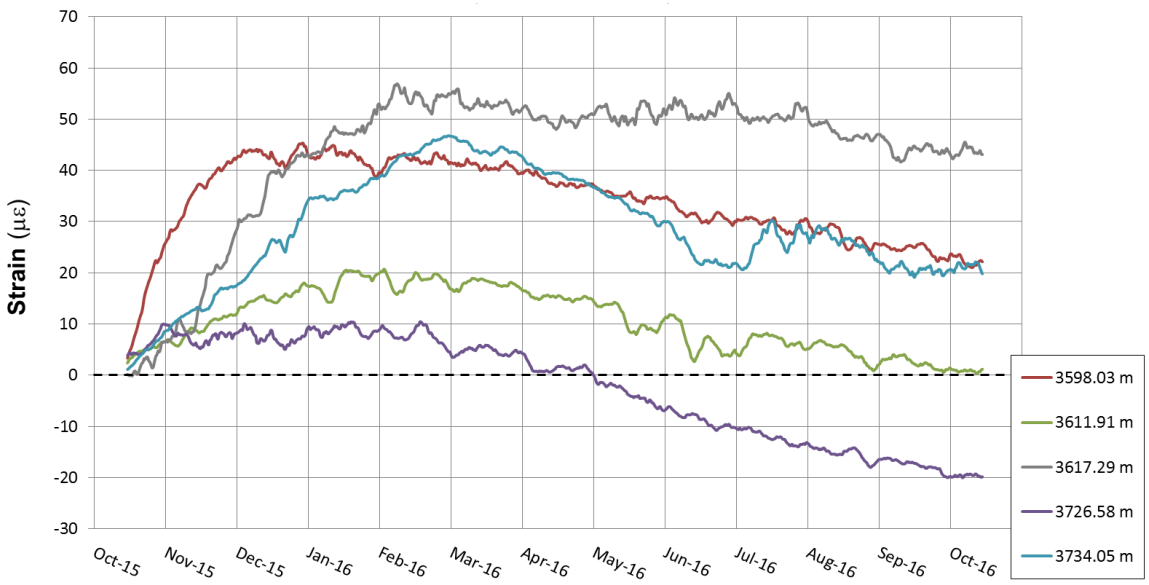

Figure 4.13: Time evolution of the DSS measurement at selected depths within the reservoir during the first year of monitoring (Oct 12, 2015 – Oct 23, 2016).

It is also interesting to note that though tensile strain is observed to some degree across the entire monitored interval, the behavior is not the same in each lithological zone. For instance, Figure 4.14 displays a side-by-side comparison of the strain profiles measured over representative intervals within the Reservoir and Carboniferous zones during the first six months of monitoring. The strain in the Carboniferous underburden appears to be much more homogeneous than in the reservoir. Additionally, though it does exhibit a general decreasing tensile signal, the bands of tension and compression in the Carboniferous zone are significantly reduced in magnitude.

Despite the relatively muted tensile signal in the Carboniferous zone, there are still a few (< 5) prominent tension bands and, in contrast to the primary behavior in the reservoir, the magnitude of the tensile signal in these bands has increased over the year of monitoring. Figure 4.15 shows the strain profile over a 25 meter interval in the Carboniferous zone that contains two prominent tension bands near 3782 mAHRT. As can been in the inset, the tensile signal at these two depths has grown steadily over the monitoring period.

Similarly, the bands of tension observed at the top of the cable in the Zechstein Salt and in the Ten Boer Claystone have generally not decreased over time either. Figure 4.16 displays the strain profile across the upper 25 meters of the monitored interval in the Salt during the first year of monitoring. Inspection of the colormap reveals that, for the most part, each band of tension and compression generally increases in intensity over time. The behavior in the Ten Boer is similar.

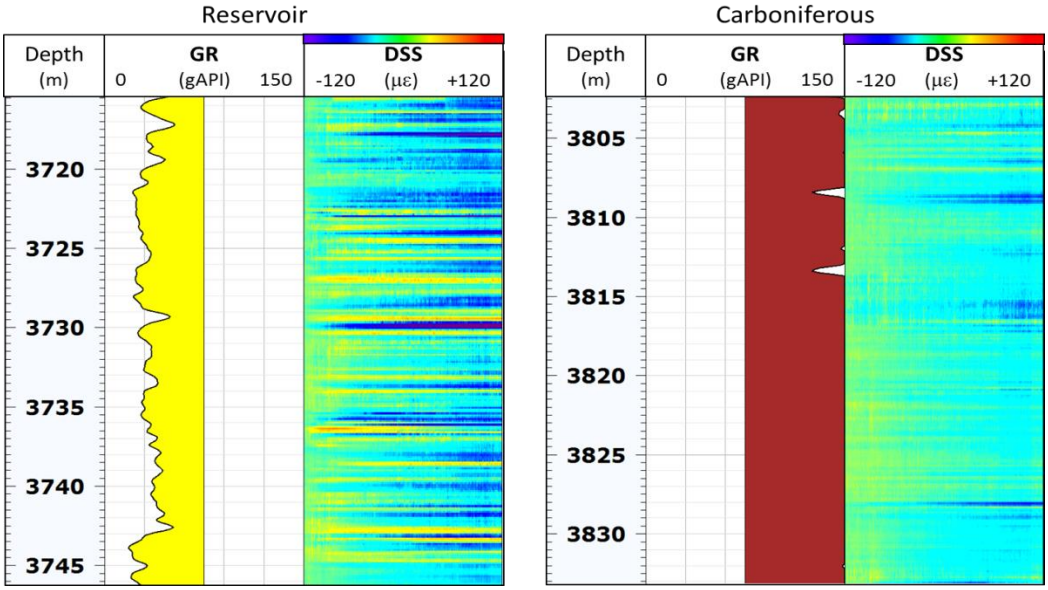

Figure 4.14: **Comparison of the strain profiles over typical 25 meter intervals in the Reservoir (left) and Carboniferous (right) during the first 6 months of monitoring (October 12, 2015 – April 19, 2016).**

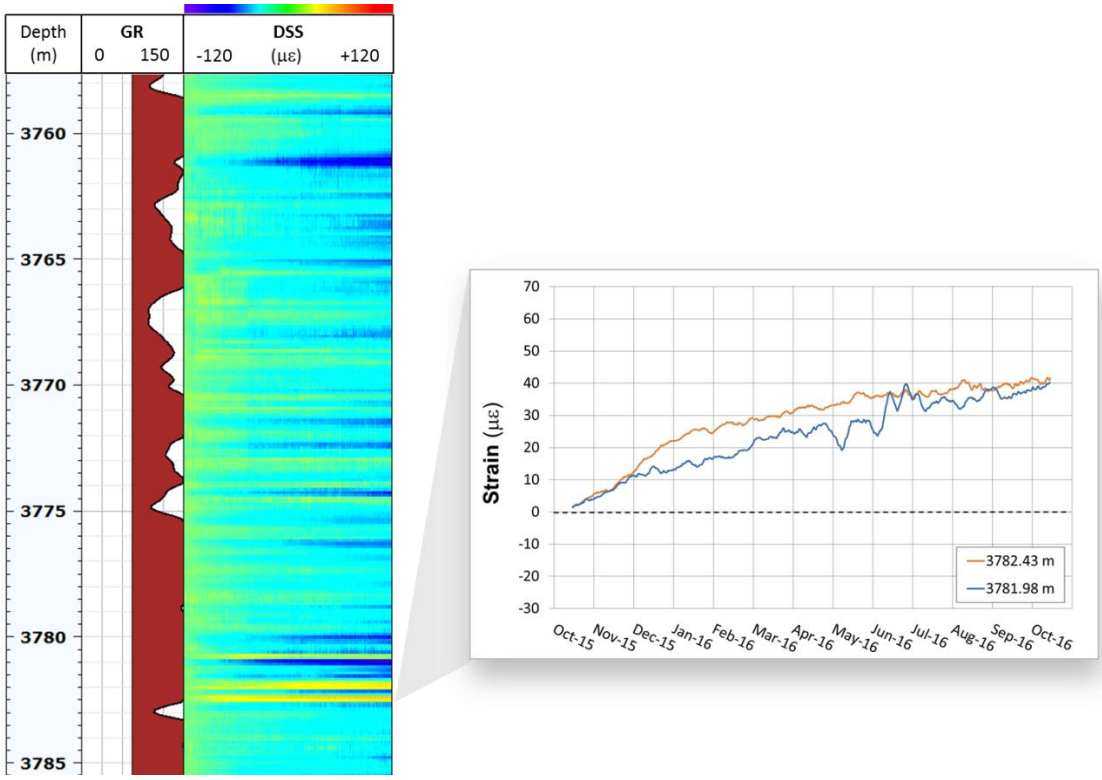

Figure 4.15: **Strain profile over a selected 25 meter interval in the Carboniferous during the first year of monitoring (Oct 12, 2015 – Oct 23, 2016). The inset displays the growing tensile strain at 3781.98 and 3782.43 mAHRT.**

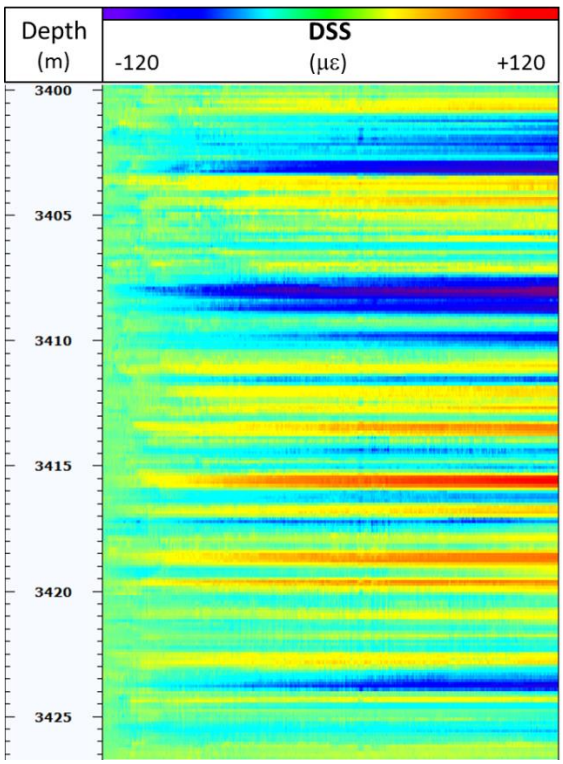

Figure 4.16: Strain profile over the top 25 meters of the DSS cable within the Zechstein Salt during the first year of monitoring (Oct 12, 2015 – Oct 23, 2016).

As another way of visualizing the tensile behavior, Figure 4.17 displays the fraction of the DSS cable under tension within each lithological zone. This is determined by simply dividing the number gratings with $\varepsilon > 0$ by the total number of gratings in each zone. It is important to keep in mind that the data only represent the fraction of the cable experiencing tension, not the magnitude of the tensile signal. For reference, the same strain log acquired at the end of the first year of monitoring displayed in Figure 4.9 is reproduced along with a simplified zonation track for reference. In all zones, the fraction of the cable under tension is initially near 0.5. This is because at the very beginning of monitoring the measured strains were extremely small and within the noise of the measurement (~1 με). Because the noise is random, there is an equal chance of the strain on a given grating to be positive or negative. The fraction of gratings under tension in the reservoir have gradually decreased and by the end of the first year less than 5% of the reservoir was in tension. The behavior within the Carboniferous zone is similar but the decay is much more rapid. In contrast, after an initial decrease over a period of 3 or 4 months, the fractions of the cable under tension within the Salt and the Ten Boer zones are very similar to one another and have remained relatively constant during the year of monitoring, near ~35 – 40%. Note that this fraction is also dependent on the baseline date. If the same analysis is performed starting 5 months later the tensile fractions stabilize near 50% in the Salt (which is not surprising for an interval with no net expansion or compaction) and 40% in the Ten Boer.

Though the source of the tension bands is still not clear, the fact that the tensile signal within the reservoir (both fraction of cable and magnitude of strain) has decreased so notably during the first

year after the well was completed suggests that it is perhaps more likely related to drilling activity than to production activity.

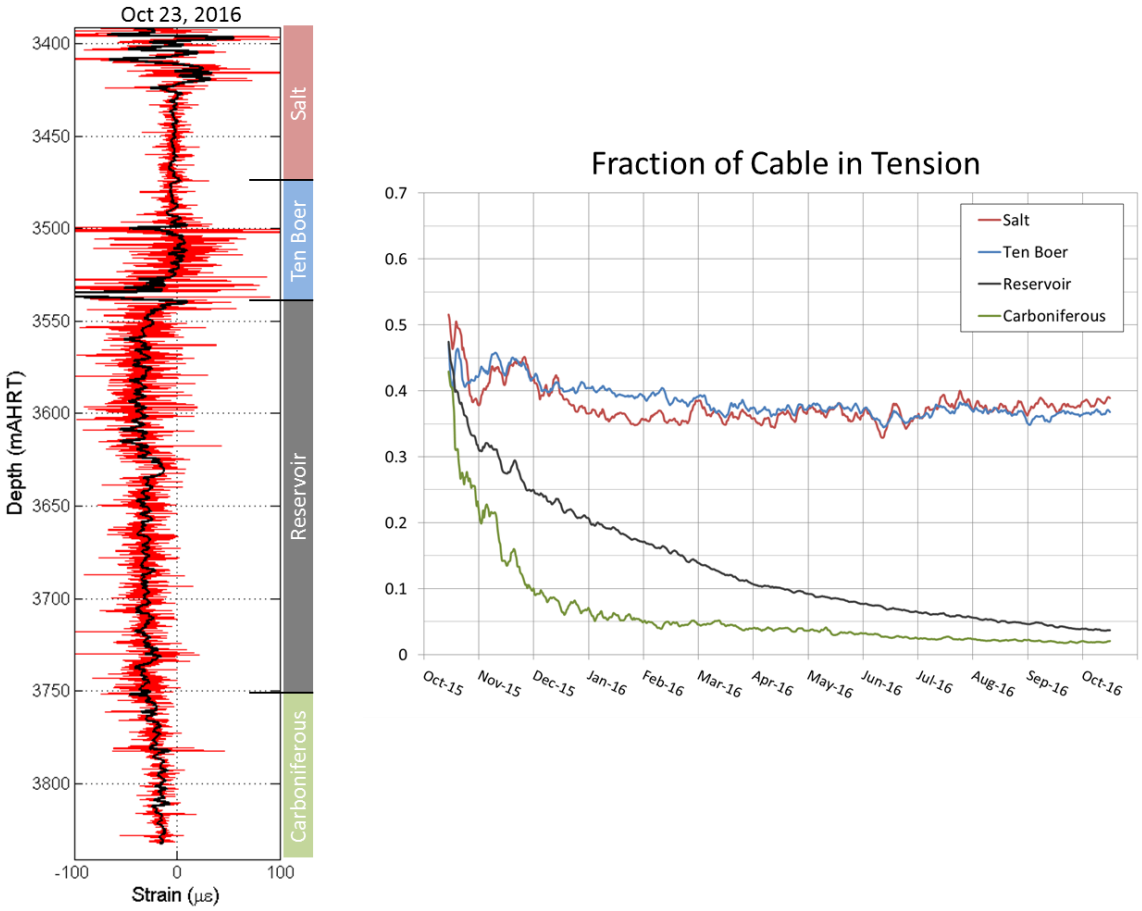

Figure 4.17: **(Left) Strain profile measured at the end of the first year of monitoring, acquired on Oct 23, 2016. The black curve represents a heavily smoothed version of the data to aid in visualization of the average. (Right) Fraction of the cable in tension as a function of time within each major lithological zone (Zechstein Salt, Ten Boer, Reservoir, and Carboniferous).**

4.2.4. Density Log Comparison

In a constitutive sense, the formation strain ε is determined by the product of the bulk compressibility C_m and the change in pressure ΔP:

$$\varepsilon = C_m \cdot \Delta P \tag{2}$$

Therefore, under constant pressure depletion (i.e., constant ΔP) the strain profile should correlate with the formation compressibility along the well. Unfortunately, an in-situ compressibility measurement is not available. However, in some circumstances, changes in the bulk density (and therefore changes in porosity) are expected to correlate with changes in the formation compressibility, especially in the higher quality sands. Figure 4.18 shows the gamma ray and density logs over a 100 meter interval along the upper reservoir. A single DSS measurement (acquired in April 2016) has been overlaid on the density track. The expanded view of the upper ~20 meters (3563 – 3584 mAHRT) shows that there is good correlation between the density log and the strain profile. The sands are fairly clean in this interval and therefore changes in bulk density should correlate reasonably well with changes in formation compressibility. However in the lower highlighted interval (3624 – 3646 mAHRT) the correlation between the strain and density measurements is rather poor. This is due to the higher shale content which, because of the non-uniform lithology, will degrade the correlation between the formation compressibility and the bulk density. Additionally, ΔP will vary with the changes in lithology because the shale layers do not deplete. However, the good correlation between the strain measurement and the density log over the interval where changes in bulk density are expected to be a suitable proxy for changes in formation compressibility give confidence that the strain measurement is providing sensible results.

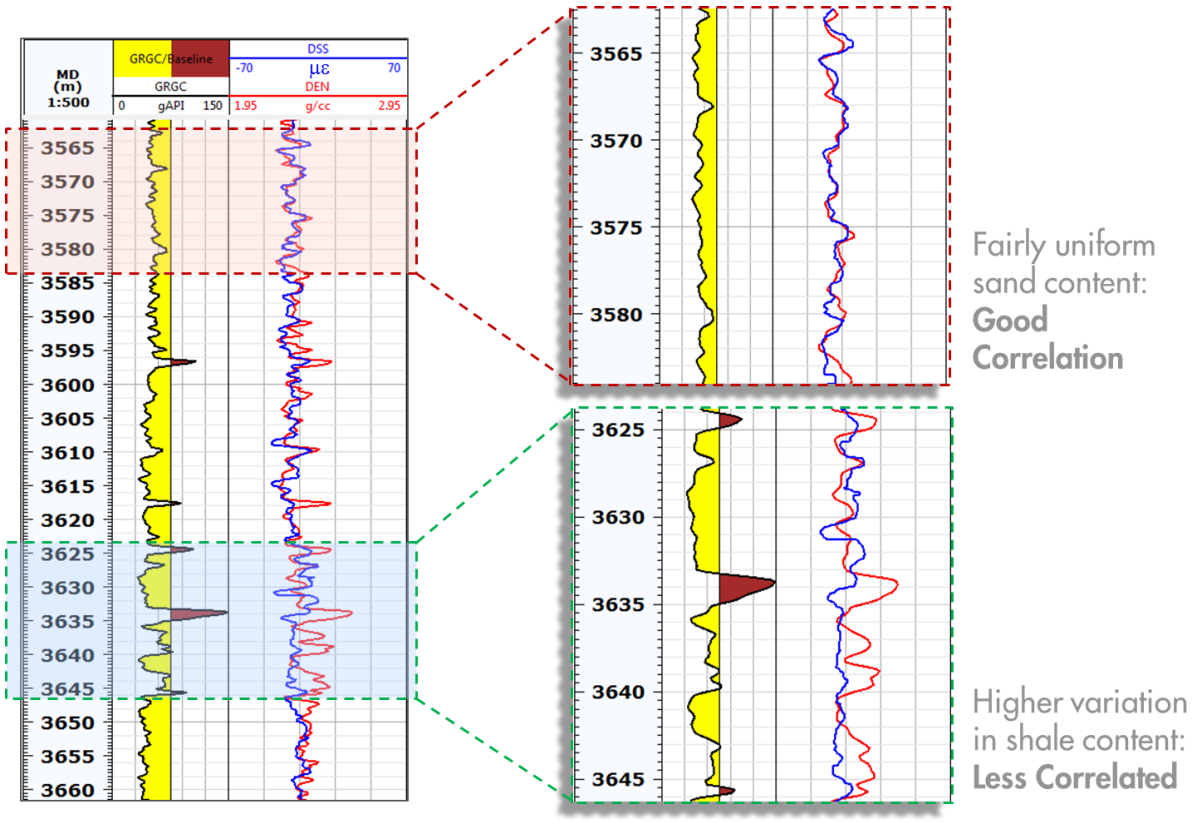

Figure 4.18: **Plot of the gamma ray log, density log, and strain along a ~100 meter interval in the upper part of the reservoir. The two insets on the right display and enlarged view of the shaded areas indicated on the log.**

4.2.5. Image Log Comparison

The fine scale of the strain measurements from DSS allows for a comparison of the strain data to other high resolution well data such as borehole image and core data. A detailed comparison and examination is yet to be performed; however, in some examples one can observe possible correlations between regions of notable strain and other formation properties for various intervals.

Figure 4.19 shows the strain log, borehole image log, and core CT scans over a depth interval spanning the anomaly at the bottom of the Ten Boer discussed in section 4.2.2. The regions of high strain appear to somewhat correlate with variations in resistivity observed in the borehole image log as well as density variations observed in the CT scans of the core.

Similarly, Figure 4.20 shows the same measurements over a 30 meter interval in the upper reservoir. Streaks of higher (apparent) density (white on the CT scans) appear to develop less strain than the adjacent lower density intervals.

The observations shown here merely serve to give an impression of the kind of comparisons that could potentially be made. The study is at this point is not developed far enough that any conclusions can be drawn.

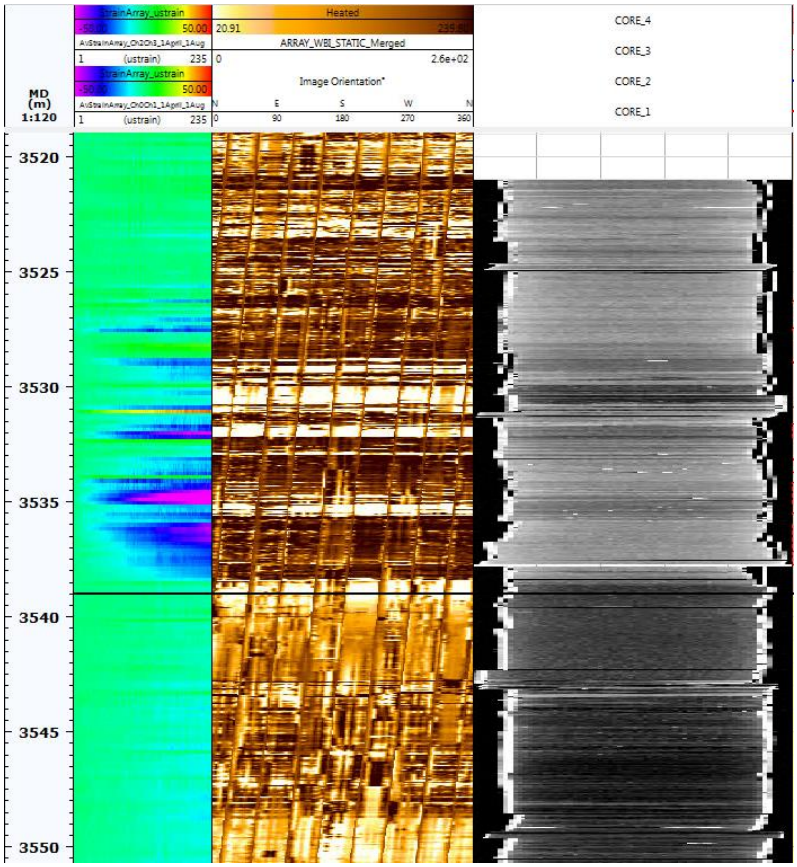

Figure 4.19: **Comparison of the strain data from DSS to the borehole image and core CT scan. The black horizontal line at 3538 mAHRT denotes the top of the reservoir.**

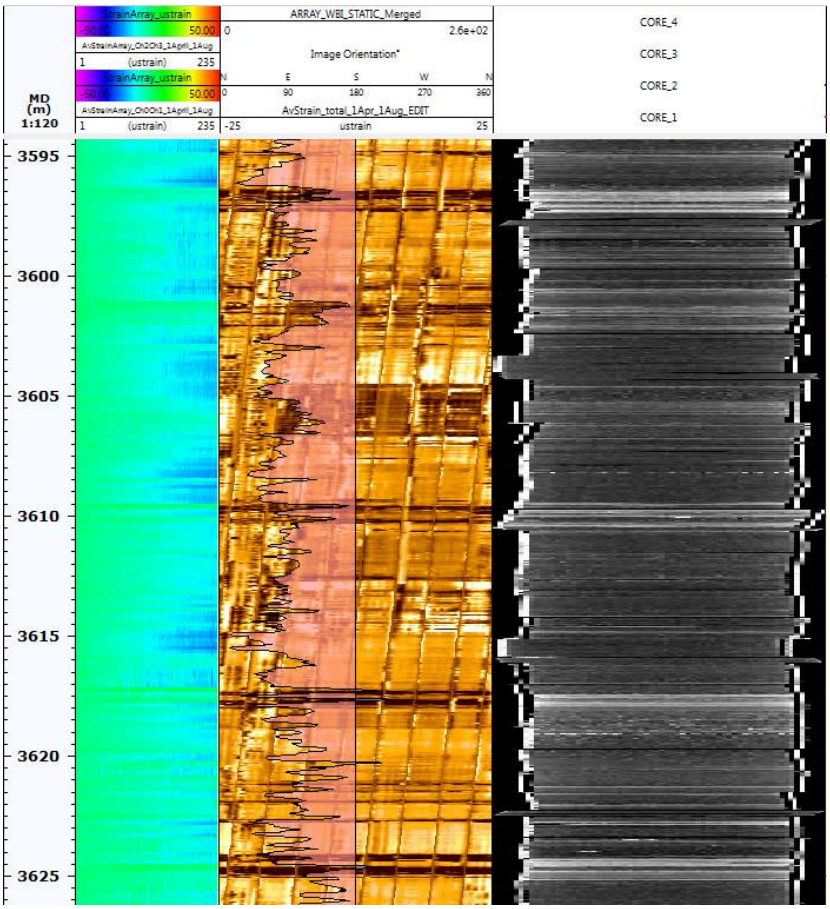

Figure 4.20: Comparison of the strain data from DSS to the borehole image and core CT scan. Streaks of higher (apparent) density (white on the CT scans) appear to develop less strain than the adjacent lower density intervals.

4.3. Compaction Measurements

The data presented in section 4.2 demonstrated how DSS can be used to measure the strain profile along the portion of the well monitored by the system. However, as will be shown in this section, it is also valuable to look the measurement aggregated within specific depth intervals to provide bulk strain behavior corresponding to zones of interest.

4.3.1. Zonal Compaction

As mentioned previously, though bands of tension are observed in many regions of the monitored interval, the general behavior within the Ten Boer and the Reservoir is compaction. Compaction is

also observed within the Salt and Carboniferous zones; however, the DSS cable only extends a limited distance into these formations and therefore does not provide a complete description of the bulk behavior in these zones. Figure 4.21 shows a plot of the compaction within each lithological zone as a function of time during the first year of monitoring. For reference, the figure also includes the strain profile measured at the end of the year (Oct 23, 2016) denoted with a generalized zonation track.

After an initial compaction period, the strain in the overlying Salt stabilized and didn't exhibit any notable subsequent compaction. Because compaction is not expected in the Salt, it is assumed that the small (~ 5 με) compaction signal during the first 3 months of monitoring was due to some form of settling in the formation after being disturbed by the drilling process. One might expect the strain profile in a non-compacting zone to be uniformly near-zero. However, it is interesting to note that this only occurs over the lower portion of the monitored Salt interval. Conversely, as shown earlier in Figure 4.10, the upper portion exhibits relatively large tension and compression bands. Evidently, the two opposing signals exactly compensate for one other producing a net effect of zero compaction.

Initially, the compaction in the Ten Boer was very small and coincided with the initial compaction in the Salt. However, during the dynamic event that began in late November 2015 at the bottom of the Ten Boer (described in section 4.2.2) the compaction rate increased dramatically. Though the affected interval was somewhat limited, the magnitude of the compaction was large enough to significantly impact the average strain of the 63 m interval. Afterwards, the compaction continued but at much reduced rate. Additionally, the compaction rate has subtly decreased throughout the year of monitoring.

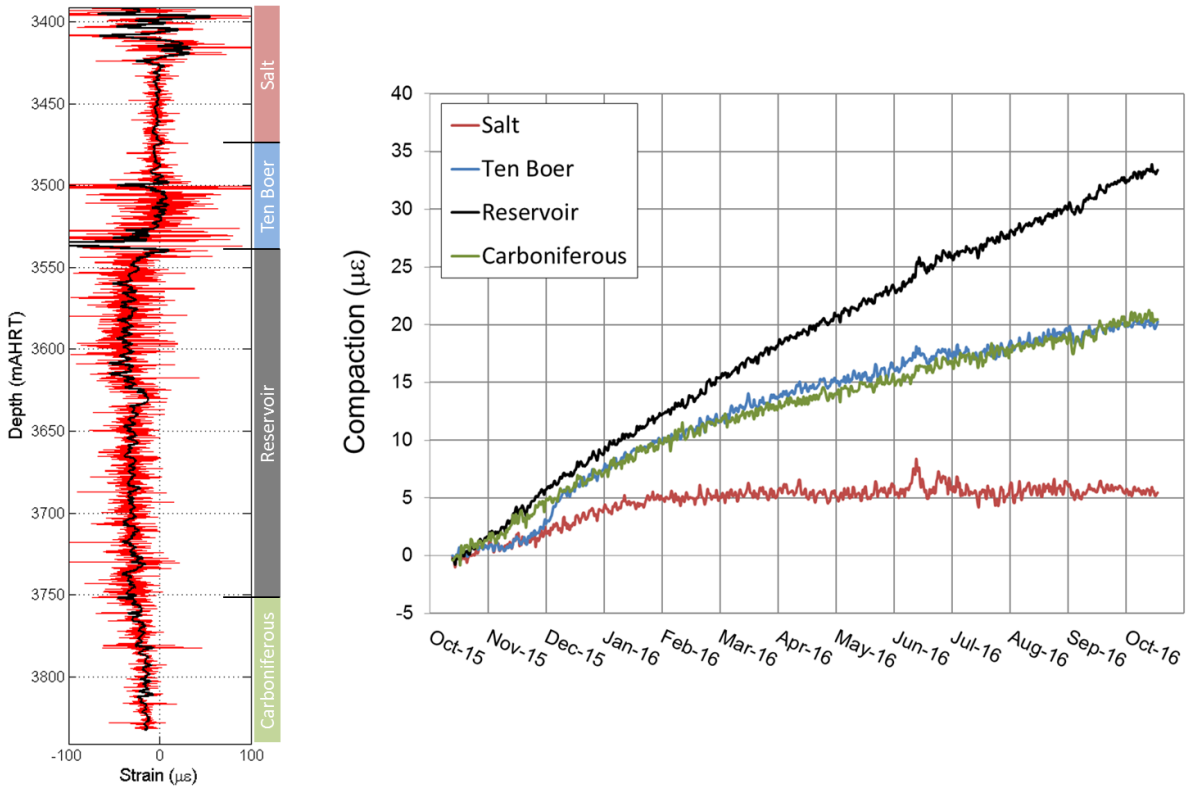

Figure 4.21: **(Left) Strain profile measured at the end of the first year of monitoring, acquired on Oct 23, 2016. The black curve represents a heavily smoothed version of the data to aid in visualization of the average. (Right) Measured compaction within each major lithological zone with DSS coverage (Zechstein Salt, Ten Boer, Reservoir, and Carboniferous).**

The Reservoir was observed to steadily compact and by the end of the first year of monitoring a total strain of 33 με was measured across the 215 meter sandstone interval, corresponding to ~7.1 mm of compaction. Similar to the behavior observed in the Ten Boer, the compaction rate in the reservoir has decreased throughout the year. Figure 4.22 displays the measured compaction rate and the modeled depletion rate at the ZRP-3 well location during the first year of monitoring. The compaction rate was determined from the slope of a linear fit to the compaction data over a moving 90-day interval. The depletion rate was calculated from the average of the depletion rate values in each grid block of the reservoir model (weighted by their heights) intersected by the wellbore. The initial compaction rate of ~45 με/yr decreased to ~25 με/yr by the end of the first year. This trend is reasonably well matched by the modeled depletion rate, suggesting it is related to the declining production rate during the time interval.

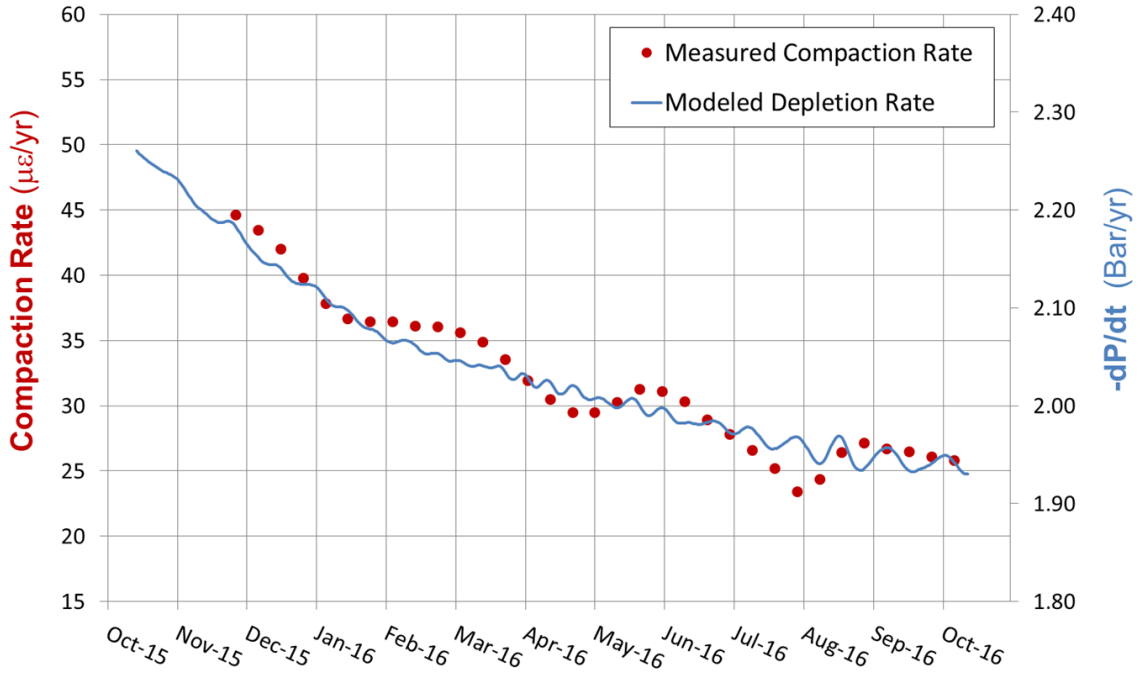

Figure 4.22: Measured compaction rate and modeled depletion rate during the first year of monitoring (Oct 12, 2015 – Oct 23, 2016).

As shown in Figure 4.21, the top of the Carboniferous underburden has exhibited notable compaction during the first year of monitoring. Interestingly, the compaction curve looks remarkably similar to that for the Ten Boer (beginning after the dynamic event in the Ten Boer in late November, 2015). However, because the DSS cable only monitors the upper 79 meters of the underburden and does not span the entire Carboniferous interval it is likely that the similarity in magnitude is coincidental. Indeed, observation of the strain profile at the top of the Carboniferous zone, 3754 to 3833 mAHRT, (shown at the bottom of the left-hand plot of Figure 4.21) reveals that the compaction signal decreases with depth. Presumably, the compaction signal decays to zero further below the DSS cable, though this has not been confirmed. It is also interesting to note that there is no dramatic change or upset in the strain profile at the interface between the Reservoir and the Carboniferous.

4.3.2. Effect of Temperature Correction

To demonstrate the effect of applying the temperature correction to the compaction data using the synthetic temperature curve shown in Figure 4.8, the compaction measurement across the reservoir interval is displayed in Figure 4.23 with and without the correction. The impact that thermal changes have on the DSS measurement depends on the relative sizes of the temperature change and the mechanical strain. Though the aggregate reservoir strains measured in the ZRP-3 well are relatively small (0 – 30 με), the change in temperature in the reservoir during the year was also small, < 0.5°C. Consequently, the difference between the corrected and uncorrected compaction curves is

less than 10%. Therefore, the analysis and interpretation of the compaction behavior is relatively unaffected by the uncertainty in the temperature data.

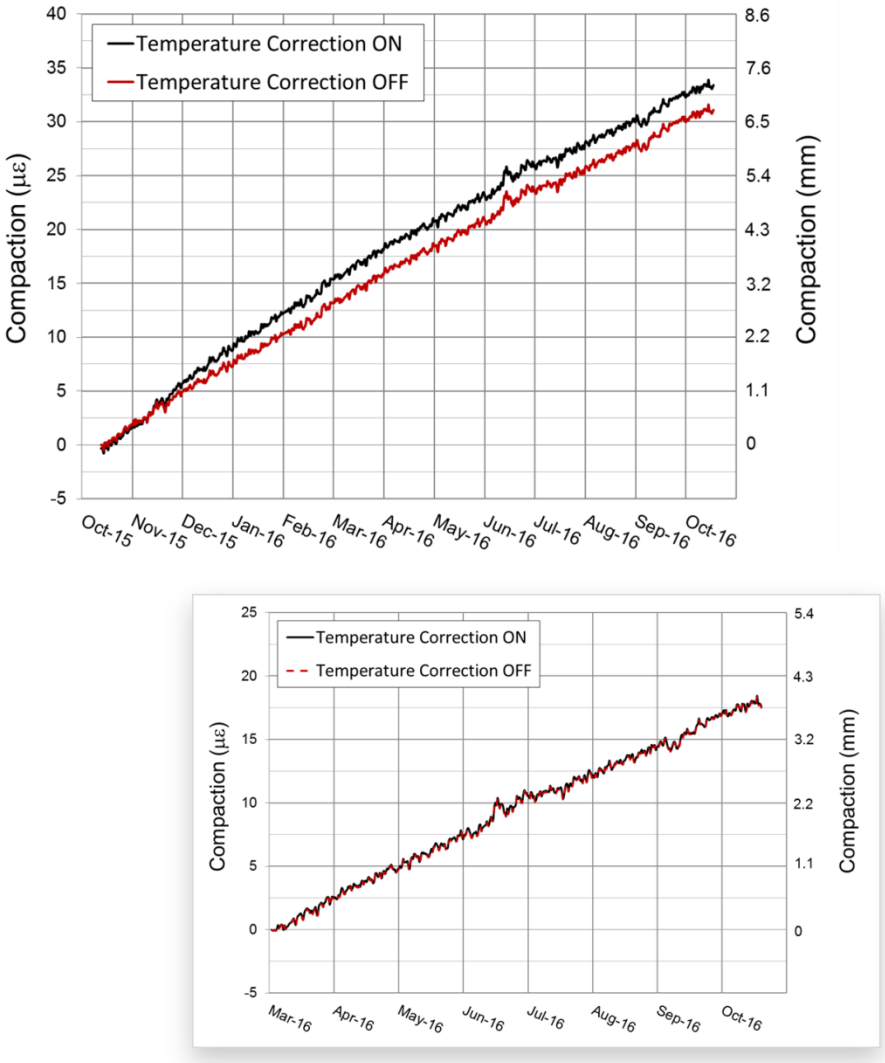

Figure 4.23: Comparison of the compaction measurement across the reservoir interval with and without the temperature correction applied. In the top plot the data have been baselined on Oct 12, 2015, whereas in the inset at the bottom the data have been baselined on Mar 1, 2016.

Because the temperature (presumably) did not change appreciably after the first 5 months of monitoring, the compaction data are unchanged by the application of the temperature correction when baselined after March 2016. This is shown in the inset of Figure 4.23 which displays the compaction across the reservoir relative to the measurement on Mar 1, 2016 with and without the temperature correction. The two curves are the identical from Mar 1, 2016 – Oct 23, 2016 because the temperature did not change during that time period.

Therefore, it is sometimes useful to simplify the analysis by only looking at the data since March 2016 because the impact on the measurement from post-drilling thermal and 'settling' effects is reduced. Figure 4.24 shows the measured compaction within each lithological zone baselined on Mar 1, 2016. The compaction rates based on the most recent 90 days are displayed next to each curve. Because the measurement is extremely sensitive, it is still possible that even over this time interval the data are influenced by lingering effects from the drilling process. However, the data are probably more indicative of the 'true' formation behavior than the data during the first several months.

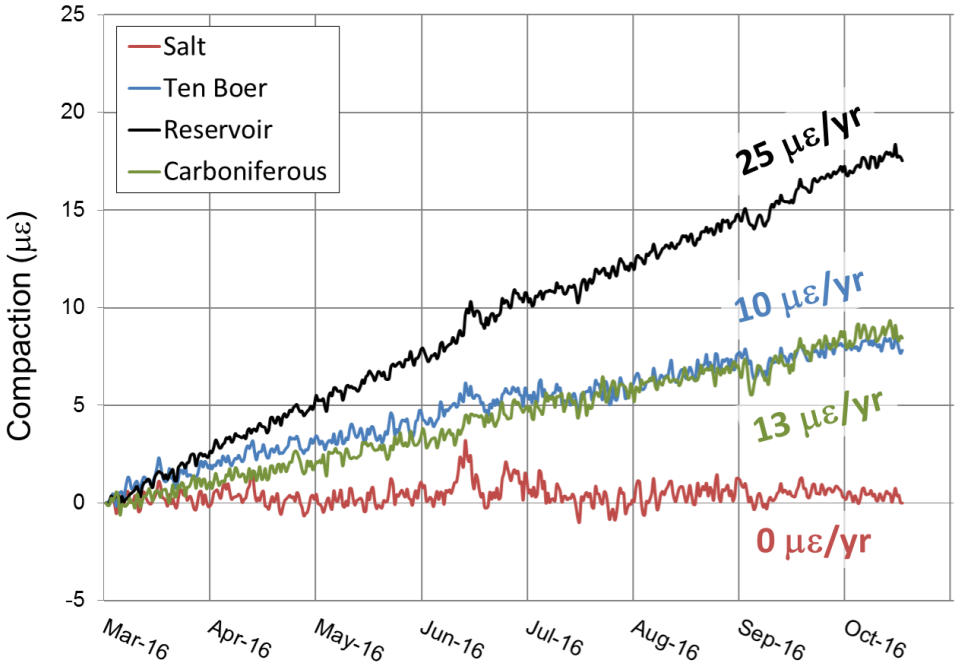

Figure 4.24: Measured compaction within each of the major lithological zones baselined on Mar 1, 2016.

4.3.3. Comparison to Compaction Data in the Stedum Well

In an effort to validate the reservoir compaction measurement in the Zeerijp-3 well, the data have been compared with the compaction data from the nearby Stedum well obtained with radioactive markers. Though the compaction across the reservoir might not be identical at the two well locations, they are both near the center of the subsidence bowl and (as shown in Figure 1.7) are within ~5 km of each other. Therefore, any differences in compaction at the two locations are likely minimal. Figure 4.25 shows the strain measurements acquired in the Stedum well since 1984. The magnitude of the strain has increased in a generally linear fashion; however, there is a significant degree of scatter in the data. Though the variation in the data is dominated by the uncertainty in the measurement and subsequent analysis, there is likely some legitimate variation due to actual changes in the compaction rate as a result of changes in the production rate. Therefore, a linear

extrapolation of the rates obtained during the past year might not perfectly match the rates from the previously acquired data. Nonetheless, the range of compaction rates obtained from the DSS data in the ZRP-3 well (indicated by the shaded region on the plot bounded by the dashed lines) appear to fit the Stedum data reasonably well. This gives an added measure of confidence that the compaction measurement obtained from the DSS system is quantitatively reasonable.

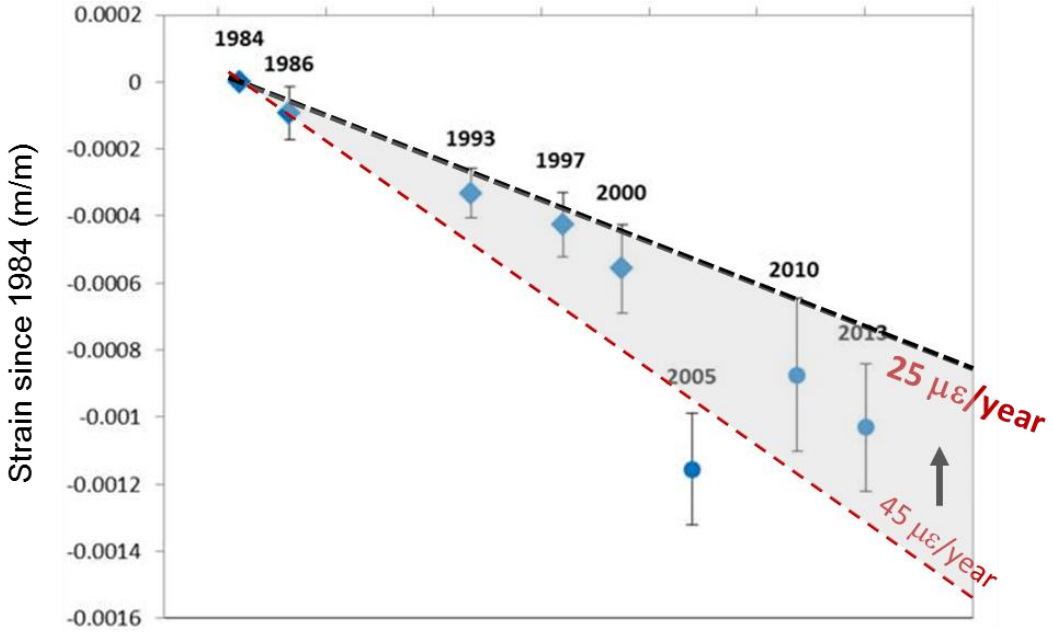

Figure 4.25: Compaction measured in the nearby Stedum well since 1984 using radioactive markers [15]. The dashed lines represent the initial and final compaction rates of 45 and 25 με/yr, respectively, measured in ZRP-3 with the DSS system.

It is also worth noting that it was deemed not useful to collect compaction data from the radioactive markers more frequently than once every 5 years or so, simply because the expected compaction occurring over shorter time periods would be too small for the method to detect. Therefore, getting a good compaction trend can take decades. However, by using the DSS system the compaction rate can be determined almost in real-time.

4.3.4. Comparison to GPS Data

In addition to the existing compaction monitoring wells outfitted with radioactive markers, the reservoir compaction in the Groningen field is also inferred from geomechanical models calibrated to surface subsidence measurements. Fortunately, there is a surface GPS station located at the ZRP-3 well site which provides an ideal opportunity to compare the surface subsidence to the reservoir compaction. Figure 4.26 displays the compaction across the reservoir as well as across the entire 450 m interval monitored by the DSS cable (in absolute length change, mm) during the first

year of monitoring. In addition, the figure also includes the subsidence measured by the GPS station during the same time interval (Oct 12, 2015 – Oct 23, 2016). Note that, in contrast to the compaction data obtained from the radioactive markers, measurements from the GPS are available at a similar temporal resolution to the DSS system. It is observed that the total compaction measured across the cable is ~50% greater than the measured surface subsidence.

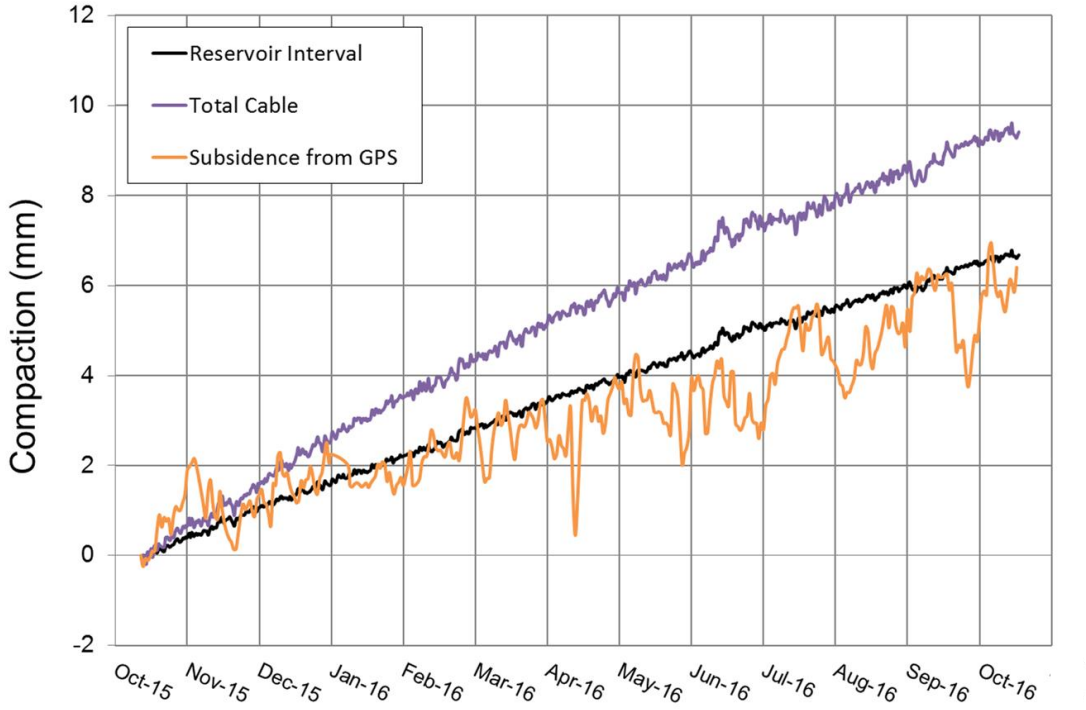

Figure 4.26: Comparison of the surface subsidence measured by the GPS station at the well site (orange) to the subsurface compaction measured by the DSS system across the entire 450 meter cable (purple) and across the reservoir interval (black) from Oct 12, 2015 to Oct 23, 2016.

4.3.5. Compressibility

As discussed in section 4.2.4, strain is the product of the formation compressibility and the change in pressure. In that section, the correlation between strain and compressibility was presented under the assumptions that in clean sands of uniform lithology: (1) changes in compressibility are correlated with changes density and (2) the pressure depletion at each depth within the uniform interval is the same. This was done to draw correlations between the strain and (unavailable) compressibility profiles. However, when attempting to *determine* the compressibility one needs to measure both the strain and the pressure change. Unfortunately, measurements of the pressure

change over the reservoir interval are not available. However, depletion values can be estimated using the calibrated (history-matched) reservoir model.

Figure 4.27 shows the measured compaction across the reservoir plotted against the modeled pressure depletion at the ZRP-3 well location. The plot is quite linear and the compressibility is provided by the resulting slope:

$$C_m = 1.4 \ [10^{-5} Bar^{-1}]$$
$$(= 0.96 \ \mu\varepsilon/psi)$$

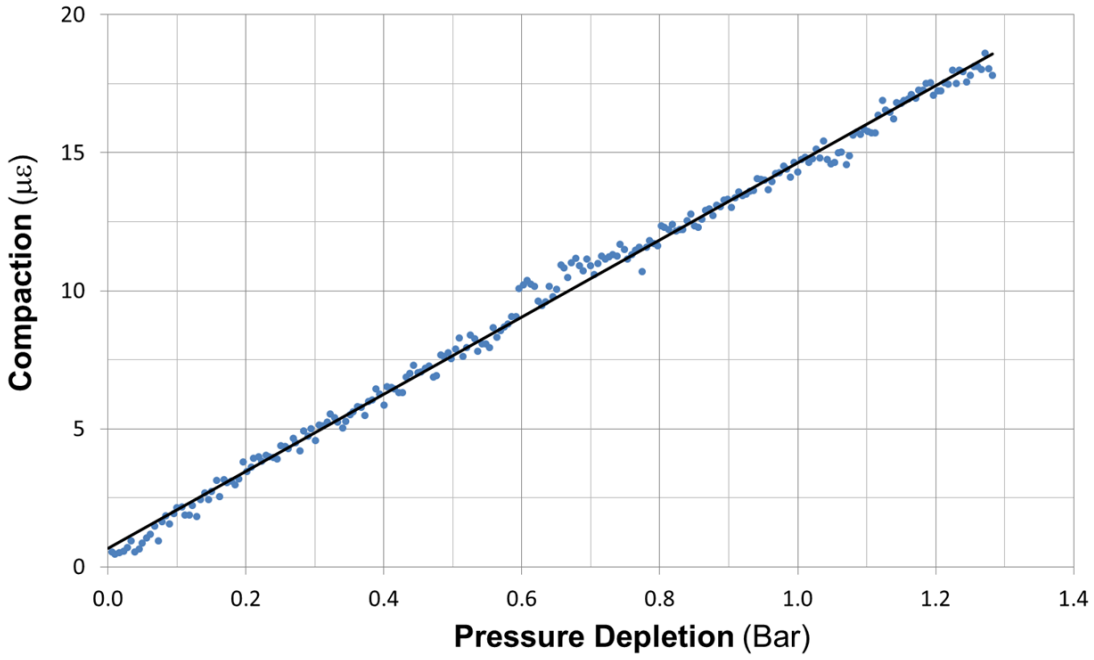

Figure 4.27: Measured compaction plotted against modeled pressure depletion from Mar 1, 2016 – Oct 23, 2016. The black line represents a linear fit to the data.

This, of course, is an aggregate compressibility across the entire reservoir interval. However the same methodology can be applied to each individual grid block of the reservoir model that intersects the well trajectory. Figure 4.28 shows the strain and porosity logs across the reservoir as well as the average values within each of the 31 grid blocks.

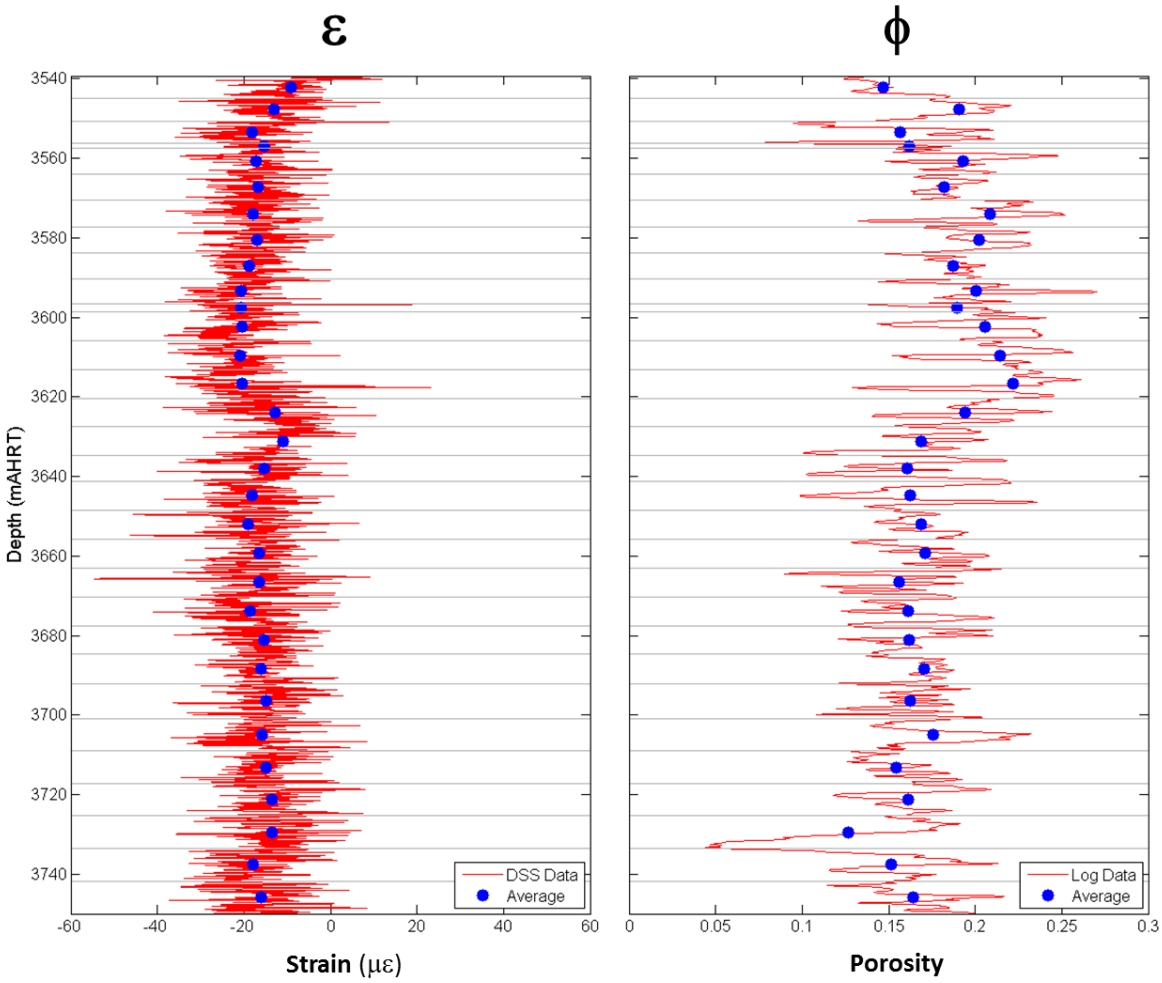

Figure 4.28: **Strain (left) and porosity (right) measured across the reservoir. The blue data points represent the average values within each grid block of the reservoir model along the well trajectory (denoted by the horizontal grey lines).**

The average strain values in each grid block are displayed as a function of time in the top plot of Figure 4.29. This plot effectively represents an upscaled version of the reservoir interval of the strain colormap in Figure 4.9. Interestingly, when the strain data are upscaled to the grid block level (each block has a nominal height of ~7 m) there is no evidence of the tension bands discussed in section 4.2.3; i.e., the average strain within each grid block is entirely compressive. Therefore, other in-well compaction monitoring technologies that don't have sub-meter spatial resolution (such as the radioactive markers) are not able to measure the tension signal.

The bottom plot in Figure 4.29 shows the pressure depletion in each grid block of the reservoir model as a function of time. It is clear that there is little variation in the vertical (depth) profile of the depletion within the reservoir.

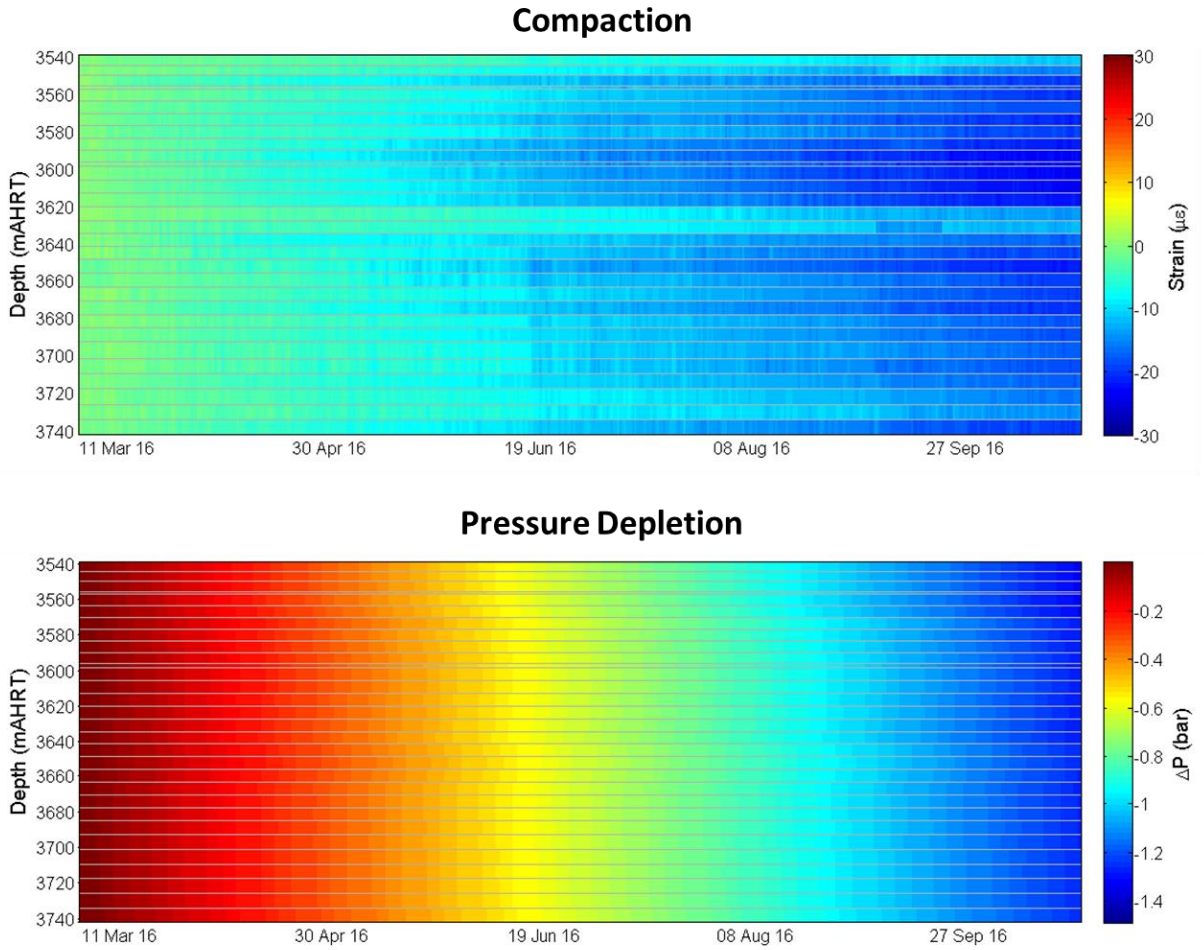

Figure 4.29: Time evolution of the compaction (top) and pressure depletion (bottom) within each grid block of the reservoir model from Mar 1, 2016 to Oct 23, 2016. The depths of the grid block boundaries are indicated by the grey lines.

The compaction vs. depletion plots for 9 representative grid blocks in the reservoir are shown in Figure 4.30 (the plots for the other 22 grid blocks in the reservoir are similar). As observed in the plot of the aggregate reservoir compaction in Figure 4.27, the trends are reasonably linear and the compressibility values derived from the slopes are displayed in the title of each plot.

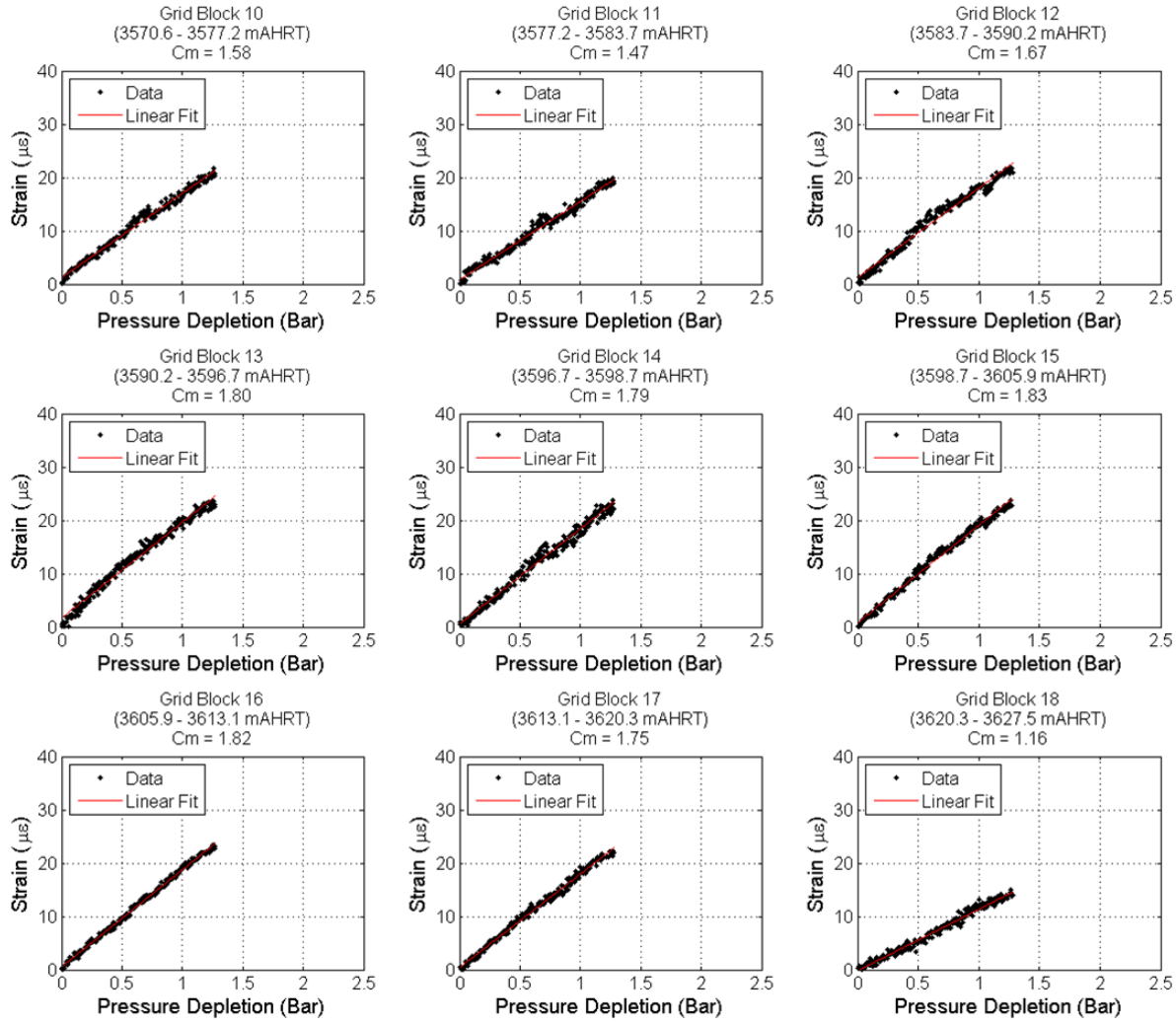

Figure 4.30: Measured compaction plotted against modeled pressure depletion in selected grid blocks of the reservoir model from Mar 1, 2016 – Oct 23, 2016.

Figure 4.31 shows the compressibility plotted against the porosity in each of the 31 grid blocks of the reservoir model. The data points are colored according to depth (taken at the center of each grid block) and there appears to be a general trend of decreasing compressibility and porosity with increasing depth.

Though there is naturally some degree of uncertainty in the strain measurement, most of the uncertainty in the derived compressibility values actually comes from the modeled pressure depletion. The greatest source of uncertainty in the model pertains to the amount of gas dissolved in the aquifer. The gas-water contact is located at 3571 mAHRT, therefore approximately 85% of the reservoir interval in ZRP-3 is in the aquifer. Consequently, changes in the pressure behavior in the water leg can have a notable impact on the compressibility values.

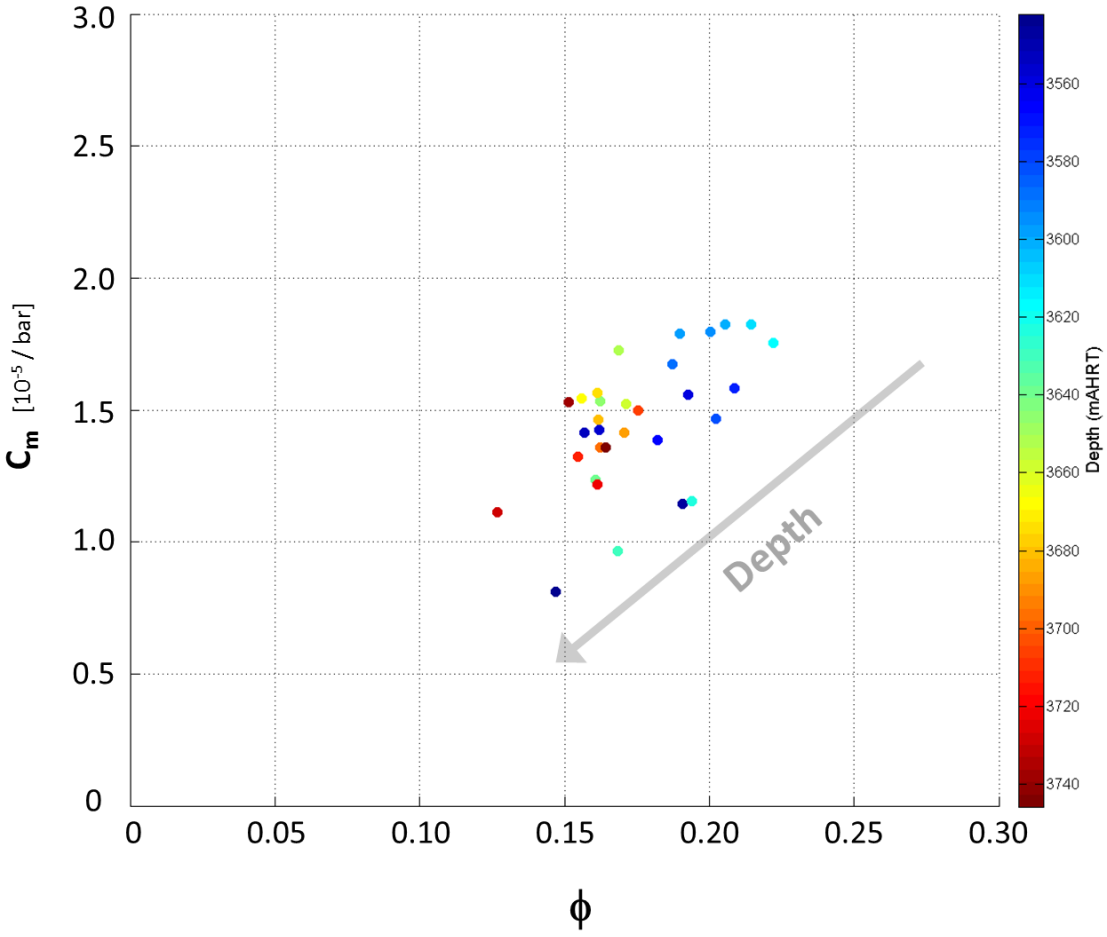

Figure 4.31: **In situ compressibility as a function of porosity based on DSS compaction measurements, modeled pressure depletion, and wireline porosity log data. The data points have been colored by depth and the trend is indicated with the large grey arrow.**

To explore the effect of varying the dissolved gas content, the compressibility was determined using depletion values obtained from three modeled scenarios: (1) no dissolved gas in the aquifer (which is the base case typically used in the reservoir model by the asset), (2) 10%, and (3) 20% dissolved gas. The data points in Figure 4.32 represent the results of the base case and the limits of the error bars are determined by the range of values obtained from the other scenarios. For comparison, the figure also shows the compressibility results obtained from two other sources. The red curve is a polynomial fit to the values obtained from laboratory measurements of core samples from several wells across the Groningen field. The black line is a fit to the compressibility values obtained from an inversion model using surface subsidence data (from leveling survey measurements) combined with modeled reservoir pressures.

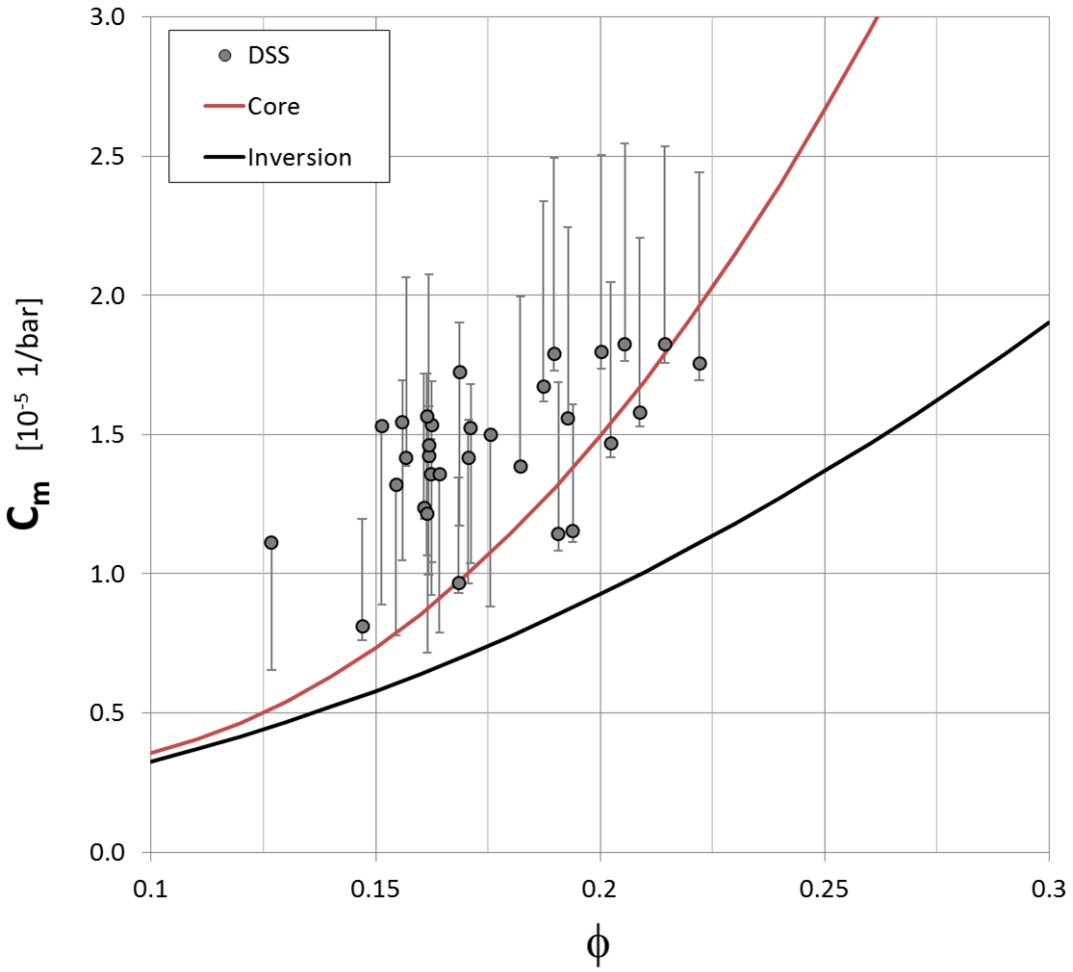

Figure 4.32: Comparison of the various compressibility results based on the DSS data (circles), core data (red line), inversion from surface subsidence (black line).

The compressibilities acquired from the core measurements are consistently higher than those obtained from modeling efforts. This has caused many people to speculate that deficiencies in the ability of the laboratory experiments to adequately represent reservoir conditions caused the results to be upwardly biased. Therefore, a scaling constant (usually on the order of ~0.5 – 0.6) has been often applied to the core data to bring them into better alignment with the model results.

It is interesting to note that, like the core data, the compressibility values derived from the in situ strain measurements are also notably higher than those obtained from the inversion model. The observation that both (independent) experimental data sets show higher compressibilities might suggest that the assumptions within the inversion model should be reassessed. However, it is also possible that the modeled pressures used to convert the strain measurements to compressibilities have more uncertainty or bias than implied by the current error bars. If this is the case, and the compressibility values from the inversion model are taken to be accurate, then the strain

measurements might be used to constrain the pressures in the reservoir model at the ZRP-3 well location. It should also be noted that the DSS-derived compressibility values are based on data obtained after a pressure depletion of only 1-2 bar with high relative uncertainty. This depletion is much lower than any typical lab measurement; however, the continued compaction monitoring with ongoing depletion is expected to significantly reduce the uncertainty over time.

It is important to point out that each curve in Figure 4.32 represents a fit to a distribution of data acquired (or modeled) over a large area. In contrast, the DSS data are sampled at a single well in the field. A data point randomly sampled from a distribution is unlikely to match the mean value. However, the range and distribution of compressibilities and porosities in the ZRP-3 are most likely similar to those across the field. In that sense it is reasonable to compare the distribution of values from the DSS data to the means of the distributions of the field-scale data.

Questions have arisen regarding the possible stress disturbance due to the drilling process and the geomechanical effect exerted around the borehole by the stiffness of a well casing [24]. This would alter the local vertical formation compressibility, and thus influence how representative wellbore compaction measurements (of any form) are of the actual reservoir compaction. In response to this, Ferronato et. al. [25] conducted a numerical modeling study for the Northern Adriatic gas fields in which they found that the casing stiffness only marginally affects compaction measurements from radioactive markers. In the most unfavorable conditions (i.e., shallow depths) the compaction was underestimated by approximately 10%. However, at a depth of 3000 m the discrepancy was only 2%. Furthermore, the potential casing influence acts to decrease the local compressibility. Any attempt to correct for this effect would increase the discrepancy between the DSS-derived compressibilities and those from the inversion modeling.

5. Summary

This report provided an overview of Fiber Bragg Grating-based DSS technology and the installation of Baker Hughes' SureVIEW WIRE™ system in the Zeerijp-3 monitor well in the Groningen gas field. Observations from the DTS and DSS data during the first year of permanent monitoring (Oct 12, 2015 – Oct 23, 2016) have been presented along with preliminary analysis of the results. Because the DSS technology is new, many questions regarding the interpretation of the data remain and further analysis is ongoing.

The DTS data revealed that the rethermalization process following the drilling activities lasted for more than 6 months. In addition, after installation of the geophone string in Nov 2015, a localized heating of ~2-3°C was clearly identified at each of the geophone depths. However, the geophones failed in February 2016 and the temperature across the reservoir has been largely stable since March 2016. After the first ~4-5 months of monitoring, the stability of the DTS measurement has suffered due to changes in temperature of the interrogator (in part impacted by activity in the data cabin dealing with the failed geophones). However, a synthetic temperature curve has been generated for each of the lithological zones that is suitable for temperature correction of the aggregate compaction data. Though improvements in the DTS measurement are desirable, the deficiencies have had little impact on the observations and conclusions derived from the strain data.

The DSS measurements have revealed that the strain profile in the subsurface is quite inhomogeneous. The variation in the strain profile is observed to strongly correlate with the density log over intervals of clean sandstones. However, in shaley regions (where the lithology is more varied) the correlation breaks down because variations in density are no longer a suitable proxy for changes in compressibility. In addition, abrupt changes in the strain profile are observed to typically occur at lithological boundaries. The observed correlation between the strain measurement and the lithology gives confidence that the measured signal is representative of the actual formation strain.

Bands of tension (a few 10s of cm thick) are observed in nearly all lithologies spanned by the DSS cable. The mechanism(s) driving this tension signal is not understood. Though the behavior of individual bands varies, it is observed that the fraction of the cable experiencing tension has been steadily decreasing in the Reservoir and underlying Carboniferous. However, the fractions in the Salt and Ten Boer have remained relatively constant through the year.

Despite the inhomogeneity and the bands of tension in the strain profile, the net effect is a growing compaction signal in the reservoir. The rate of compaction has decreased from ~45 to 25 με/yr and correlates reasonably well with the modeled reduction in reservoir pressure at the ZRP-3 well location. This suggests that the reduction in compaction rate is related to field production. In addition, the range of compaction rates measured in the ZRP-3 well using the DSS system are similar to those measured in the (nearby) Stedum well using radioactive markers. Again, this gives added confidence that the strain measurement is quantitatively reasonable. Additionally, the compaction data is obtained in real-time; whereas results from the radioactive markers are acquired a couple of times each decade.

A growing compaction signal is also observed across the Ten Boer Claystone as well as the upper portion of the Carboniferous (only 79 meters of the underburden are monitored by the DSS system). After an initial settling period of ~3 months, no further compaction in the overlying Zechstein Salt has been observed. The surface subsidence measured by the GPS located at the well

site is less than the compaction measured across the (total) DSS cable. This observation suggests a notable tension signal in the overburden above the monitored interval.

The measured strain across the reservoir interval was used in conjunction with formation pressures obtained from the reservoir model to determine the compressibility as a function of porosity. The preliminary resulting values are similar to those obtained from laboratory core measurements, but larger than those derived from modeling and inversion efforts.

6. Acknowledgements

The authors wish to acknowledge the support and sponsorship from the operating company, Nederlandse Aardolie Maatschappij B.V. They also wish to thank Per Valvatne (NAM) for his input and for providing valuable reservoir model pressure data.

References

[1] J.V. Koelman, "Fiber-Optic Sensing Technology Providing Well, Reservoir Information – Anyplace, Anytime", Journal of Petroleum Technology, Vol. 63, No. 7, p. 22 (2011).

[2] M. Rahman, P.J. Zannitto, D.A. Reed, M.E. Allan, "Application of Fiber-Optic Distributed Temperature Sensing Technology for Monitoring Injection Profile in Belridge Field, Diatomite Reservoir", SPE 144116, SPE Digital Energy Conference and Exhibition, The Woodlands, TX (2011).

[3] M. Rahman, D.A. Reed, M.E. Allan, "The Challenges of Full Field Implementation of Fiber-Optic DTS for Monitoring Injection Profile in Belridge Field, California", SPE 163694, SPE Digital Energy Conference and Exhibition, The Woodlands, TX (2013).

[4] J. van der Horst, H. den Boer, P. in 't Panhuis, R. Kusters, D. Roy, A. Ridge, A. Godfrey, "Fiber Optic Sensing for Improved Wellbore Surveillance", Paper IPTC 16873 presented at the International Petroleum Technology Conference, Beijing, China, March 26-28 (2013).

[5] J. van der Horst, H. den Boer, P. in 't Panhuis, B. Wyker, R. Kusters, D. Mustafina, L. Groen, N. Bulushi, R. Mijeni, K. Awan, S. Rajhi, M. Molenaar, A. Reynolds, R. Paleja, D. Randell, R. Bartlett, K. Green, "Fiber Optic Sensing for Improved Wellbore Production Surveillance", Paper IPTC 17528 presented at the International Petroleum Technology Conference, Doho, Qatar, January 20-22 (2014).

[6] J. Richards, R. Bartlett, D. Onen, G. Crowther, M. Molenaar, A. Reynolds, B. Wyker, H. den Boer, W. Berlang, "Cloud-based solutions for permanent fiber-optic DAS flow monitoring", Paper SPE-173440, presented at SPE Digital Energy Conference and Exhibition, The Woodlands, Texas, March 3-5 (2015).

[7] D.A. Mustafina, J.J. Kreeft, D.I.M. ten Bosch, "Flow and Low Induced Noise Modeling for Marmul Water/Polymer Injectors for the Development of DAS Interpretation Workflows, SR.16.12700 (2016).

[8] C. Staveley, "Real Time Monitoring System for Oil Rim and Offtake Management of Fractured Carbonate Reservoirs", SPE-181464-MS , Presented at the SPE Annual Technical Conference and Exhibition, Dubai, UAE, Sept 26-28 (2016).

[9] M. Haugland, M. Cannon, J. van der Horst, H. Potters, M. Rahman, J. Ozcan, A. Urdaneta, "Subsurface Distributed Strain Sensing in the Belridge Field Diatomite Reservoir", SR.16.10124 (2016).

[10] J. van der Horst, F. Rambow, G. Frisch, J. Quirein, P. Fox, "Formation Compaction Surveillance in Deepwater Gulf of Mexico: Applications, Experiences, and Best Practices", SPWLA 46th Annual Logging Symposium, paper RRR, June 26-29 (2005).

[11] J. Weiland, D. Mikulencak, P. Fox, G. Frisch, M. Azari, "Waterflood Surveillance in the Mars Field Deepwater GOM: Mississippi Canyon Block 807", SPE 115365, SPE ATCE, Denver, CO (2008).

[12] O. Torsaeter, "An Experimental Study of Water Imbibition in Chalk from the Ekofisk Field", Presented at the SPE Enhanced Oil Recovery Symposium, Tulsa, Oklahoma, SPE-12688-MS, April 15-18 (1984).

[13] M. Raum, R. Duncan, K. Holmes, "Strain Monitoring of a Steamed Reservoir", Presented at the SPE Distributed Fiber-Optics Sensing for Well, Reservoir and Facilities Management Workshop, Napa, California, USA, August 11-13 (2015).

[14] K.V.T Grattan, B.T. Meggitt, "Optical Fiber Sensor Technology", Kluwier Academic Publishers, p. 79-187 (2000).

[15] "Subsidence by Gas Extraction – NAM Gas Fields in Groningen, Friesland and Northern Drenthe", Status Report 2015 and Forecast to the Year 2080, December (2015).

[16] B. Childers, M. Froggatt, S. Allison, T. Moore, D. Hare, C. Batten, D. Jegley, "Use of 3000 Bragg Grating Strain Sensors Distributed on Four 8-m Optical Fibers During Static Load Tests of a Composite Structure", Proc. SPIE 4332, Smart Structures and Materials 2001: Industrial and Commercial Applications of Smart Structures Technologies, 133, June 14 (2001).

[17] B. Soller, D. Gifford, M. Wolfe, M. Froggatt, "High Resolution Optical Frequency Domain Reflectometry for Characterization of Components and Assemblies", Optics Express, Vol. 13, No. 2, p. 666, Jan 24 (2005).

[18] D.G. Davis and S.K. Sanyal, "Case history report on East Mesa and Cerro Prieto geothermal fields", Los Alamos Scientific Lab (1979) (Report LA-7889-MS).

[19] J.M. Gorman, J.P. Abraham and E.M. Sparrow, "A novel, comprehensive numerical simulation for predicting temperatures within boreholes and the adjoining rock bed", Geothermics, 50 (2014) 213-219.

[20] E.C. Bullard, "The time necessary for a bore hole to attain temperature equilibrium", Geophys. J. Int., 5 (1947) 127-130.

[21] S. Fomin, V. Chugunov, and T. Hashida, "Analytical modeling of the formation temperature stabilization during the borehole shut-in period", Geophys. J. Int., 155 (2003) 469-478.

[22] M. Zare-Reisabadi, M.R. Kamali, M. Mohammadnia, and F. Shabani, "Estimation of true formation temperature from well logs for basin modeling in Persian Gulf", J. Petroleum Science and Engineering, 125 (2015) 13-22.

[23] P. Macini, E. Mesini, V.A. Salomoni, and B.A. Schrefler, "Casing influence while measuring in situ reservoir compaction", J. Petroleum Science and Engineering, 50 (2006) 40–54.

[24] M. Ferronato, "Rock Expansion and Compaction at the Marker Scale in Gas Producing Reservoirs", Ph.D. Thesis, TU Delft (2003).

[25] M. Ferronato, G. Gambolati, P, Teatini, and C. Janna, "Casing Influence in Reservoir Compaction Measurement by Radioactive Markers in the Northern Adriatic, Italy", Int. J. Geomechanics, 7 (2007) 444-447.

[26] G. Hool, et. al., "Concrete Engineer's Handbook: Data for the Design and Construction of Plain and Reinforced Concrete Structures", McGraw-Hill Book Company, Inc., New York, Ch. 6 (1918).

[27] F. Rambow, C. Tixier, L. Stockwell, M. Meyers, K. Cowan, "Reservoir Compaction and Seafloor Subsidence in the Gulf of Mexico: A Supplement to the 1994 Design Recommendations and Guidelines for Oil and Gas Developments", EP-2005-3016 (2007).

Appendix 1. Cement Adhesion to DSS Cable

There are many layers of differing materials between the core of the optical fiber and the formation, and there must be good bonding at each interface to properly measure the formation strain. Extensive laboratory testing of the SureVIEW WIRE at Shell Technology Center Houston (STCH) has demonstrated that all of the materials internal to the composite cable structure are satisfactorily bonded (i.e.; strains imposed on the outer surface of the cable couple to the core of the optical fiber extremely well). However, the adequacy of the coupling at the cement-formation and the cement-cable interfaces (see Figure A1.1) are more difficult to directly confirm.

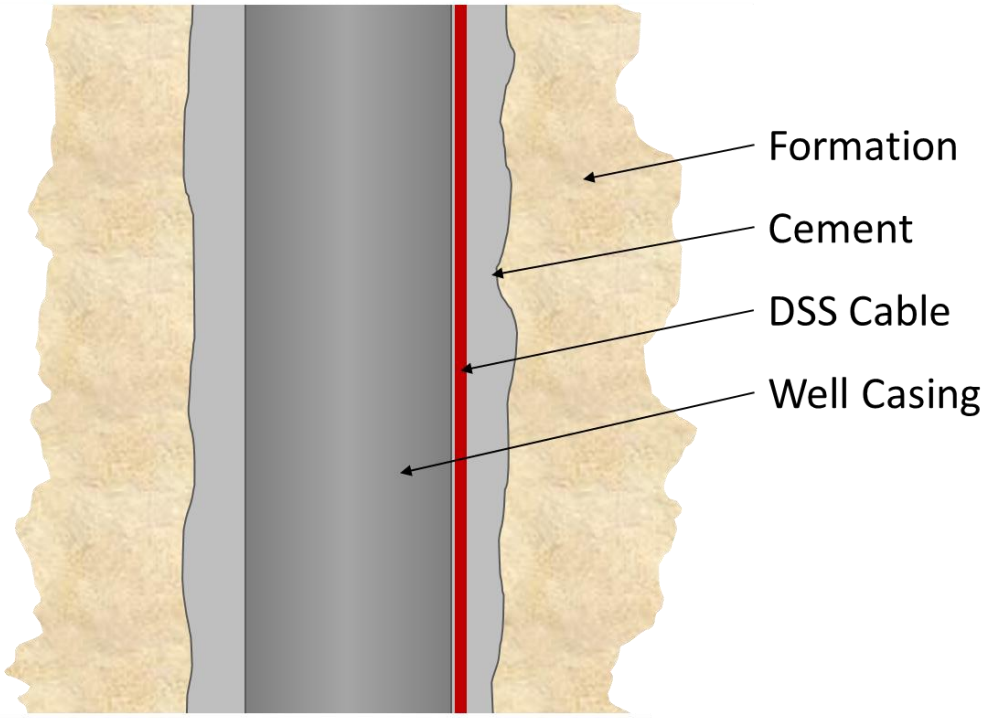

Figure A1.1: Simplified representation of a DSS cable cemented in the annulus behind the casing.

As a starting point, the cement must adequately fill the annular space between the casing and the formation. This can be confirmed by analyzing the cement bond log. The bond index (BI) as derived from the CBL data is shown together with the variable density log (VDL) tracks for the 7" and 3.5" casings in Figure A1.2. The 60% and 80% bond levels are indicated by the red and orange shading, respectively. Behind the 7" casing, the cement is of reasonable quality, being around 50%, and does not show very poorly bonded intervals. The quality behind the 3.5" tubing is of much better quality, especially in the Ten Boer, Slochteren, and Carboniferous formations. In these regions, the bond index typically exceeds 80% without any indication of poor patches.

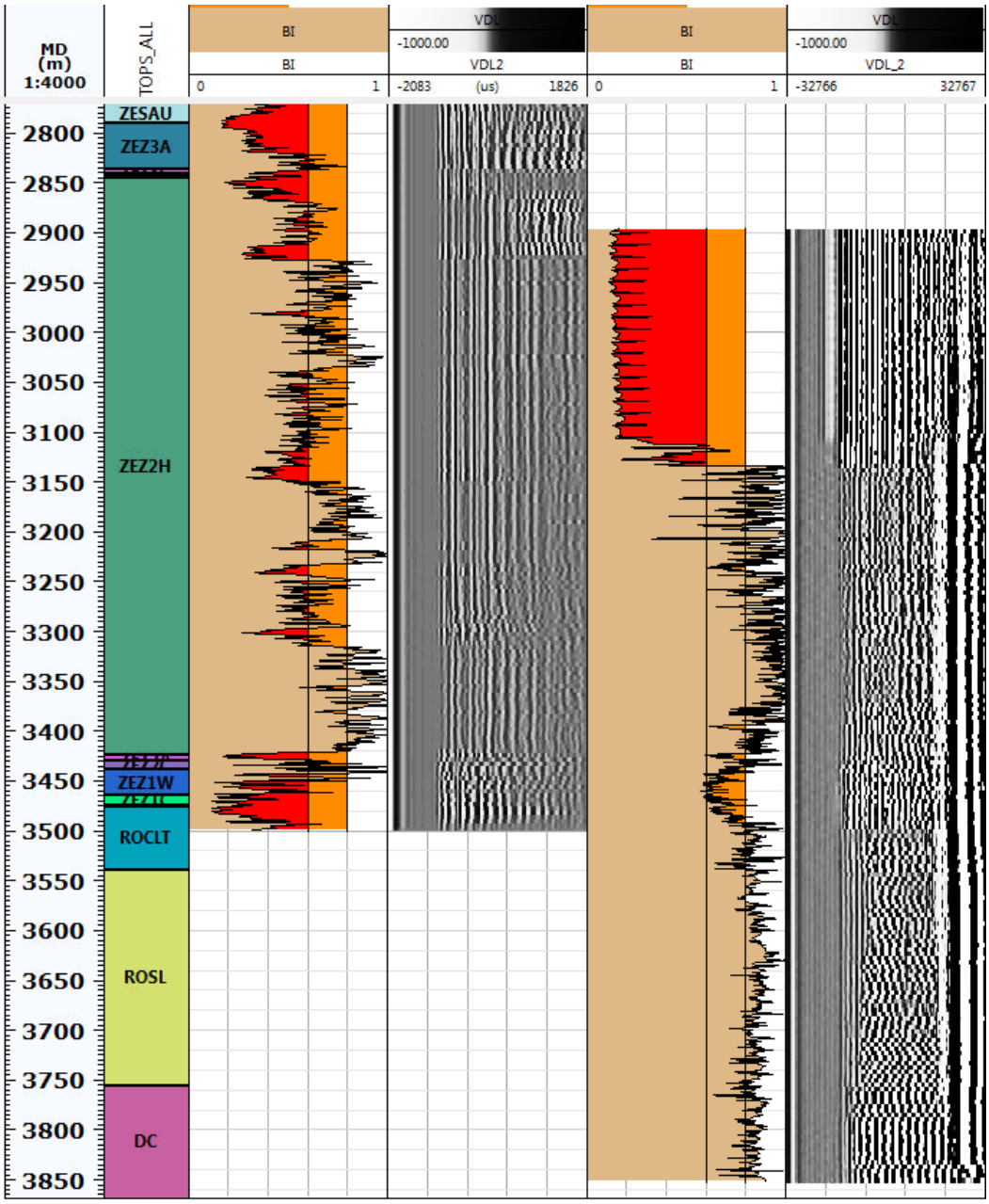

Figure A1.2: Bond index (BI) derived from CBL amplitude attenuation logs, together with VDL tracks. Data shown is from the cement behind the 7" casing and the 3.5" completion.

The good cement bond is in stark contrast to the cement quality in the nearby Zeerijp-2 well, where the BI over the reservoir section regularly dips as low as 10%. The difference can partly be ascribed to the quality of the borehole in Zeerijp-3A. Due to the excessive coring, the borehole of Zeerijp-3A is very straight and in-gauge. In contrast, the Zeerijp-2 reservoir section was drilled with a bicentre bit and shows clear signs of spiraling.

A qualitative interpretation of the cement quality behind the 3.5" casing in the form of a BI is less accurate for depths shallower than ~3500 mAHRT due to the presence of the 7" casing behind it. The interference between the two means a proper bond index cannot, strictly speaking, be determined. However, given the clear transition to a text book free pipe signal around ~3105 mAHRT gives confidence there is a decent amount of cement between the two casings over this interval.

Note that the interval between the ZEZ2H and ROCLT are so-called fast formations, where the sound velocity is higher than that in the steel casing. In such a case, the first arrival seen by the CBL tool is not appropriate for deriving the amplitude damping of the casing, hence the CBL data cannot be used for a proper quantitative interpretation in these intervals. Nevertheless, the fact that the fast formations are observed indicates there is at least some form of acoustic coupling between the casing and formation, in turn suggesting there is at least some cement present.

However, even under perfect cementing conditions the question of the adequacy of bonding still remains. The topic of the bond strength between metal rods and cement has been studied in depth for many years in the context of civil engineering structures utilizing reinforced concrete. A series of pull tests was performed [26] in which the load required to break the bond between a smooth metal rod embedded in a concrete cylinder was measured. This situation is analogous to the DSS cable in the cement column. The results showed that (for the type of concrete used – a 1:2:4 mix of cement, sand, and coarse aggregate) the first measurable slip indicating a weakening of the cohesive bond occurs at ~260 psi.

With a diameter of 0.25", each linear inch of the DSS cable has an exterior surface area of 0.79 in^2. Assuming a shear bond strength of 260 psi, the force required to induce slippage between the cable and the cement is 200 lbs. per inch of bonded cable length. Based on laboratory testing at STCH, it takes ~2500 lbs. of force to yield the DSS cable in compression (a similar value is obtained in tension). Therefore, if more than ~15 inches (38 cm) of cable are embedded in the cement then the cable should yield before it debonds.

Furthermore, it was found during the pull test study [26] that the bond strength increases significantly when the cement is allowed to cure under pressure. With the addition of 100 psi applied to the fresh concrete (for 5 days after molding) the bond strength was increased by 92%. It is not clear what the effect is when the applied pressure is further increased, however, it is probable that the pressure from the overlying fluid column in the well (which is much more than 100 psi) provides a substantial increase to the bond strength.

However, the bond between the cement and the formation might also be complicated by the presence of the filter cake. The filter cake is typically not removed during most cement operations [27] and can act as a potential slip layer between the cement and the formation.

There is no direct evidence in the DSS data to suppose that the cable has debonded at any point along its length and the prevailing assumption is that there is adequate strain coupling to the formation. Ultimately, however, this has not been proven and remains somewhat of an open question.

Appendix 2. Laboratory Compression Tests

The capability to axially compress samples of the DSS cable in the laboratory was developed at Shell Technology Center Houston (STCH) using a custom oven press (see Figure A2.1). A length of the cable is gripped by two clamps on either end of the sample (separated by ~40 cm) and radially confined within a long cylindrical steel fixture to prevent buckling. The sample is then axially compressed by two pistons which can apply loads up to 30,000 psi. The tests can be carried out over a temperature range of 25 – 300°C.

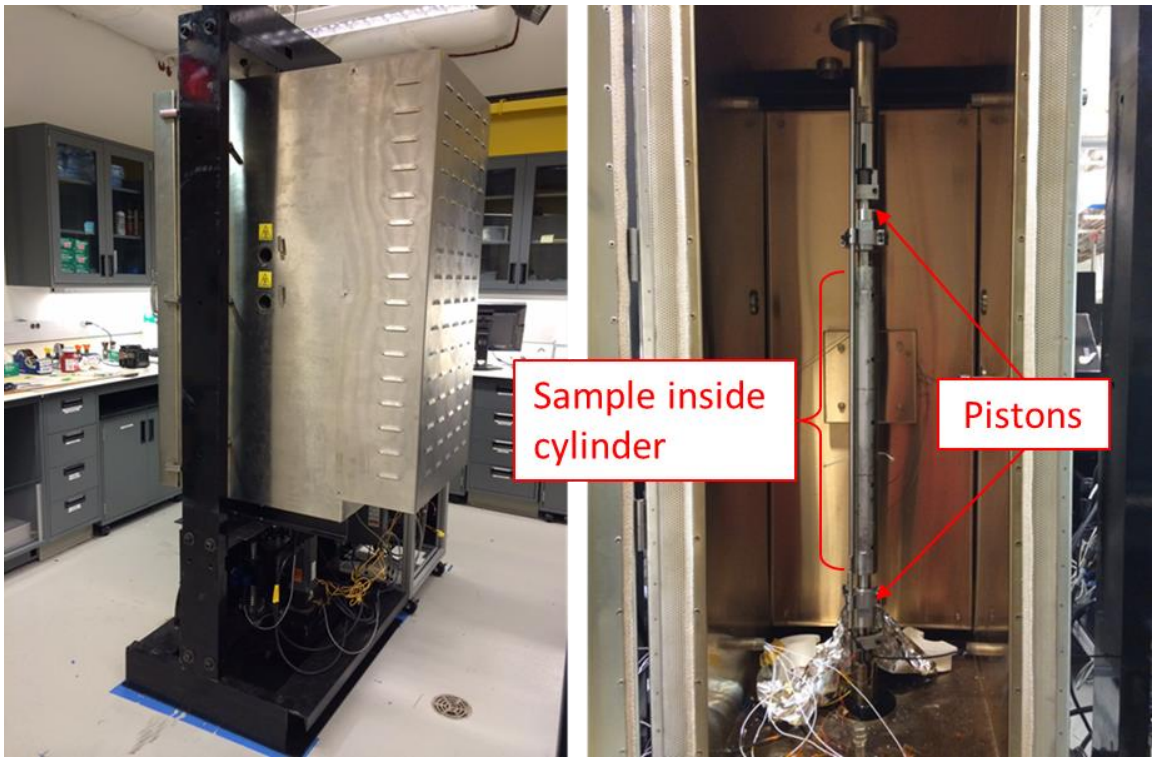

Figure A2.1: Photographs of the compression/tension press at STCH. The picture on the left shows the oven enclosing the press fixtures. The picture on the right shows a compression sample loaded inside the oven.

Figure A2.2 displays the results of a typical compression test on a sample of the SureVIEW WIRE cable. As shown in the upper plot, the mean strain along the region of the sample between the two clamps increases linearly with compression (press displacement). Furthermore, as shown in the bottom plot, at compressive strains below ~0.5% (5,000 με) the response is fairly uniform along the affected length between the clamps (from ~22 – 60 cm along the sample).

At higher mean strains (above ~0.75%), the strain profile develops large gradients due to the Portevin–Le Chatelier (PLC) effect in which the plastic strain deformation becomes localized in the form of bands. This takes place within the grain structure of the metal itself and is a well-known phenomenon that commonly occurs in metals. However, this clearly does not affect the mean strain when averaged over ~20-30 cm. Therefore, even at large strains there is no impact on the aggregate

compaction measurements, though one must exercise caution when interpreting the strain profile. (Note that the onset of the PLC effect occurs at strains approximately 2 orders of magnitude larger than those observed in ZRP-3.)

Though the profile develops non-uniformly at very large strains, there is no evidence of tensile bands forming along the sample at any point during the testing. The strains are entirely compressive in nature.

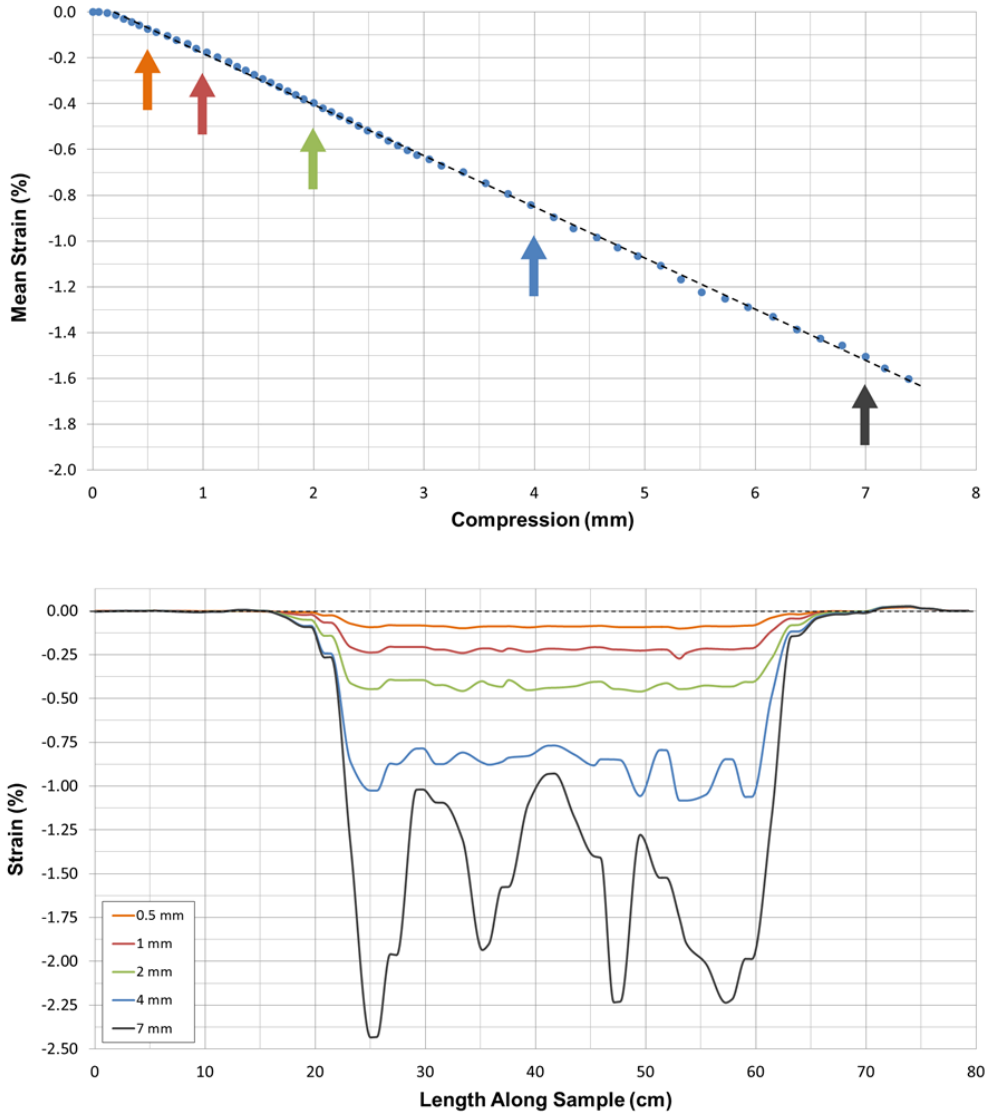

Figure A2.2: **(Top) Mean strain along the fiber as a function of sample compression. The dashed line represents a linear fit to the data. (Bottom) Strain profile along the fiber at the displacements indicated. The arrows in the upper figure indicate the mean strains of the profiles in the lower figure.**

Bibliographic information

Classification	Unrestricted
Report Number	SR.17.00934
Title	The First Year of Distributed Strain Sensing (DSS) Monitoring in the Groningen Gas Field
Author(s)	M. Cannon (SIEP-PTI/RS)
	P. Kole (NAM-PTU/E/Q)
Keywords	DSS, Strain, Compaction, RTCM, RTCI, Fiber, Fibre
Date of Issue	November 2017
US Export Control	US - Non Controlled (EAR99)
WBSE Code	ZZPT/015243/010202
Reviewed by	J. van der Horst (GSNL-PTI/RS)
	D. Doornhof (NAM-PTU/E/Q)
Approved by/Content owner	J. van Elk (NAM-UPO/T/GD)
Sponsoring Company / Customer	Shell International Exploration and Production Inc.
Issuing Company	Shell International Exploration and Production Inc.
	Shell Technology Center Houston
	3333 Highway 6 South
	Houston TX 77082-3101
	USA

Report distribution

Electronic distribution (PDF)

Name, Company, Ref. Ind.	*PDF*
PT Information Services, PTT/TIKE, PT-Information-Services@Shell.com	1
Cannon, Matt Q SIEP-PTI/RS	1
Kole, Pepijn R NAM-PTU/E/Q	1
van Elk, Jan F NAM-UPO/T/GD	1
Doornhof, Dirk NAM-PTU/E/Q	1
Barber, Sarah K NAM-UPO/T/LW	1
Berlang, Wilfred GSNL-PTI/RS	1
Deitrick, Greg L SIEP-PTI/RS	1
Faber, Tjeerd LC NAM-PTT/SDEA	1
Filippidou, Aletta NAM-UPO/T/GD	1
Fournier, Tom SIEP-PTU/E/Q	1
Freeman, Floris C GSNL-PTI/RS	1
Hindriks, Kees OH GSNL-PTI/RC	1
Hol, Sander GSNL-PTI/RF	1
Kuperus, Eddy A NAM-UPO/T/GD	1
Liao, Zijie GSNL-PTI/RS	1
Potters, Hans HHM GSNL-PTI/RS	1
Romijn, Remco NAM-UPO/T/GD	1
Schutjens, Peter MTM GSNL-PTU/E/Q	1
Spivakovska, Daria GSNL-PTI/RS	1
Valvatne, Per H NAM-UPO/T/GD	1
van der Horst, Juun GSNL-PTI/RS	1
van der Wal, Onno NAM-PTU/E/Q	1
van Eijs, Rob MHE NAM-PTU/E/Q	1
Wojtaszek, Magdalena GSNL-PTI/RS	1
Ye, Shuzhen SIEP-PTI/RS	1